Kondo effect under extreme conditions: testing the limits of the Numerical Renormalization Group

Patricia de Assis Almeida

Universidade Federal de Uberlândia
Instituto de Física - INFIS
Programa de Pós-Graduação em Física

Uberlândia
2025

Patricia de Assis Almeida

Kondo effect under extreme conditions: testing the limits of the Numerical Renormalization Group

Dissertation presented to the Graduate Program in Physics at the Federal University of Uberlândia as part of the requirements for obtaining the doctorate degree in Physics.

Área de concentração: Instituto de Física - INFIS

Orientador: Prof. Dr. George Balster Martins
Coorientador: Prof. Dr. Sergio E. Ulloa

Uberlândia
2025

Dados Internacionais de Catalogação na Publicação (CIP)
Sistema de Bibliotecas da UFU, MG, Brasil.

A447k
2025

Almeida, Patricia de Assis, 1992-
Kondo effect under extreme conditions [recurso eletrônico] : testing the limits of the Numerical Renormalization Group / Patricia de Assis Almeida. - 2025.

Orientador: George Balster Martins.
Coorientador: Sergio E. Ulloa.
Tese (Doutorado) - Universidade Federal de Uberlândia, Programa de Pós-graduação em Física.
Modo de acesso: Internet.
Disponível em: http://doi.org/10.14393/ufu.te.2026.5004
Inclui bibliografia.
Inclui ilustrações.

1. Física. I. Martins, George Balster, 1962-, (Orient.). II. Ulloa, Sergio E., 1955-, (Coorient.). III. Universidade Federal de Uberlândia. Programa de Pós-graduação em Física. IV. Título.

CDU: 53

Nelson Marcos Ferreira
Bibliotecário-Documentalista - CRB-6/3074

UNIVERSIDADE FEDERAL DE UBERLÂNDIA
Coordenação do Programa de Pós-Graduação em Física
Av. João Naves de Ávila, 2121, Bloco 1A, Sala 213 - Bairro Santa Mônica, Uberlândia-MG, CEP 38400-902
Telefone: (34) 3239-4309 - www.infis.ufu.br - cpgfisica@ufu.br

ATA DE DEFESA - PÓS-GRADUAÇÃO

Programa de Pós-Graduação em:	Física				
Defesa de:	Defesa de Tese de Doutorado				
Data:	10 de novembro de 2025	Hora de início:	14:00	Hora de encerramento:	16:33
Matrícula do Discente:	12213FIS002				
Nome do Discente:	Patrícia de Assis Almeida				
Título do Trabalho:	Kondo effect under extreme conditions: testing the limits of the Numerical Renormalization Group				
Área de concentração:	Física				
Linha de pesquisa:	Sistemas Fortemente Correlacionados				
Projeto de Pesquisa de vinculação:	*N.A*				

Reuniu-se, por meio de videoconferência, a Banca Examinadora, designada pelo Colegiado do Programa de Pós-graduação em Física, assim composta: Professores Doutores: Gerson Ferreira Junior - INFIS/UFU, Tomé Mauro Schmidt - INFIS/UFU, Ginetom Souza Diniz - UFC, Marcos Sergio Figueira da Silva - UFF e George Balster Martins - INFIS/UFU, orientador da discente.

Iniciando os trabalhos o presidente da mesa, Prof. George Balster Martins, apresentou a Comissão Examinadora e a candidata, agradeceu a presença do público, e concedeu a discente a palavra para a exposição do seu trabalho. A duração da apresentação da discente e o tempo de arguição e resposta foram conforme as normas do Programa.

A seguir o senhor(a) presidente concedeu a palavra, pela ordem sucessivamente, aos(às) examinadores(as), que passaram a arguir o(a) candidato(a). Ultimada a arguição, que se desenvolveu dentro dos termos regimentais, a Banca, em sessão secreta, atribuiu o resultado final, considerando o(a) candidato(a):

Aprovada.

Esta defesa faz parte dos requisitos necessários à obtenção do título de Doutor.

O competente diploma será expedido após cumprimento dos demais requisitos, conforme as normas do Programa, a legislação pertinente e a regulamentação interna da UFU.

Nada mais havendo a tratar foram encerrados os trabalhos. Foi lavrada a presente ata que após lida e achada conforme foi assinada pela Banca Examinadora.

Documento assinado eletronicamente por **Gerson Ferreira Junior**, **Professor(a) do Magistério Superior**, em 10/11/2025, às 17:15, conforme horário oficial de Brasília, com fundamento no art. 6º, § 1º, do Decreto nº 8.539, de 8 de outubro de 2015.

Documento assinado eletronicamente por **George Balster Martins**, **Presidente**, em 10/11/2025, às 18:12, conforme horário oficial de Brasília, com fundamento no art. 6º, § 1º, do Decreto nº 8.539, de 8 de outubro de 2015.

Documento assinado eletronicamente por **Tome Mauro Schmidt**, **Membro de Comissão**, em 11/11/2025, às 13:00, conforme horário oficial de Brasília, com fundamento no art. 6º, § 1º, do Decreto nº 8.539, de 8 de outubro de 2015.

Documento assinado eletronicamente por **Marcos Sergio Figueira da Silva**, **Usuário Externo**, em 11/11/2025, às 14:58, conforme horário oficial de Brasília, com fundamento no art. 6º, § 1º, do Decreto nº 8.539, de 8 de outubro de 2015.

Documento assinado eletronicamente por **Ginetom Souza Diniz**, **Usuário Externo**, em 11/11/2025, às 15:17, conforme horário oficial de Brasília, com fundamento no art. 6º, § 1º, do Decreto nº 8.539, de 8 de outubro de 2015.

A autenticidade deste documento pode ser conferida no site https://www.sei.ufu.br/sei/controlador_externo.php?acao=documento_conferir&id_orgao_acesso_externo=0, informando o código verificador **6843476** e o código CRC **78D6F64E**.

Referência: Processo nº 23117.080298/2025-88 SEI nº 6843476

I dedicate this work to all those who have supported me throughout this journey: family, friends, mentors, and colleagues. Your encouragement, patience, and belief in me have been a constant source of strength. This thesis is a reflection of your support and the inspiration you've provided along the way.

"Nothing in life is to be feared, it is only to be understood. Now is the time to understand more, so that we may fear less."

(Marie Curie)

Resumo

O estudo de fenômenos físicos em condições extremas (baixíssimas temperaturas, por exemplo) tem historicamente mostrado potencial para revelar estados inesperados da matéria condensada, ao mesmo tempo que representa um grande desafio às técnicas de pesquisa, tanto experimentais quanto teóricas. Um exemplo seria a descoberta da supercondutividade quando se conseguiu liquefazer o hélio e fazer medidas de resistividade a baixíssimas temperaturas. Portanto, seguindo esta linha de raciocínio, nesta Tese estudamos o efeito Kondo em duas situações extremas: (i) sistemas onde a densidade de estados do metal hospedeiro apresenta divergências fortes próximas à energia de Fermi; (ii) sistemas de dois pontos quânticos (PQs) em geometria T, onde as escalas de energia de interesse se estendem por um intervalo de aproximadamente 20 ordens de magnitude. Tais sistemas foram estudados via a ferramenta computacional Grupo de Renormalização Numérica (NRG, na sigla em inglês). Em (i), vimos que divergências relativamente suaves, do tipo $\omega^{-1/2}$, geram uma série de estados de muitos-corpos com propriedades inusitadas. Divergências mais fortes têm, portanto, potencial de revelar mais surpresas. Já no sistema de dois PQs, apresentamos resultados que nos permitem orientar os experimentais a como calibrar as propriedades dos PQs, de maneira a distinguir claramente dois regimes com propriedades bastante distintas, sendo, regime de Kondo de dois estágios e regime molecular. Para analisar o efeito Kondo em condições que podemos chamar de extremas (quais sejam, divergências fortes na densidade de estado do hospedeiro e variações extremas na escala de energia) foi necessário levar o NRG a situações limítrofes, levando os parâmetros do método a valores extremos.

Palavras-chave: Kondo. NRG. Ponto quântico.

Patricia de Assis Almeida

Universidade Federal de Uberlândia
Instituto de Física - INFIS
Programa de Pós-Graduação em Física

Uberlândia
2025

Abstract

The study of physical phenomena under extreme conditions (very low temperatures, for example) has historically shown the potential to uncover unexpected states in Condensed matter Physics, at the same time, it poses a stiff challenge to both experimental and theoretical research techniques. One celebrated example was the discovery of superconductivity when it became possible to liquefy helium and thus perform resistivity measurements at temperatures of a few Kelvin. Following this approach, in this Thesis we study the Kondo effect under two extreme conditions: (i) systems where the metallic host density of states presents a strong divergency near the Fermi energy; (ii) T-shape double quantum dot (DQD) systems, where the energy scale of interest spans 20 orders of magnitude. Both systems were studied using the Numerical Renormalization Group (NRG) method. In (i), we obtained that relatively soft divergencies, of the $\omega^{-1/2}$-type, generate a series of many-body bound-states with peculiar properties. We thus believe that stronger divergencies (associated to flat bands, for example) have the potential to uncover additional surprises. As to the DQD system, we obtained results that allow us to guide the experimentalists on how to tune the DQD characteristics in order to clearly distinguish two regimes with very different properties, viz., the two-stage Kondo regime and the molecular regime. To analyze the Kondo effect in these so-called extreme conditions (strong host DOS divergencies and extreme energy scale variation) it was necessary to force the NRG into high-demand scenarios, pushing its parameters to extreme values.

Keywords: Kondo Effect. NRG. Quantum dots.

List of Figures

Acronyms list

NRG Numerical Renormalization Group

PHS Particle-hole Symmetry

QD Quantum Dot

QDs Quantum Dots

FL Fermi Liquid

RG Renormalization Group

SIAM Single Impurity Anderson Model

SOI Spin-Orbit Coupling

T_K Kondo Temperature

TRS Time-Reversal Symmetry

RL Resonant Level

HF Heavy Fermion

HFs Heavy Fermions

QCP Quantum Critical Point

SCES Strongly Correlated Electron Systems

AIM Anderson Impurity Model

SW Schrieffer–Wolff

LM local moment

E_F Fermi energy

CBP Coulomb blockade peak

TSK two-stage Kondo

Contents

Chapter 1

Introduction

In condensed matter physics, we are interested in investigating the physics of diverse systems (12). An area of great interest, due to its relevance in understanding real systems, is the study of Strongly Correlated Electron Systems (SCES). Usually, SCES are characterized by electron motion being restricted by the positions and motions of all other electrons, a consequence of Coulomb repulsion. By definition, all materials may exhibit some degree of correlation, in ionic systems or in ideal metals, the essential properties can be described by simplified models that neglect such correlations or treat them with approximations, as in the case of the free-electron Fermi gas or the Fermi Liquid (FL). But in SCES these approximations are insufficient because it is hard to solve the many-body problem involving a large number of particles.(13, 14, 15).

The complexity in SCES arises from the competition among multiple degrees of freedom which collectively determine the ground state (16). Remarkably, one of the most significant manifestations of SCES are Heavy Fermion (HF) metals (17), in which electronic excitations exhibit effective masses up to a thousand times greater than those of conventional metals. In these systems, the Kondo effect, associated with the screening of localized magnetic moments by conduction electrons, plays a key role. Heavy Fermions (HFs) frequently display non-Fermi Liquid (NFL) behavior,evidenced by the breakdown of Landau's description. Such behavior typically emerges close to a Quantum Critical Point (QCP) (18), corresponding to a continuous zero-temperature phase transition.

Since its discovery in the 1930s (19), the Kondo effect has become a key concept since then, significantly advancing the comprehension of SCES. Its initial detection dates back to 1934, with Haas et al. reporting an unusual reduction in the electrical resistance of some metals at low temperatures. However, contrary to the expected steady decrease predicted by Matthiessen's rule (20), the resistivity exhibited a minimum, a characteristic subsequently found in various dilute metallic alloys containing some amounts of magnetic impurities. The physics behind this minimum remained elusive until 1964, when Jun Kondo formulated a theory based on the exchange interaction between localized magnetic

moments and conduction electrons (21). By employing the s-d exchange Hamiltonian, now recognized as the Kondo model, and utilizing perturbation theory, he demonstrated that many-body scattering processes result in a logarithmic contribution to resistivity at low temperatures. This analysis introduced the T_K, an energy scale defining the resistivity minimum and the transition from weak to strong coupling. Although its exponential expression is reminiscent of BCS theory, the T_K represents a crossover rather than a true phase transition. However, Kondo's perturbative approach predicted a divergent increase in resistance as $T \to 0$, a theoretical limitation. Kenneth Wilson solved this in 1974 by developing the NRG (22), establishing a nonperturbative approach able to describe the full temperature range of Kondo physics.

The physics of this effect can be analyzed using two standard models. The first, the Anderson Impurity Model (AIM), elucidates the hybridization between localized orbitals and conduction band states. The second, the Kondo Hamiltonian, derived via the Schrieffer–Wolff (SW) transformation, effectively projects the Anderson model into the subspace of localized magnetic moments. This projection yields an antiferromagnetic exchange Hamiltonian that governs the interaction between the impurity spin and the local spin density of conduction electrons.

Below T_K, it is possible to observe the emergence of a strongly correlated state. This occurs because, at this energy scale, the localized magnetic moment is effectively shielded by the surrounding conduction electrons. The interaction between the localized moment and the conduction electrons, characterized by repeated spin-inversion scattering events, leads to the formation of a collective ground state. Consequently, the system no longer exhibits the properties of a free magnetic ion but rather behaves as a nonmagnetic scattering center. For a complete understanding of this phenomenon, it was necessary to develop non-perturbative methods, since perturbation theory fails to describe systems with strong Coulomb interaction. These included Anderson's scaling theory, Wilson's NRG, and Nozières's framework (23), which defined the low-energy behavior as a renormalized FL.

Progress in nanotechnology has enabled the artificial realization of the Kondo effect in Quantum Dots (QDs), marked by substantial progress in the 1990s (24). These QDs, often regarded as artificial atoms, allow for precise control over parameters that govern the Kondo phenomenon, such as the number of confined electrons, the local level energy, and the coupling (hybridization) with conduction electrons in the leads. Unlike traditional dilute metals, where the Kondo effect manifests as increased resistivity, in quantum dots it appears as an enhancement of electrical conductance, which at very low temperatures can reach the unitary quantum limit of $G = 2e^2/h$. A distinctive signature of this effect is the zero-bias anomaly, observed as a sharp resonance peak in electrical conductance in the density of states at the Fermi level. The tunability of these parameters, including the bias, allows researchers to directly adjust T_K, making quantum dots an ideal platform for exploring the fundamental properties of the Kondo effect under controlled conditions.

Extensions of this phenomenon beyond a single impurity involve multichannel and SU versions (25, 26), notably the Kondo lattice model. In this model, a dense lattice of magnetic moments interacts with conduction electrons, leading to heavy fermion metals. These metals exhibit very high effective masses and a balance between the local Kondo effect and long-range magnetic interactions (27).

Recently, growing attention has been directed to the SCES. However, from the rigorous point of view, many phenomena still require further elucidation. Despite extensive study, the Kondo effect remains a valuable probe of correlated systems. The Kondo effect can be observed through a variety of experimental techniques, including scanning tunneling microscopy and transport measurements (28, 29). Superconductivity in materials is significantly influenced by the Kondo effect. For example, in $Pb_{1-x}Tl_xTe$, superconductivity was found due to a charge Kondo effect (30). Furthermore, in Nb thin films, residual superconductivity was observed even in the presence of the Kondo effect (31). Another field that has seen extensive research is the study of the Kondo effect in topological insulating systems. Notably, topological insulator quantum dots have been found to exhibit a spin-orbital Kondo effect (32). In addition, emerging research investigates the Kondo effect in kagome lattices, well-known for its flat energy bands. The presence of these flat bands alters the dependencies of the Kondo temperature and coherence temperature, substituting exponential relationships with linear and quadratic ones, respectively (33). In flat-band systems, the Kondo effect can be simplified to a two-electron molecular Kondo problem, resulting in distinct thermodynamic and dynamic characteristics (34).

This thesis is organized as follows:

Chapter 2 - Kondo Effect. This chapter presents an analysis of the Kondo phenomenon, analyzing its physical effects and theoretical implications, as well as its practical uses. Furthermore, the Kondo and Anderson models are introduced, providing the conceptual basis for studying the Kondo problem.

Chapter 3 - The Numerical Renormalization Group Approach. In this chapter, we describe the Numerical Renormalization Group (NRG) method and explain how this approach can be used to solve the Kondo problem. The chapter details the fundamentals of the technique and its relevance in investigating systems with strong electron correlations.

Chapter 4 - Resonant Level. In this chapter, we investigate the behavior of a non-interacting Resonant Level (RL) when positioned near (or exactly on) the singularity $\omega^{-1/2}$, which naturally arises in a one-dimensional quantum wire. We highlight its most relevant characteristics and, using the Anderson model, analyze the effects caused by the presence of an impurity interacting with a host system whose energy band presents a divergence in the density of states.

Chapter 5 - 1D quantum wires with impurities: NRG approach . This chapter investigates the Kondo state within a metallic system exhibiting a $\omega^{-1/2}$ singularity

in its density of states, characteristic of one-dimensional chains. By employing the Single Impurity Anderson Model and utilizing Numerical Renormalization Group analysis, we demonstrate the profound influence of Hubbard interaction on the bound state and its corresponding spectral features. As the impurity level ε_d approaches this singularity, Kondo characteristics re-emerge, and the local moment fixed point demonstrates resilience against charge fluctuations. Furthermore, we propose an experimental setup employing armchair graphene nanoribbons to realize these phenomena.

Chapter 6 - Modeling the Two-Stage Kondo Regime via NRG . In this chapter, we investigate the behavior of a compound impurity in a metal, which can explore different configurations where its net magnetic moment can be screened by the host electrons. Here, we investigate a two-stage Kondo (TSK) system, in which the screening process occurs successively at distinct and progressively lower energy scales. In contrast, impurities may prefer a local singlet disconnected from the metal. This competition is decided by the tuning of the couplings in the system. A T-shaped double quantum dot geometry, where a 'dangling' dot is connected to the current-carrying conductors only through another dot, represents a flexible system in which these different regimes can be explored experimentally.

Chapter 2

Kondo Effect

Quantum impurity models are employed to describe scenarios where an atom or molecule is integrated into a host material (35). These models were initially developed to examine the behavior of transition metal ions, which, despite typically exhibiting magnetic characteristics, are situated within non-magnetic metals. Such systems can be conceptualized as the interaction between two subsystems: a localized system, akin to a magnetic impurity with limited degrees of freedom, and an infinite-dimensional system characterized by a continuous spectrum (36, 11). The Kondo effect, a many-body phenomenon associated with magnetic impurities, is intrinsically tied to the concept of electron localization, a fundamental aspect in the study of strongly correlated materials, particularly those containing atoms with partially filled d or f orbitals (16). Within these materials, the competition between localized magnetic moments and a collective of delocalized electrons leads to rich physics.

To understand the physics involved in the Kondo effect, it is important first to consider how the concept of electronic localization appears within the periodic table. The Kmetko-Smith diagram, Fig. 1(a), provides a clear representation of this organization, showing that as one moves towards the top right of the diagram, electrons become progressively more localized (37, 38). Metals located in the lower left region exhibit itinerant d orbitals, which favor the occurrence of superconductivity at low temperatures. However, metals located in the upper right region of the periodic table exhibit strongly localized f electrons, which commonly lead to the formation of magnetic structures, such as antiferromagnetic orderings.

Thus, it may suggest that the physics of the Kondo effect is closely related to the presence of localized magnetic moments, which consist of spins confined to specific sites within the crystal lattice. One of the classical manifestations of these moments is the magnetic susceptibility that follows the Curie-Weiss law at high temperatures, expressed by

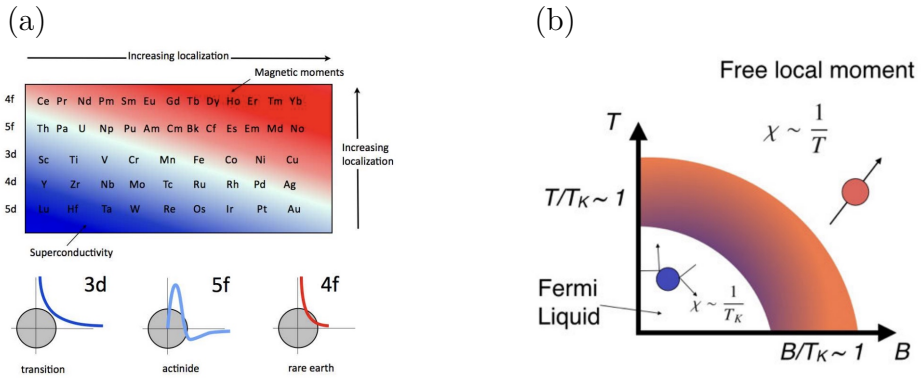

Figure 1 – (a) The Kmetko-Smith diagram shows growing electron localization in d and f compounds. (b) Simplified temperature-field phase diagram of the Kondo effect. For $T, B \gg T_K$, the local moment remains unscreened with Curie-like susceptibility. For $T, B \ll T_K$, it becomes screened, acting as an elastic scatterer in a Landau Fermi liquid with Pauli susceptibility $\chi \sim 1/T_K$. From Ref. (1).

$$\chi \approx \frac{n_1 M^2}{3(T+\theta)}, \tag{1}$$

In Eq. 1, χ represents the magnetic susceptibility, n_1 is the number of magnetic moments per unit volume, M is the magnetic moment associated with each localized center, T is the absolute temperature, and θ is the Weiss constant, which reflects the interactions between the magnetic moments. This behavior may highlight the localized nature of the moments and provides a way to analyze magnetic interactions in systems with impurities.

Having established the concept of local moment, we can now explore the Kondo Effect conceptually. This effect describes the process by which a magnetic impurity, which exhibits Curie-type magnetic susceptibility at high temperatures, becomes "screened" by the spins of conduction electrons, forming, at low temperatures and magnetic fields, a spinless scattering center, effectively destroying the MB singlet state. This screening process occurs continuously and begins when the temperature or magnetic field drops below a characteristic energy scale known as the T_K, which will be explained in detail later. These "quenched" magnetic moments act as strong elastic scattering potentials for the electrons, leading to an increase in electrical resistivity due to the presence of magnetic impurities, this resistivity minimum is the hallmark of the Kondo effect. Figure 1(b) illustrates the phase diagram of the Kondo effect with respect to temperature. Within this diagram, B denotes the magnetic field, and T represents the temperature. At temperatures and magnetic fields significantly higher than T_K, the local moment remains free, displaying a Curie-type susceptibility. Conversely, at low temperatures and magnetic fields relative to T_K, the local moment is fully compensated. This state manifests as an elastic scattering

center within a Landau Fermi liquid, characterized by a Pauli susceptibility on the order of $1/T_K$.

2.1 Historical and Fundamental Aspects

The Kondo Effect is a physical phenomenon whose roots date back to early studies of dilute magnetic metal alloys, characterized by the presence of low concentrations of impurity atoms embedded in a host metal. These alloys, called dilute, are obtained through the controlled introduction of distinct elements into the base metal, a process that induces specific changes in properties such as electrical resistivity and the magnetic behavior of the system (39). It was first observed experimentally over nine decades ago. In pioneering experiments, De Haas, De Boer, and Van den Berg (1934) measured the resistance of impure gold wires and discovered an unexpected resistivity minimum at low temperatures (19).

In metals such as gold, it was initially assumed that electrical resistance should decrease with lowering temperature, as the interaction with phonons becomes progressively weaker. It was assumed that, at extremely low temperatures, the resistance would stabilize at a constant value, determined primarily by impurities in the material. However, as shown in Fig. 2(a), based on data from the study conducted on (2): unexpected behavior was observed. The resistance of gold and later of other metals reached a minimum and, instead of remaining constant, increased again as the temperature continued to drop. The behavior described earlier lacked a complete theoretical explanation until the 1960s, when that was achieved. Another fundamental aspect of the Kondo effect concerns its universality, that is, when the impurity properties are rescaling as a function of the Kondo temperature, all corresponding curves collapse into a single universal form. This is shown in Fig. 2(b).

Below, we present the mathematical formulation used to describe a system undergoing the Kondo effect.

2.1.1 Exchange s-d Model

The s-d exchange model, proposed by Zener in 1951 (40), describes the effects of a magnetic moment on conduction electrons (this phenomenon is exemplified in metallic systems containing magnetic impurities). When considering a single magnetic impurity embedded into the metal, the interaction between the conduction electrons and the impurity's magnetic moment can be described by a Hamiltonian given by

$$H_{sd} = \sum_{k,k'} J_{k,k'} \left(S^+ c^\dagger_{k,\downarrow} c_{k',\uparrow} + S^- c^\dagger_{k,\uparrow} c_{k',\downarrow} + S_z \left(c^\dagger_{k,\uparrow} c_{k',\uparrow} - c^\dagger_{k,\downarrow} c_{k',\downarrow} \right) \right), \tag{2}$$

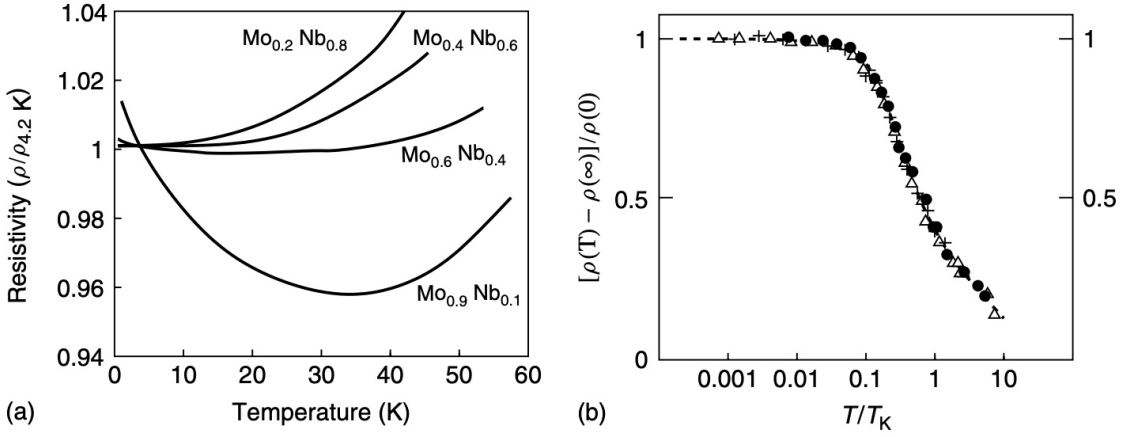

Figure 2 – (a) Evidence for a resistivity minimum in the alloy system MoxNb$_{1x}$, from Ref. (2). (b) Variation of resistivity with temperature, due to scattering by magnetic ions, exhibiting a universal behavior determined by the Kondo temperature. From Ref (3).

Eq. 2 describes a Heisenberg-like interaction between the conduction electrons and a localized moment, governed by an exchange coupling denoted by $J_{k,k'}$. The spin operators associated with the impurity, S_z and $S^{\pm}$ (defined as $S_x \pm iS_y$), characterize a single impurity with spin S. This interaction can induce spin flips in the conduction electrons as a result of scattering caused by the impurity. In addition to the term shown in Eq. 2, a full description of the Kondo effect must also include a term for the host metal, which represents the conduction electrons,

$$H_{cond} = \sum_{k,\sigma} \epsilon_k c^{\dagger}_{k,\sigma} c_{k,\sigma}. \tag{3}$$

Here, H_{cond} denotes the Hamiltonian of the conduction electrons. The parameter ϵ_k corresponds to the energy of an electron with momentum k, while the operators $c^{\dagger}_{k,\sigma}$ and $c_{k,\sigma}$ represent the creation and annihilation operators, respectively, for electrons with momentum k and spin σ.

$$H = H_{sd} + H_{cond}. \tag{4}$$

By setting the coupling constant $J_{k,k'}$ to zero, the system begins to behave like an isolated ion, which leads to the manifestation of a free magnetic moment. Under these conditions, the susceptibility follows Curie's law.

2.1.2 Solution proposed by Jun Kondo

One explanation for the emergence of the resistance minimum in metals has been proposed based on experimental evidence, which revealed a correlation between two key factors: first, the observation of Curie-Weiss behavior in the magnetic susceptibility of impurities, indicating the presence of localized magnetic moments, and second the appearance of a minimum in the electrical resistance curve. This correlation motivated Jun Kondo, a Japanese physicist, to pursue a theoretical investigation of the phenomenon in 1964. Kondo showed that the minimum in electrical resistance arises from the interaction between the spin states of localized and conduction electrons. To describe this, he employed the s-d model and applied perturbation theory up to third order in the exchange coupling $J_{kk'}$. According to linear response theory, determining the resistivity requires calculating the T-matrix associated with the problem, which can be achieved through the computation of the transport lifetime $\tau_1(\epsilon, k)$, defined by the following expression (41)

$$\frac{1}{\tau_1(k)} = 2\pi c_{\text{imp}} \int \delta(\epsilon_k - \epsilon_{k'}) \left|T_{kk'}\right|^2 (1 - \cos\theta') \frac{dk'}{(2\pi)^3}, \tag{5}$$

where c_{imp} is the impurity concentration and θ' is related to the scattering angle. The matrix elements of the scattering operator $T(\epsilon^+)$, evaluated between Slater states in which a conduction electron is scattered from $|k, \sigma\rangle$ to $|k', \sigma'\rangle$, take the following forms at the lowest order in $J_{kk'}$

$$\begin{aligned}
\langle k', \uparrow | T(\epsilon^+) | k, \uparrow \rangle_{(1)} &= J_{kk'} S_z, \\
\langle k', \uparrow | T(\epsilon^+) | k, \downarrow \rangle_{(1)} &= J_{kk'} S^-, \\
\langle k', \downarrow | T(\epsilon^+) | k, \uparrow \rangle_{(1)} &= -J_{kk'} S_z, \\
\langle k', \downarrow | T(\epsilon^+) | k, \downarrow \rangle_{(1)} &= J_{kk'} S^+.
\end{aligned} \tag{6}$$

Assuming an exchange coupling independent of k, given by $J_{kk'} = \frac{J}{N_s}$, where N_s is the number of sites, and considering parabolic dispersion for free electrons, $\epsilon(k) = \frac{\hbar^2 k^2}{2m}$, with bandwidth D such that $\epsilon_k, \epsilon_{k'} < D$, the expression for the transport lifetime at the Fermi level, up to second order in J, is:

$$\tau(k_F) = \frac{2e^2 \epsilon_F}{3 n c_{imp} J^2 S(S+1)}. \tag{7}$$

From the previous result, the impurity resistivity due to impurities can be written as

$$R_{\text{imp}} = \frac{3\pi m J^2 S(S+1)}{2e^2\hbar\epsilon_F}, \tag{8}$$

where m is the electron mass, J the exchange coupling constant, S the impurity spin, e the elementary charge, $\hbar$ the reduced Planck constant, and ϵ_F the Fermi energy. This term is temperature-independent and therefore cannot explain the observed increase in resistivity at low temperatures.

To capture the increase in resistivity at low temperatures, the calculations must be extended to third order in J. This requires first determining the second-order terms in the T-matrix, as they contribute to the third-order corrections. Kondo carried out these calculations and obtained an expression in which the resistivity depends explicitly on temperature, taking the following form:

$$R_{\text{spin}}^{\text{imp}} = \frac{3\pi m J^2 S(S+1)}{2e^2\hbar\epsilon_F}\left(1 - 4J\rho_0(\epsilon_F)\ln\left(\frac{k_B T}{D}\right)\right). \tag{9}$$

By taking all terms into account, the total resistivity of a metal can be expressed as

$$R(T) = aT^5 + c_{\text{imp}}R_0 - c_{\text{imp}}R_1\ln\left(\frac{k_B T}{D}\right), \tag{10}$$

where aT^5 term represents electron-phonon scattering, The $c_{imp}R_0$ is the temperature-independent potential scattering from impurities and the last term is related to the presence of magnetic impurities in the material and is only relevant at low temperatures.

Kondo's foundational research elucidated the experimental observation, establishing that its core mechanism stems from the interplay between localized magnetic moments and conduction electrons. He clarified that the unusual temperature-dependent electrical resistivity, characterized by a minimum at low temperatures, is not attributable to intrinsic properties of the impurity, such as its charge. This interaction results in a distinctive resistivity profile as a function of temperature, where the minimum arises from the cumulative effect of individual magnetic moments, rather than from correlations between localized spins. Kondo's theoretical predictions show excellent agreement with the experimental data:

- ❏ The minimum temperature T_{min} is approximately proportional to $c_{imp}^{1/5}$ and is given by

$$T_{\text{min}} = \left(\frac{R_1}{5a}\right)^{1/5} c_{\text{imp}}^{1/5}. \tag{11}$$

- ❏ The depth of the minimum is approximately proportional to the concentration c_{imp}.
- ❏ The dependence on $\log T$ has been confirmed experimentally, especially in gold-iron alloys.

Kondo's work marked a advance in the understanding of a phenomenon studied for over three decades. His theory explained the abrupt increase in resistivity in metals with impurities, introducing the concept of the T_K, but it had limitations: it predicted a divergence in resistivity below T_K that was not confirmed experimentally. Despite this limitation, his model significantly advanced research on the Kondo effect, and a full explanation of the phenomenon was only achieved in the 1970s with the development of the numerical renormalization method, a topic that will be discussed in greater detail in the next chapter.

2.1.2.1 Kondo Temperature

The T_K is usually taken as a central energy scale, though perhaps more a crossover indicator than a strict boundary, marking when a magnetic impurity begins to couple strongly with the conduction electrons. This characteristic temperature depends exponentially on the exchange coupling J and the density of states ρ at the Fermi level, and can be expressed by the following equation:

$$T_K \sim De^{-1/(J\rho)}, \tag{12}$$

An important quantity is the impurity spectral function, $A_d(\omega)$, which characterizes the density of electronic states localized at the impurity as a function of the energy ω. Within the Kondo regime, this function is characterized by a sharp peak situated at the Fermi level, commonly referred to as the Kondo resonance. The bandwidth of this resonance is directly correlated with the Kondo temperature, T_K. Consequently, experimental techniques like scanning tunneling spectroscopy can be employed to probe the spectral function, enabling the direct determination of T_K from the measured width of the Kondo resonance. In the absence of interactions $U = 0$, the spectral function is a simple Lorentzian resonance centered at ε_d, with a width determined by the hybridization Γ. The three-peak structure emerge when strong Coulomb interaction U is present. Fig. 3 shows the spectral function $A(\omega)$ for an impurity in an interacting system. It highlights three main regions, specifically in the case where the system exhibits particle–hole symmetry.

The lower Hubbard band, located at $-U/2$ corresponds to occupied states and represents the energy required to remove an electron from the impurity orbital, driving the transition from single occupation to zero occupation. The Kondo resonance, or Kondo

peak, is directly related to the screening of the impurity spin caused by conduction electrons, as a result of low-energy excitation processes. This peak does not persist at temperatures above the Kondo temperature, highlighting its direct connection to the effect. Furthermore, in the presence of a magnetic field, the peak splits into two (42). Similarly, the upper Hubbard band, located at $U/2$ on the positive side of the spectrum, corresponds to unoccupied states. It represents the energy required to add a second electron to the impurity orbital, driving the transition from single to double occupancy, which involves overcoming the Coulomb repulsion U.

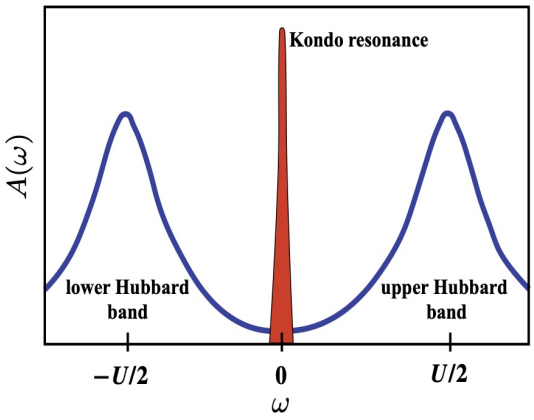

Figure 3 – Spectral function characteristic of the Kondo regime, highlighting the Hubbard peaks located at high energies and the Kondo resonance centered at the Fermi level. From Ref. (4).

2.1.2.2 Kondo cloud

There is a spatial scale known as the Kondo length, denoted by ξ_K, which characterizes the extent of the so-called Kondo cloud (6, 43). This cloud is a spatial manifestation of the quantum correlations between a localized magnetic moment and the conduction electrons in a metal and arises due to the Kondo effect. Within this region, the electrons interact strongly with the impurity's spin, forming a singlet (non-magnetic) state. Outside the Kondo cloud, the electrons do not couple directly to the impurity's magnetic moment at low energies. They feel its influence only through an effective potential that becomes a scattering center (responsible for the increased resistivity of the metal at low temperatures). This type of interaction induces a characteristic phase shift of $\pi/2$ in the Fermi energy.

Figure 4, right panel, illustrates the situation for $T > T_K$, where the electrons interact only weakly with the impurity, leaving the impurity spin essentially free. In contrast, the left panel shows that for $T < T_K$, the impurity strongly interacts with the collective state of the metal's conduction electrons, giving rise to the Kondo cloud that surrounds and screens it. Mathematically, the extent of the Kondo cloud is expressed by

$$\xi_K = \frac{\hbar v_F}{T_K}, \tag{13}$$

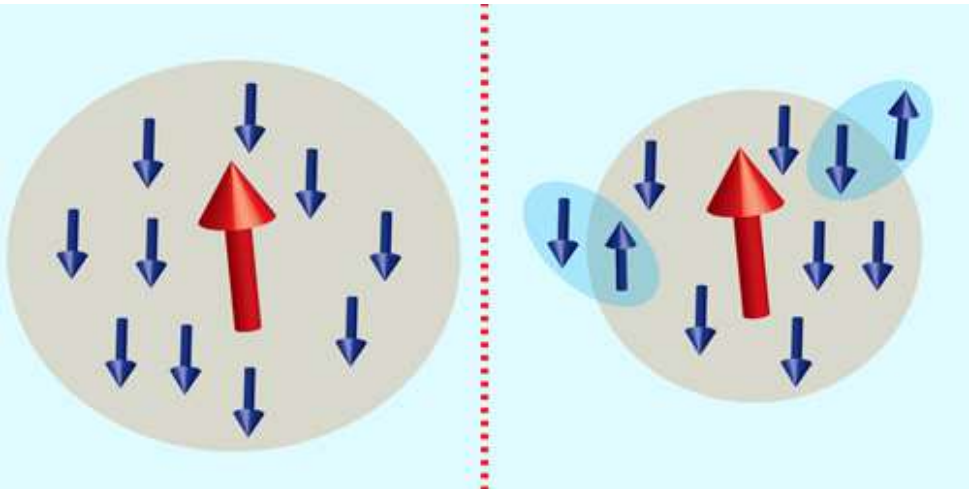

Figure 4 – Left panel: when $T < T_K$, the impurity strongly affects the conduction electrons, which begin to gather around it, forming a singlet state. Right panel: for $T > T_K$, the impurity (red arrow pointing upward) interacts weakly with the conduction electrons (blue arrows pointing downward), having minimal influence. From Ref. (5).

where v_F represents the Fermi velocity. In quantum dot experiments, the characteristic temperature of the Kondo effect is typically below 1K and can be tuned by the gate voltage V_g. Considering a Fermi velocity of the order of $v_F = 5 \times 10^5, \mathrm{m/s}$, the spatial extent associated with the phenomenon reaches approximately 3 μm (44, 45).

Due to this macroscopic spatial scale and the nonlocal nature of the correlations, direct observation of the Kondo cloud remains challenging. In (6), researchers performed Kondo cloud measurements in a setup consisting of a quantum dot containing an unpaired spin, which simulates a magnetic impurity, coupled to a one-dimensional (1D) ballistic channel of extended length. This channel had multiple conduction modes to allow electron flow and included three quantum point contact (QPC) gates, positioned at distances of $L = 1.4 \quad \mu m$, $L = 3.6 \quad \mu m$, and $L = 6.1 \quad \mu m$, respectively, from the quantum dot (QD). The device is operated by forming a Fabry-Pérot (FP) interferometer. The length of each cavity corresponded to the distance between the QD and the respective QPC used. By varying the voltage applied to the QPC gate, the cavity could be adjusted to or from resonance, thus modifying the electron density within it. This variation disturbed the electron density and generated oscillations in the Kondo temperature measured in the QD. Analysis of the amplitude of these oscillations at different distances allowed us to experimentally determine the spatial extent of the Kondo cloud.

Figure 5 presents an analysis of the relationship between the Fabry-Pérot cavity (FP) length and the T_K, aiming to highlight the spatial extent of the Kondo cloud. In the

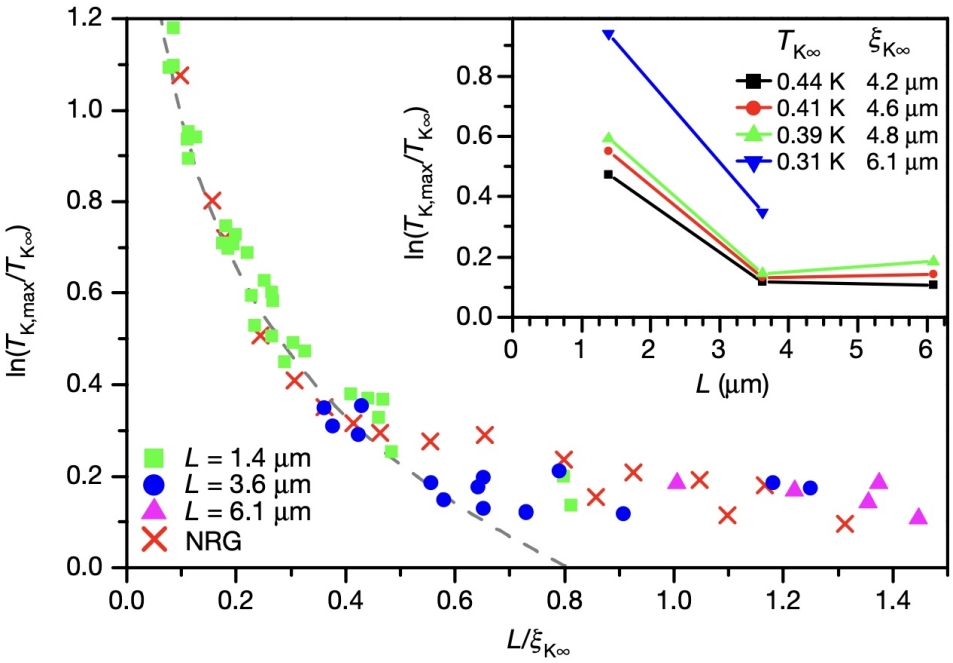

Figure 5 – Amplitude of the Kondo temperature oscillations, T_K, plotted as a function of the Fabry-Pérot cavity length L and normalized by the characteristic Kondo cloud length, ξ_K. Experimental data for cavities of 1.4 μm, 3.6 μm, and 6.1μm collapse onto a universal curve, demonstrating that ξ_K determines the spatial extent of the Kondo cloud. The dashed line shows the theoretical relation, $\ln(T_{K,\max}/T_{K0}) = -n\ln(L/\xi_K)$ with $n = 0.47$, obtained via numerical renormalization group (NRG) calculations. From Ref. (6).

graph, the vertical axis corresponds to

$$\ln\left(\frac{T_{K,\max}}{T_{K0}}\right), \tag{14}$$

that is, the logarithm of the ratio of the maximum measured T_K to the unperturbed Kondo temperature. The horizontal axis displays the FP cavity length L, normalized by the characteristic length of the Kondo cloud ξ_K. The experimental data obtained for three cavities of different lengths (1.4 μm, 3.6 μm, and 6.1 μm) collapse into a single universal curve when expressed as a function of ξ_K, demonstrating that this is the relevant length parameter for the phenomenon.

The dashed theoretical curve, derived from NRG calculations, is described by the expression

$$\ln\left(\frac{T_{K,\max}}{T_{K0}}\right) = -n\ln\left(\frac{L}{\xi_K}\right), \tag{15}$$

with $n = 0.47$, indicating that the amplitude of the T_K oscillations decays logarithmically with increasing L. For $L < \xi_K$, a strong perturbation of the Kondo cloud is observed, reflected in significant T_K oscillations. In contrast, for $L > \xi_K$, the FP cavity is outside the cloud's influence region, resulting in less pronounced oscillations. These results constitute direct evidence for the existence and spatial shape of the Kondo cloud, confirming its sensitivity to perturbations within a characteristic length.

2.1.3 Single-impurity Anderson model: local moment formation

The Single Impurity Anderson Model (SIAM), proposed by P. W. Anderson in 1961 (46), was designed to describe the emergence of localized magnetic moments in metallic alloys. These alloys exhibit localized moments, generally associated with d or f orbitals, which, despite being strongly confined spatially, can still interact with the electrons of the host metal through the process of hybridization. To accurately represent the physical phenomena involved in these systems, Anderson formulated a specific Hamiltonian that incorporates these fundamental interactions

$$H = H_{\text{bath}} + H_{\text{imp}} + H_{\text{hyb}} \tag{16}$$

where

$$H_{\text{bath}} = \sum_{k\sigma} \epsilon_k \hat{n}_{k\sigma} \tag{17}$$

where $\hat{n}_{k\sigma}$ is the number operator representing the occupation of the conduction state with momentum k and spin σ, and ϵ_k is the energy of that conduction state. On the other hand

$$H_{\text{imp}} = \sum_{\sigma} \epsilon_d \hat{n}_{d\sigma} + U \hat{n}_{d\uparrow} \hat{n}_{d\downarrow} \tag{18}$$

the term H_{imp} describes the impurity, where ϵ_d is the energy of the discrete and localized impurity level, σ is the spin, and $\hat{n}_{d\sigma}$ is the number operator for the impurity electron with spin σ. The second term, $U \hat{n}_{d\uparrow} \hat{n}_{d\downarrow}$, represents the Coulomb repulsion U between two electrons when the impurity level is doubly occupied, where $\hat{n}_{d\uparrow}$ and $\hat{n}_{d\downarrow}$ are the number operators for spin-up and spin-down electrons, respectively. Finally

$$H_{\text{hyb}} = \sum_{k\sigma} V_k \left(c^\dagger_{k\sigma} d_\sigma + d^\dagger_\sigma c_{k\sigma} \right) \tag{19}$$

here, $c^{\dagger}_{k\sigma}(c_{k\sigma})$ is the creation (annihilation) operator for an electron in the conduction band with momentum k and spin σ, and $d^{\dagger}_{\sigma}(d_{\sigma})$ is the creation (annihilation) operator for an electron in the impurity level with spin σ. The hybridization between the d level and the conduction band constitutes a fundamental interaction that enables the exchange of electrons between these two systems, allowing them to hop from one to the other. The coupling strength associated with this interaction is described by V_k, which, for convenience, will be considered independent of the wave vector k, and thus assumed to be a constant equal to V. Another fundamental term is the so-called Γ, defined as

$$\Gamma = \pi V^2 \rho(E_F) \tag{20}$$

The parameter Γ quantifies the rate of electron transfer between the impurity level and the conduction band of the host metal. In this context, $\rho(E_F)$ represents the density of states of the host metal at the Fermi energy.

The Anderson model has two important limits.

1. The first is the atomic limit, in which we consider only the H_{imp} Hamiltonian. This contains the elements responsible for the formation of localized moments and presents four states, defined by

   a) Not magnetic

$$\begin{cases} |0\rangle \quad ; \quad E_0 = 0 \\ |\uparrow\downarrow\rangle \quad ; \quad E_{\uparrow\downarrow} = 2\varepsilon_d + U \end{cases} \tag{21}$$

   b) Magnetic

$$\begin{array}{lll} |\uparrow\rangle & ; & E_{\uparrow} = \varepsilon_d \\ |\downarrow\rangle & ; & E_{\downarrow} = \varepsilon_d \end{array} \tag{22}$$

   Figure 6 illustrates the electronic phases of the Anderson impurity model in the atomic regime, highlighting the energy conditions (such as $\epsilon_d + U/2, U, -U$) that define these phases. The vertical axis corresponds to the impurity orbital energy, $E_d + U/2$, while the horizontal axis represents the Coulomb repulsion energy, U, which quantifies the energetic cost of placing two electrons in the same orbital.

   The diagram is divided into regions corresponding to distinct electronic states. In the upper-left corner, the Kondo effect (d^0) prevails, where the impurity orbital, either vacant or doubly occupied, hybridizes strongly with the metal's

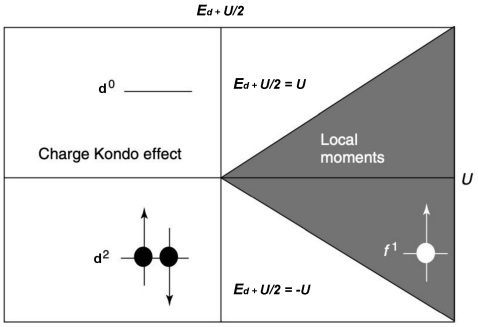

Figure 6 – Representation of electronic phases in the Anderson impurity model considering the atomic regime. From Ref. (7).

conduction electrons. This results in substantial charge fluctuations, producing a state without a net magnetic moment. In the lower-left corner, a mixed-valence state (d^2) dominates, in which the impurity orbital is typically doubly occupied, but its relatively low energy still allows strong hybridization, sustaining charge fluctuations.

A large shaded area on the right represents the local-moment phase. Here, the Coulomb repulsion U is sufficiently strong to prevent double occupancy of the impurity orbital, which is therefore singly occupied (f^1), forming a stable local magnetic moment. The interaction of this moment with conduction electrons can give rise to the Kondo magnetic effect. The transition between the mixed-valence state and the local-moment phase is governed by the competition between hybridization, which favors the mixed-valence regime, and Coulomb repulsion U, which stabilizes the local moment. The boundaries of these phases are approximately defined by the lines $E_d + U/2 = U$ and $E_d + U/2 = -U$.

2. The second limit concerns the formation of a virtual bound state, where a magnetic impurity is placed in contact with a sea of electrons. This interaction occurs through hybridization, described by the Hamiltonian composed of $H_{bath} + H_{hyb}$. The interaction between the localized momentum and the sea of electrons results in the formation of a quasiparticle. In strict quantum mechanical terms, a bound state is generally defined as a state requiring energy to separate its constituent particles, resulting in negative-energy states relative to the continuum and a discrete energy spectrum. The virtual bound state (VBS), however, does not meet this strict definition. Rather, it is considered a resonance phenomenon associated with localized orbitals (such as d or f shells in transition metal impurities) coupled to the continuum of itinerant conduction electrons.

   The VBS corresponds to a localized state whose energy level, instead of being dis-

crete, is broadened into a peak in the local density of states (LDOS) due to hybridization with the metallic host. This broadening is commonly described by a Lorentzian function:

$$\rho_d(\epsilon) = \frac{1}{\pi} \frac{\Delta}{(\epsilon - \epsilon_d)^2 + \Delta^2}, \tag{23}$$

where ϵ_d denotes the effective energy of the impurity level, and Δ represents the characteristic width of the resonance. This width, often referred to as the hybridization width, is defined as

$$\Delta = \pi \rho_0 |V|^2, \tag{24}$$

with ρ_0 being the density of states (DOS) of the conduction electrons at the Fermi level and V the average hybridization matrix element.

The VBS can thus be viewed as an open quantum system, continuously exchanging electrons with the Fermi sea. The imaginary term $i\Delta$ in the denominator of the retarded Green's function, from which the Lorentzian spectral shape arises, indicates a finite lifetime, $\tau \sim 1/\Delta$. This ongoing decay and replenishment, referred to as charge fluctuation is quantitatively captured by Δ.

Finally, the SIAM can be transformed into a low-energy effective model using the Schrieffer–Wolff transformation. In conditions of substantial Coulomb repulsion U, this effective model accurately describes the spin dynamics of the Anderson impurity, forming the foundation for analyzing the Kondo effect.

2.1.4 Introduction to Quantum Dots

QDs are nanoscale structures, typically with dimensions of about 100 nanometers, embedded in semiconductor materials. In these confined regions, the number of free electrons is strongly restricted, ranging from a single electron to a few hundred. It means that electrons within a quantum dot can only occupy discrete energy levels, analogous to the orbitals of an atom. Note that one feature of these nanostructures is the charging energy, which corresponds to the energy required to add or remove an electron from the QD, resembling the ionization process in atoms. Owing to these characteristics, quantum dots are often referred to as "artificial atoms" (47, 48, 49).

Figure 7 presents a schematic representation of a quantum dot. At the center is the system known as the QD, which is connected to the source and drain terminals, linked to instruments for measuring current and voltage. A third terminal represents the gate

electrode (control). By allowing electron tunneling between the source and the drain, the number of electrons N in the QD adjusts until the total energy of the system is minimized. Since electrons are introduced in discrete quantities, the addition of a charge e alters the electrostatic energy, which is conveniently expressed in terms of the capacitance C of the island (or the QD).

A change in the number of charges in a system, such as a QD, causes a modification in its electrostatic potential. This variation is described by the charge energy. This energy derives from the quantization of electronic levels as much as from the Coulomb repulsion between confined electrons, playing a important role in determining the behavior of the system (50).

$$E = \frac{e^2}{C}, \tag{25}$$

where e is the electron charge and C is the total capacitance of the QD. The factor $\frac{1}{2}$ in the expression $\frac{e^2}{2C}$ calculates the work required to charge the capacitor from its neutral state to a charge $Q = ne$, giving n or the number of electrons. Thus, the charging energy represents the energetic cost associated with the insertion of an electron into QD.

This expression accounts for the quantization of energy levels and Coulomb repulsion between confined electrons. When the temperature is sufficiently low and the applied bias voltage is small, the energy cost to add an extra electron to the island may exceed the available thermal energy $k_B T$, that is:

$$k_B T \ll \frac{e^2}{C} \tag{26}$$

where k_B is Boltzmann's constant and T is the temperature. When this situation occurs, the thermal energy available is not enough for the electron to cross the potential barrier and enter the quantum dot QD. Thus, the electric current passing through the quantum dot is blocked by low bias voltages, creating the so-called Coulomb blocking effect. This phenomenon is essential for the functioning of devices that work in the single electron regime, such as single electron transistors.

2.1.5 Kondo effect in quantum dots

The significant advantage of employing quantum dots for the investigation of the Kondo effect, in contrast to metallic counterparts, is rooted in their exceptional tunability and precise parameter control. While in metals the Kondo effect is observed in intrinsic magnetic impurities, quantum dots act as "artificial magnetic impurities," allowing for precise knowledge and control of the number of confined electrons N. This

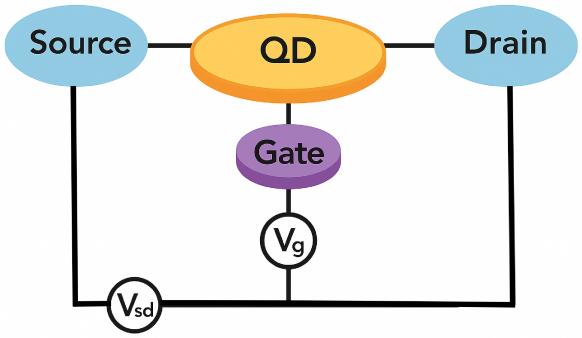

Figure 7 – A schematic representation of a quantum dot connected to the source and drain contacts through tunneling junctions, and to the gate via a capacitor.

capability enables switching between Kondo and non-Kondo regimes by varying N from odd to even, and also allows the adjustment of the T_K through gate voltage. In addition, at sufficiently low temperatures, these spin-flip co-tunneling events form a coherent superposition, ultimately screening the local spin and producing a spin singlet state encompassing both the dot and the electrodes. Note that the characteristic energy scale governing this screening behavior is the Kondo temperature T_K.

The Kondo singlet produces a significant impact on electronic conduction through the QP, manifesting itself as a well-defined resonance peak, $G = dI/dV$, where the voltage polarization is zero ($V = 0$). This anomaly at $V = 0$ constitutes an experimental evidence more consistent with the Kondo effect in QDs (24).

At the Kondo resonance, and for temperatures $T \ll T_K$, the conductance G can reach its maximum value by quantizing the conductance, expressed by:

$$G(V = 0, T = 0) = \frac{2e^2}{h}\tau \approx \frac{2e^2}{h}, \tag{27}$$

where τ represents the transmission factor, which ideally assumes the value $\tau = 1$, and the factor 2 arises from spin degeneracy.

Figure 8, depicts a quantum dot containing a single spin-degenerate energy level, ϵ_0, occupied by one electron and illustrates the fundamental co-tunneling processes responsible for the conventional spin-1/2 Kondo effect in a quantum dot with an odd number of electrons (N odd), representing the canonical example of this phenomenon in artificial systems. It means that the dot carries a net half-integer spin ($S = 1/2$). Although ϵ_0 is situated well below the Fermi levels of the neighboring leads (μ_L and μ_R), therefore suppressing direct first-order tunneling due to Coulomb blockade, higher-order tunneling mechanisms, known as co-tunneling, remain possible.

It appears that these co-tunneling processes involve virtual, high-energy intermediate states (depicted in orange in Fig. 8), where an electron transiently tunnels on or off the dot

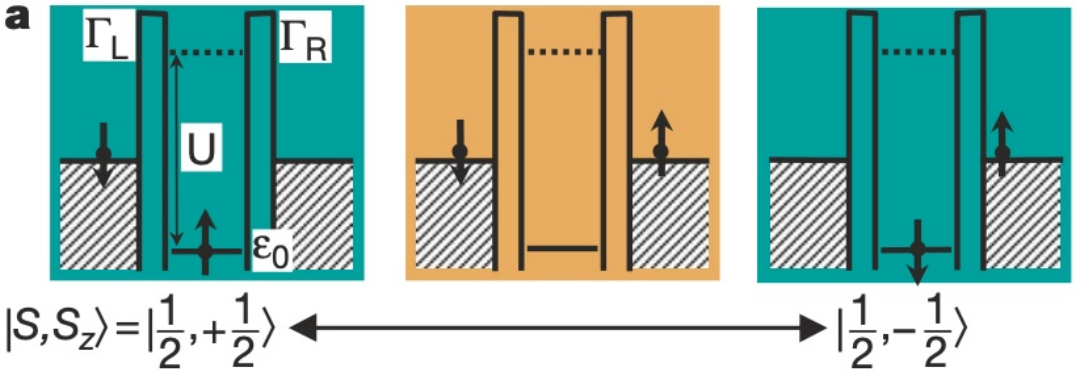

Figure 8 – Spin inversion processes give rise to the ordinary and singlet Kondo effects in a quantum dot with spin-1/2 and an odd number of electrons N. The highest-energy electron occupies the spin-degenerate level ϵ_0, and the ground states with $S_z = \pm\frac{1}{2}$ (green panels) are connected by co-tunneling events through barriers with rates Γ_L and Γ_R. From Ref. (8)

at an energy cost approximately equal to U, the on-site Coulomb energy. Actually, such processes can induce spin flips of the confined electron, for example, a spin-up electron may tunnel out of the dot and be promptly replaced by a spin-down electron from the leads. At low temperatures, a coherent superposition of all possible spin-flip co-tunneling events leads to screening of the localized spin on the dot by conduction electrons from the leads. Hence, the resulting many-body entangled state, a spin singlet, characterizes the Kondo effect.

2.1.5.1 Experimental observations

Figure 9 illustrates the conductance in the linear-response regime ($G = I/V$) of a quantum dot as a function of gate voltage (V_g) at two electron temperatures: 45 mK (solid line) and 150 mK (dashed line). By varying V_g, the electrostatic potential of the dot is tuned, controlling the number of confined electrons (N), with each Coulomb blockade oscillation corresponding to the addition of a single electron. In the valleys between conductance peaks, where transport is suppressed, the parity of N can be inferred from the spacing between peaks and supported by magnetic field measurements. A clear temperature-dependent distinction is observed: valleys with odd N (e.g., 3, 5, 7) display higher conductance at the lower temperature, which decreases as temperature increases, reflecting Kondo screening of a localized spin. In contrast, even-N valleys (e.g., 2, 4, 6) show conductance that rises with temperature, indicative of thermally activated transport without Kondo correlations. This alternating pattern between odd and even valleys demonstrates the tunable nature of the Kondo effect in quantum dot systems.

Another key experimental signature of the Kondo effect in quantum dots is the zero-bias anomaly in the differential conductance (dI/dV) when a bias voltage (V) is applied

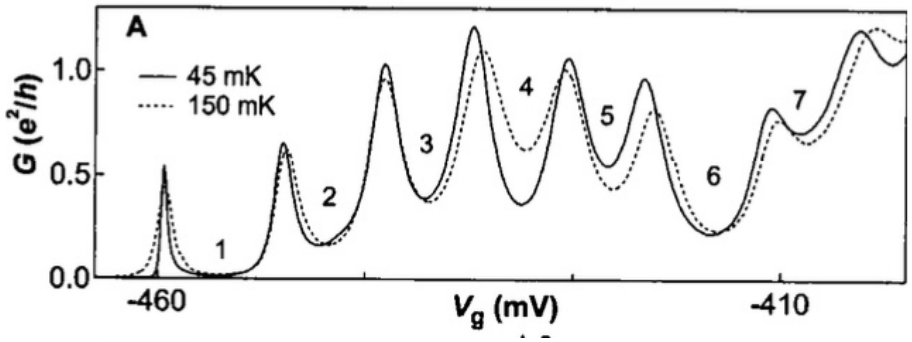

Figure 9 – The linear conductance, defined as $G = I/V$, was recorded as a function of the voltage applied to the gate (V), at point 1, under a null magnetic field ($B = 0$), for a voltage of 7.9 mV. The measurements were performed at two different temperatures: 45 mK, represented by the solid line, and 150 mK, indicated by the dashed line. Planck's constant (h) is used as a reference. From Ref. (9).

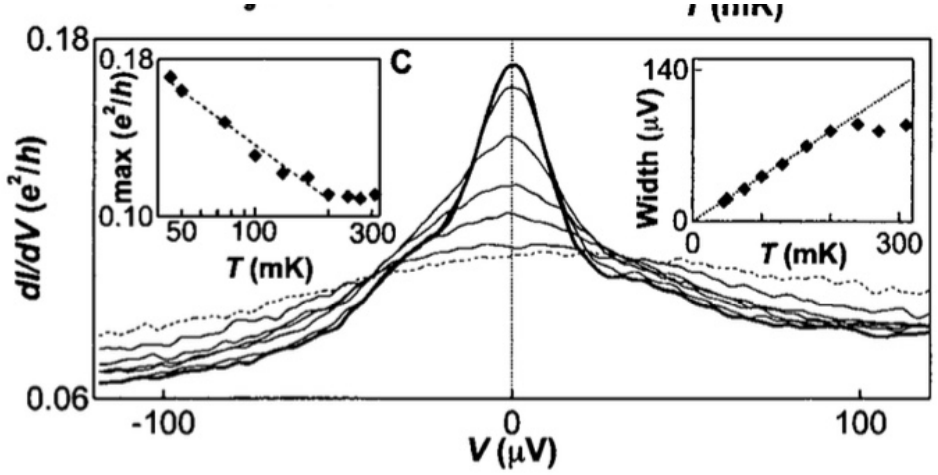

Figure 10 – The differential conductance dI/dV was measured at different temperatures (45 to 270 mK), with the gate voltage centered in the intermediate valley. The observed peak grows logarithmically with temperature, while its width increases linearly, with a slope of 4.8 kB. The asymmetry in the peak at zero bias indicates a difference between Γ_L and Γ_R coupling. From Ref. (9)

between source and drain. This anomaly appears as a pronounced peak at zero bias. Fig. 10 illustrates dI/dV versus source-drain voltage (V_{sd}) at various temperatures (45 mK to 270 mK), measured at the center of a "Kondo valley" (i.e., for an odd number of electrons).

At the base temperature of 45 mK (bold curve), a sharp peak appears at $V_{sd} = 0$, representing the Kondo resonance, which can be seen as a narrow feature in the dot's density of states pinned to the leads' Fermi energies. This resonance enhances conductance at zero bias. As temperature rises, the peak broadens and decreases in height, vanishing at higher temperatures (e.g., 270 mK), reflecting the progressive disruption of coherent Kondo screening by thermal fluctuations. The logarithmic temperature dependence of

the peak maximum is a hallmark of the Kondo effect for $T \lesssim T_K$, and the peak width saturates near T_K at very low temperatures. Observing this zero-bias anomaly and its characteristic temperature behavior provides strong evidence for the formation of the many-body Kondo singlet in the quantum dot.

Chapter 3

The Numerical Renormalization Group Approach

In materials with strong correlations, single-particle approximations fail and are not able to describe the correct physics. For quantum impurity systems, a complete description requires the use of non-perturbative theories. In this context, the method commonly employed is the NRG. In quantum impurity systems, the NRG is applied with the aim of determining the many-body eigenvalues and eigenstates across different energy scales $\omega_1 < \omega_2 < \ldots$, through a series of successive steps. Each of these steps is associated with a specific scale, either in energy or in length.

The aim is to proceed through the elimination of high-energy states so as to construct effective Hamiltonians H_N (with $N = 0, 1, \ldots$). In doing so, one hopes to capture the relevant physics of the system at increasingly reduced energy scales ω_N, though the accuracy of such a description may depend on subtle assumptions and approximations (51, 41). Mathematically, this is described by

$$H_{N+1} = R[H_N], \tag{28}$$

In Eq. 28, the renormalization operation R can be seen as a way of connecting effective Hamiltonians that account for physical behavior across distinct energy scales. During the 1970s, Kenneth Wilson introduced a non-perturbative formulation of the Renormalization Group (RG) applied to the Kondo model. This method made it possible to follow, step by step, the crossover from weak coupling at high temperatures to the strong coupling regime that dominates at low temperatures. In this chapter, we describe a specific implementation of the NRG idea: Wilson's nonperturbative method for the Anderson model.

3.1 Logarithmic discretization

In the context of the Kondo problem (and, to some extent, in other scenarios involving quantum impurities) the system does not behave uniformly across energy scales. Instead, its qualitative features shift in ways that can be quite dramatic. One might say that this evolution reflects a passage between distinct fixed points of the RG. At elevated temperatures, the system tends to display the familiar traits of a localized magnetic moment, almost as if the impurity were standing alone. On the other hand when the temperature drops below T_K, the description changes: the system begins to resemble a Fermi liquid, with the impurity effectively screened. Wilson's approach offers a non-perturbative framework for the RG that remains applicable across the full range of energy scales.

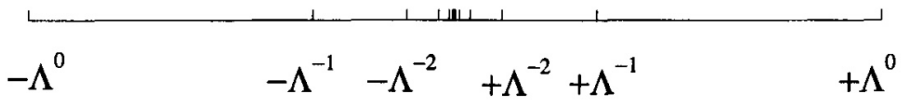

Figure 11 – Schematic representation of the Logarithmic discretization of the conduction band.

Wilson's formulation relies on a logarithmic discretization of the energy axis, governed by a parameter $\Lambda > 1$. Rather than treating the band in its original form, the conduction states are restricted into the interval ([-1,1]), which is then split into two parts, positive and negative, so that the impurity's influence can be tracked more carefully. What stands out, is that the accuracy of the transformation remains constant throughout all iterations, unaffected by the strength of the couplings. The discretization intervals are given by

$$D_n^+ = [\Lambda^{-(n+1)}, \Lambda^{-n}], \quad D_n^- = [-\Lambda^{-n}, -\Lambda^{-(n+1)}], \tag{29}$$

taking into account the discrete values $n = 0, 1, \ldots$, which lie near the Fermi level $\epsilon_F = 0$ (see Fig. 11), one should note that orbital isotropy is assumed. In practice, this means that only electrons with s-wave symmetry are allowed to interact with the impurity, as suggested in Figure 12 (11). Under these conditions the Anderson Hamiltonian can be written in its continuous form as

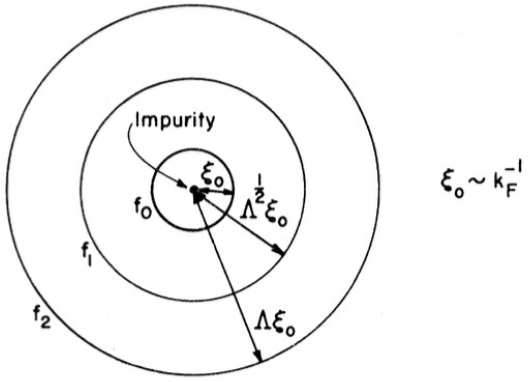

Figure 12 – Illustration of spherical regions in radial space r, which indicate the boundaries of the wave functions f_n. Each of these functions oscillates within its respective region, ensuring that they are orthogonal to each other. From Ref. (10).

$$H = H_{\text{imp}} + \sum_{\sigma} \int_{-1}^{1} d\epsilon \, g(\epsilon) \, a^{\dagger}_{\epsilon\sigma} a_{\epsilon\sigma} + \sum_{\sigma} \int_{-1}^{1} d\epsilon \, h(\epsilon) \left(f^{\dagger}_{\sigma} a_{\epsilon\sigma} + a^{\dagger}_{\epsilon\sigma} f_{\sigma} \right). \tag{30}$$

Equation 30 sets the cutoffs over the interval $[-1, 1]$. Where $g(\epsilon)$ denotes the dispersion, while $h(\epsilon)$ captures the hybridization. According to the analysis by Bulla, Pruschke, and Hewson (1997) (52), the hybridization function $\Delta(\omega)$ can be written explicitly in terms of $h(\epsilon)$ and $g(\epsilon)$ as:

$$\Delta(\omega) = \frac{1}{\pi} \cdot \frac{d\epsilon(\omega)}{d\omega} \cdot \left[h\left(\epsilon(\omega)\right) \right]^2, \tag{31}$$

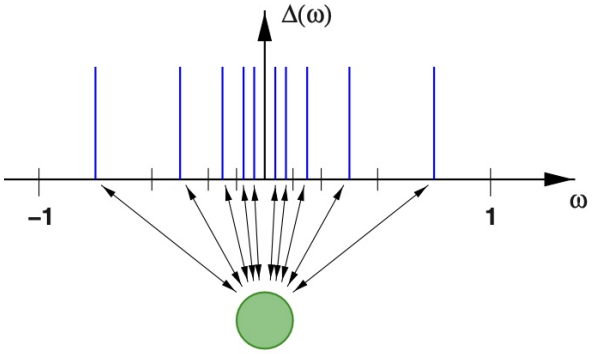

Figure 13 – A single state serves as an approximation of the continuous spectrum in each interval. From Ref. (11).

in this way, establishing a connection between $g(\epsilon)$ and $h(\epsilon)$, where $\epsilon(\omega)$ is the energy of the conduction electron that satisfies $g[\epsilon(\omega)] = \omega$, corresponding to the frequency ω of

the Hamiltonian, we introduce within each interval D_n, as schematically depicted in Fig. 13, a complete set of orthonormal functions given by

$$\psi_{np}^{\pm}(\varepsilon) = \begin{cases} \frac{1}{\sqrt{d_n}}\, e^{\pm i\omega_{np}\varepsilon}, & \text{if } \Lambda^{-(n+1)} < \pm\varepsilon < \Lambda^{-(n)} \\ 0, & \text{outside of the interval} \end{cases} \tag{32}$$

where the parameter p ranges from $-\infty$ to ∞, and within this domain the fundamental frequencies are expressed as

$$\omega_n = \frac{2\pi}{d_n} \tag{33}$$

in which $d_n = \Lambda^{-n}(1-\Lambda^{-1})$ is the width of the interval. By considering the basis functions $\psi_{np}^{\pm}(\varepsilon)$, the conduction-electron operators can be expanded as

$$a_{\varepsilon\sigma} = \sum_{np} \left[a_{np\sigma}\psi_{np}^{\dagger}(\varepsilon) + b_{np\sigma}\psi_{np}(\varepsilon) \right]. \tag{34}$$

This can be understood as the performance of a Fourier expansion within each segment. The inverse operation is given by

$$a_{np\sigma} = \int_{-1}^{1} d\varepsilon \, \left[\psi_{np}^{+}(\varepsilon)\right]^{*} a_{\varepsilon\sigma} \tag{35}$$

and

$$b_{np\sigma} = \int_{-1}^{1} d\varepsilon \, \left[\psi_{np}^{-}(\varepsilon)\right]^{*} a_{\varepsilon\sigma}. \tag{36}$$

With the simplifications proposed above, the Hamiltonian in Eq. 30 can be written in a discretized form. A key aspect of Wilson's formulation is the observation that only states with $p = 0$ couple directly to the impurity. Consequently, without loss of accuracy, states with $p = 1, 2, \ldots$, which are not located near the impurity, can be neglected. These states are centered farther away, specifically at a distance $r \approx \Lambda^{p}$ from the impurity, and therefore couple to it only indirectly. Another essential element is the treatment of the function $h(\epsilon)$, which must be considered constant within each interval, even if $\Delta(\epsilon)$ is not constant in general. Following the formulation by Bulla (52), $h(\epsilon)$ is assumed to be a step function, i.e., constant within each subinterval of the discretization.

$$h(\varepsilon) = h_n^{\pm}, \quad x_{n+1} < \pm\varepsilon < x_n, \tag{37}$$

this leads to the following expression for the hybridization term

$$\int_{-1}^{1} d\epsilon\, h(\epsilon) f_\sigma^\dagger a_{\epsilon\sigma} = \frac{1}{\sqrt{\pi}} f_\sigma^\dagger \sum_n \left(\gamma_n^+ a_{n0\sigma} + \bar{\gamma}_n b_{n0\sigma}\right), \tag{38}$$

with

$$\gamma_n^{\pm 2} = \int^{\pm,n} d\varepsilon\, \Delta(\varepsilon), \tag{39}$$

where

$$\int^{+,n} d\varepsilon \equiv \int_{x_{n+1}}^{x_n} d\varepsilon, \qquad \int^{-,n} d\varepsilon \equiv \int_{-x_n}^{-x_{n+1}} d\varepsilon. \tag{40}$$

First, we examine the term associated with the conduction electrons, which can be rewritten as

$$\begin{aligned} \int_{-1}^{1} d\epsilon\, g(\epsilon)\, a_{\varepsilon_0}^\dagger a_{\varepsilon_0} &= \sum_{n,p} \left(\xi_n a_{np\sigma}^\dagger a_{np\sigma} + \xi_n b_{np\sigma}^\dagger b_{np\sigma}\right) \\ &+ \sum_{n,\, p\neq p'} \left[a_n^\dagger(p,p') a_n^\dagger(p',\sigma) - a_n(p,p') b_{np\sigma}^\dagger b_{np'\sigma}\right]. \end{aligned} \tag{41}$$

The initial term on the right-hand side of Eq. 41 is diagonal with respect to the index p. Therefore, the discrete set of energy levels $\xi_n^{\pm}$ can be represented as described by Bulla, Pruschke, and Hewson (52) as

$$\xi_n^{\pm} = \frac{\int_{\pm,n} d\varepsilon\, \Delta(\varepsilon)\varepsilon}{\int_{\pm,n} d\varepsilon\, \Delta(\varepsilon)} = -\frac{1}{2}\Lambda^{-n}(1+\Lambda^{-1}). \tag{42}$$

The expression in parentheses corresponds to the case in which $\Delta(\varepsilon)$ is assumed to be constant. Nevertheless, the coupling between conduction electrons with indices p and p', which characterizes how the electronic states reconnect to the continuum, is exact at this stage, since no approximation has yet been introduced. Second, by considering a linear dispersion relation of the form $\varepsilon_k = k$, the matrix elements $\alpha_{pp'}$ for $(p \neq p')$ take identical values for both positive and negative p, and are described by

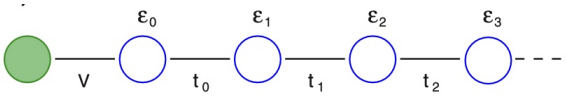

Figure 14 – The discretized model is reformulated as a semi-infinite chain, in which the impurity interacts with the first conduction electron site through the hybridization term V. The tight-binding parameters of this representation are denoted by ϵ_n and t_n (the hopping between sites in the chain that represents the bath, see Eq. 50).

$$\alpha_n^{\frac{1}{2}}(p,p') = \frac{1-\Lambda^{-1}}{2\pi i}\cdot\frac{\Lambda^{-n}}{p'-p}\exp\left(\frac{2\pi i(p'-p)}{1-\Lambda^{-1}}\right). \tag{43}$$

The discretized Hamiltonian is obtained by disregarding all terms with $p \neq 0$ in Eq. 41, a crucial simplification that isolates the conduction states most directly coupled to the impurity. Following this step, and upon substituting $a_{n0\sigma} \equiv a_{n\sigma}$, the discretized Hamiltonian is finally obtained

$$\begin{aligned} H = H_{\text{imp}} &+ \sum_{n\sigma}\left(\xi_n^\dagger a_{n\sigma}^\dagger a_{n\sigma} + \xi_n b_{n\sigma}^\dagger b_{n\sigma}\right) \\ &+ \frac{1}{\sqrt{\pi}}\sum_\sigma f_\sigma^\dagger \sum_n \left(\gamma_n a_{n\sigma} + \gamma_n b_{n\sigma}\right) \\ &+ \frac{1}{\sqrt{\pi}}\left(\sum_n\left(\gamma_n a_{n\sigma}^\dagger + \gamma_n b_{n\sigma}^\dagger\right)\right) f_\sigma \end{aligned} \tag{44}$$

3.2 Linear chain

In order to proceed with the analysis, the discretized Hamiltonian in Eq. 44 is arranged in a linear chain form through the Lanczos transformation, we then have a more systematic and tractable way to investigate the dynamics of the system. Which implies that a sequence of steps must be followed

1. The first site of the chain corresponds to the impurity (see Fig. 14), while the subsequent sites represent the conduction band. The impurity couples only to the first site in the chain, represented by the operators $c_{0\sigma}^\dagger$, where

$$c_{0\sigma} = \frac{1}{\sqrt{\xi_0}}\sum_n\left(\gamma_n^+ a_{n\sigma} + \bar{\gamma}_n b_{n\sigma}\right), \tag{45}$$

in addition, the normalization condition is expressed as

$$\xi_0 = \sum_n \left[(\gamma_n^+)^2 + (\bar{\gamma}_n^-)^2\right] = \int_{-1}^{1} d\varepsilon\, \Delta(\varepsilon). \tag{46}$$

From Eq. 45, the hybridization can be written as

$$\frac{1}{\sqrt{\pi}} f_\sigma^\dagger \sum_n \left(\gamma_n^+ a_{n\sigma} + \bar{\gamma}_n b_{n\sigma}\right) = \sqrt{\frac{\xi_0}{\pi}} f_\sigma^\dagger c_{0\sigma}, \tag{47}$$

and considering $V_k = V$ (with V independent of k), we have

$$V = \sqrt{\frac{\xi_0}{\pi}}. \tag{48}$$

2. The operators $C_{0p}^\dagger$ are not inherently orthogonal to the operators $a_{n\sigma}^\dagger$ and $b_{n\sigma}^\dagger$. Orthogonality is subsequently enforced via a tridiagonalization procedure, through which a novel set of mutually orthogonal operators, $c_{n\sigma}^\dagger$, is systematically constructed from $a_{n\sigma}^\dagger$ and $b_{n\sigma}^\dagger$. In addition, the chain Hamiltonian can be expressed as

$$H = H_{\text{imp}} + \sqrt{\tfrac{\xi_0}{\pi}} \sum_\sigma \left(f_\sigma^\dagger c_{0\sigma} + c_{0\sigma}^\dagger f_\sigma\right) + \sum_{n=0}^{\infty} \left[\varepsilon_n c_{n\sigma}^\dagger c_{n\sigma} + t_n \left(c_{n\sigma}^\dagger c_{n+1,\sigma} + c_{n+1,\sigma}^\dagger c_{n\sigma}\right)\right], \tag{49}$$

In Eq. 49, we represent the single-impurity Anderson model (SIAM) expressed in its one-dimensional chain representation. Therefore, the Hamiltonian has three distinct contributions:

a) H_{imp}, which describes the isolated impurity, including its on-site energy and Coulomb interaction.

b) The hybridization term, $\sqrt{\frac{\xi_0}{\pi}} \sum_\sigma \left(f_\sigma^\dagger c_{0\sigma} + c_{0\sigma}^\dagger f_\sigma\right)$, which couples the impurity orbital f_σ to the first site of the conduction chain, $c_{0\sigma}$, enabling spin exchange between the impurity and the conduction electrons.

c) The chain contribution, $\sum_{n=0}^{\infty} \left[\varepsilon_n c_{n\sigma}^\dagger c_{n\sigma} + t_n \left(c_{n\sigma}^\dagger c_{n+1,\sigma} + c_{n+1,\sigma}^\dagger c_{n\sigma}\right)\right]$, describing the conduction electrons mapped onto a linear chain. Here, ε_n denotes the on-site energy of the n-th site, while t_n is the hopping amplitude between adjacent sites. For a logarithmic discretization with constant hybridization, t_n

decays exponentially with n, reflecting the reduced energy scale of successive sites along the chain

$$t_n = \frac{(1+\Lambda^{-1})(1-\Lambda^{-n-1})}{2\sqrt{1-\Lambda^{-2n-1}}\sqrt{1-\Lambda^{-2n-3}}}\Lambda^{-n/2}. \tag{50}$$

This representation is especially amenable to NRG calculations, as the exponential attenuation of the hopping amplitudes facilitates a controlled, iterative treatment of the system across progressively lower energy scales.

3.3 Iterative diagonalization

A RG transformation, defined by the relationship between Hamiltonians at successive energy scales $\Lambda^{n/2}$ and $\Lambda^{-(n+1)/2}$, can be formulated as follows

1. The Hamiltonian in Eq. 49 is truncated to N orbitals, yielding H_N, which is defined as

$$H = \lim_{N\to\infty} \Lambda^{-(N-1)/2} H_N, \tag{51}$$

where

$$H_N = \Lambda^{(N-1)/2}\Bigg(H_{\text{imp}} + \sqrt{\frac{\xi_0}{\pi}}\sum_{\sigma}\left(f_\sigma^\dagger c_{0\sigma} + c_{0\sigma}^\dagger f_\sigma\right) + \sum_{\sigma,n=0}^{N}\epsilon_n c_{n\sigma}^\dagger c_{n\sigma} + \sum_{n=0}^{N} t_n\left(c_{n\sigma}^\dagger c_{n+1\sigma} + c_{n+1\sigma}^\dagger c_{n\sigma}\right)\Bigg). \tag{52}$$

The prefactor $\Lambda^{(N-1)/2}$ defines a rescaled Hamiltonian, removing the explicit N-dependence of the hopping parameter t_{N-1} and thereby facilitating the analysis of the Hamiltonian's fixed points.

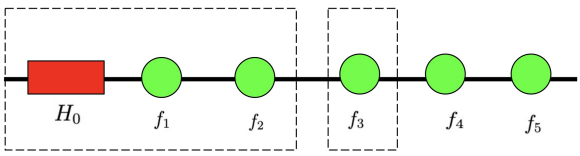

Figure 15 – Iterative procedure of diagonalization of the H operator, starting with H_0 and gradually expanded with the orbitals f_1, f_2, and so on.

2. Two successive Hamiltonians are connected according to

$$H_{N+1} = \sqrt{\Lambda} H_N + \Lambda^{N/2} \sum_\sigma \varepsilon_{N+1} c^\dagger_{N+1\sigma} c_{N+1\sigma} + \Lambda^{N/2} \sum_\sigma t_N \left(c^\dagger_{N\sigma} c_{N+1\sigma} + c^\dagger_{N+1\sigma} c_{N\sigma} \right). \tag{53}$$

Within the RG framework, Hamiltonians are parametrized by a set of parameters $\vec{K}$. The mapping R transforms the original Hamiltonian into a new Hamiltonian defined by an updated set of parameters $\vec{K}'$, such that

$$H_{N+1} = R H_N. \tag{54}$$

This conceptual framework provides the basis for the iterative diagonalization of the Anderson Hamiltonian, as schematically illustrated in Figure 15. The subsequent procedure for obtaining the spectrum of the Hamiltonian, H_0, is then described as

a) The first Hamiltonian is given by

$$H_0 = \Lambda^{-1/2} \left(H_{\text{imp}} + \sum_\sigma \varepsilon_0 c^\dagger_{0\sigma} c_{0\sigma} + \sqrt{\frac{\xi_0}{\pi}} \sum_\sigma \left(f^\dagger_\sigma c_{0\sigma} + c^\dagger_{0\sigma} f_\sigma \right) \right), \tag{55}$$

this Hamiltonian represents a system composed of two sites: the impurity site and the first site of the conduction electron band.

b) Second, we assume that H_N has already been diagonalized, with the many-body energies given by

$$H_N \left| r \right\rangle_N = E_N(r) \left| r \right\rangle_N, \quad r = 1, \ldots, N_s, \tag{56}$$

where $|r\rangle_N$ are the eigenstates of H_N and N_s is the dimension of H_N. The idea now is that, from the spectrum of H_N, it is possible to construct a basis for H_{N+1}.

$$|r; s\rangle_{N+1} = |r\rangle_N \otimes |s(N+1)\rangle, \tag{57}$$

The states $|\, r's'; s'\rangle$ are product states, consisting of the basis of H_N and a new basis $|s(N+1)\rangle$ that represents the newly added site. Based on Eq. 57 it is then possible to construct H_{N+1}

$$H_{N+1}(rs, r's') = \langle rs \,|\, H_{N+1} \,|\, r's' \rangle_{N+1}, \tag{58}$$

by diagonalizing Eq. 58, we obtain the new eigenvalues $E_{N+1}(w)$ and the corresponding eigenstates $|w\rangle_{N+1}$. By repeating this procedure successively, as illustrated in Figure 15, we obtain the complete spectrum.

3.4 Renormalization group flow and fixed points

The iterative diagonalization procedure yields the energies of the many-body states $E_N(r)$, with $r = 1, \ldots, N_s$. In the initial steps, the number of states is smaller than N_s, until the truncation mechanism is applied. The index N runs from 0 up to a maximum value $N_{\max}$, chosen such that the system lies sufficiently close to its fixed point corresponding to the low-temperature regime.

The many-body energy spectra remain approximately within the same range for different values of N, owing to the scaling factor $\Lambda^{(N-1)/2}$. The first excited state of H_N has an energy on the order of $\Lambda^{(N-1)/2} t_{N-1}$, while the highest excited state after truncation depends on N_s and is typically 5 to 10 times larger than the lowest energy. When rescaled by $\Lambda^{-(N-1)/2}$, the energies $E_N(r)$ approximate the many-body spectrum of the chain Hamiltonian, within an energy window that decreases exponentially with N. As a consequence of iterative truncation, only a subset of the lowest-energy states from each iteration is retained to construct the subsequent Hamiltonian, leading to the progressive elimination of high-energy excitations from the original system.

Figure 16 shows an example of multiparticle energy levels for the symmetric Anderson model with a single impurity. The energies are plotted for odd values of N. The energies are identified by the total charge Q and the total spin S. In this diagram, three fixed points can be identified:

1. For $N \approx 3 - 9$, the system is close to the free-orbital fixed point. This can be verified by setting $U = 0$ and $V = 0$. This is an unstable fixed point.

2. For $N \approx 20 - 50$, the system approaches the local-moment fixed point, which is also an unstable fixed point.

3. For $N > 50$, the system reaches the strong-coupling fixed point, a regime in which the impurity is screened by the conduction electrons. This fixed point is obtained by considering $V \to \infty$.

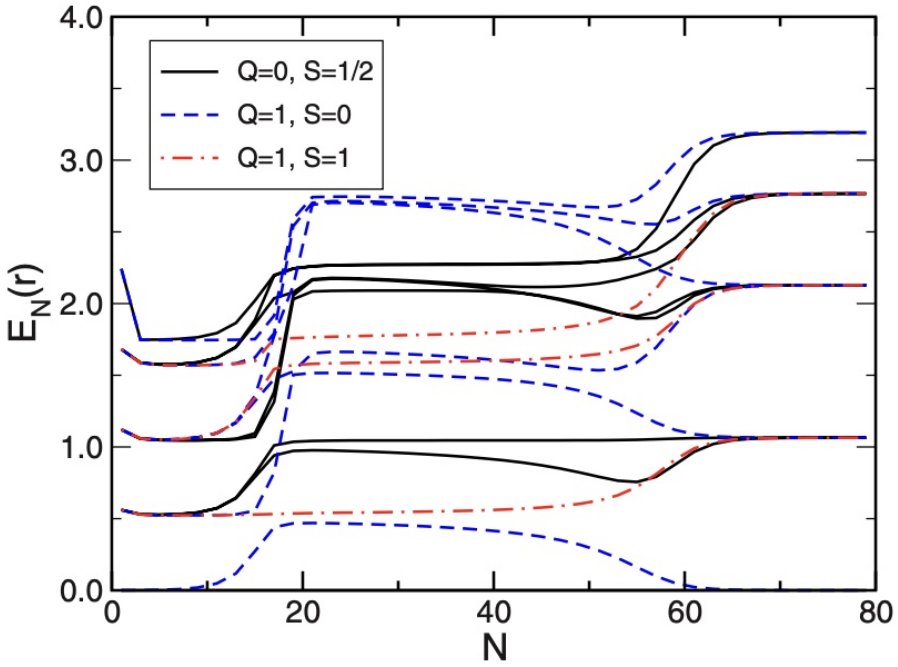

Figure 16 – Evolution of the lowest energy levels of the Anderson model with a single impurity, for the parameters $f = -0.5 \times 10^{-3}$, $U = 10^{-3}$, $V = 0.004$, and $\Gamma = 2.5$. The states are identified by the quantum numbers of total charge Q and total spin S.

3.5 Applications

The applications of the NRG method in quantum impurity systems encompass three principal aspects: the analysis of the system's fixed points, the evaluation of its thermodynamic properties, and the investigation of its dynamical and transport characteristics.

3.5.1 Thermodynamic Quantities: Entropy, Specific Heat, and Susceptibility

The simplest physical quantities associated with the impurity degrees of freedom are the impurity contributions to the entropy S_{imp}, the specific heat C_{imp}, and the magnetic susceptibility χ_{imp}. Specifically, the entropy and the specific heat correspond to the first derivatives of the free energy, $F = -k_B T \ln Z$, and the internal energy, $U = \langle H \rangle$, with respect to temperature, respectively, that is,

$$S = -\frac{\partial F}{\partial T}, \qquad C = \frac{\partial U}{\partial T}. \tag{59}$$

From a numerical point of view, performing direct differentiations should be avoided whenever possible. Another difficulty arises in the NRG: to avoid exponential energy growth,

it is necessary to subtract the ground state energy at each NRG level, requiring control of these subtractions. A more convenient way is to evaluate the derivative analytically, obtaining

$$\frac{S}{k_B} = \beta\langle H\rangle + \ln Z \tag{60}$$

for entropy and

$$\frac{C}{k_B} = \beta^2\left(\langle H^2\rangle - \langle H\rangle^2\right) \tag{61}$$

for specific heat.

Other local properties typically require the calculation of correlation functions. In this context, it is necessary to distinguish between real-time correlators and susceptibilities. Calculating the impurity contribution to isothermal magnetic susceptibility requires more careful consideration. The standard definition for the isothermal magnetic susceptibility (assuming $g\mu_B = 1$) is

$$\chi(T) = \int_0^\beta \langle S_z(\tau)S_z\rangle\, d\tau - \beta\langle S_z\rangle^2, \tag{62}$$

where τ is the imaginary time ($0 < \tau < \beta$), S_z is the z component of the impurity spin operator, and

$$\langle S_z(\tau)S_z\rangle = \frac{1}{Z}\,\mathrm{Tr}\Big(e^{-\beta H}e^{\tau H}S_z e^{-\tau H}S_z\Big)\,. \tag{63}$$

In general, experimental measurements yield the global susceptibility of the system. By exploiting the fact that the total spin operator commutes with the Hamiltonian, one can express

$$\langle S_{\mathrm{tot},z}[\tau]\, S_{\mathrm{tot},z}\rangle = \langle S_{\mathrm{tot},z}\, S_{\mathrm{tot},z}\rangle\,. \tag{64}$$

and therefore arrive at the following expression.

$$\chi_{\mathrm{tot}}(T) = \beta\Big(\langle S^2_{\mathrm{tot},z}\rangle - \langle S_{\mathrm{tot},z}\rangle^2\Big), \tag{65}$$

by subtracting the susceptibility of the system in the absence of the impurity, one arrives at Wilson's definition of the impurity contribution to the susceptibility.

$$\chi_{\text{imp}}(T) = \chi_{\text{tot}}(T) - \chi^{(0)}_{\text{tot}}(T). \tag{66}$$

Since $S_{\text{tot},z}$ and $S_{\text{tot},z}$ defines the states, the values of Eq. 66 are directly accessible. Analogously, one obtains the impurity contributions to the entropy and the specific heat.

$$S_{\text{imp}}(T) = S_{\text{tot}}(T) - S^{(0)}_{\text{tot}}(T), \tag{67}$$

and

$$C_{\text{imp}}(T) = C_{\text{tot}}(T) - C^{(0)}_{\text{tot}}(T), \tag{68}$$

where $S^{(0)}_{\text{tot}}(T)$ and $C^{(0)}_{\text{tot}}(T)$ represent, respectively, the entropy and the specific heat of the reference system without impurities. Figure 17 shows the dependence of $T\chi(T)$ as a function of temperature T for the symmetric Anderson model, considering two ratios $U/\pi\Gamma$, equal to 12 and 1, represented by solid and dashed curves, respectively. For $U \gg \pi\Gamma$, the presence of a well-defined local moment regime around $T \approx 1/4$ is observed, delimited by the free orbital regime, characterized by $T\chi = 1/8$, and by the strong coupling regime, in which the susceptibility remains constant.

3.5.2 Dynamics quantities

The NRG can also be used to calculate the dynamical properties of quantum impurity models. As an example, the impurity spectral function is given by

$$A_\sigma(\omega, T) = -\frac{1}{\pi} \operatorname{Im} G_\sigma(\omega, T), \tag{69}$$

where $G_\sigma(\omega, T)$ denotes the impurity Green's function. Suppose that all eigenvalues $E_N(r)$ and many-body eigenstates $|r\rangle$ of the Anderson Hamiltonian are known. In the Lehmann representation, the impurity Green's function is

$$G_\sigma(\omega, T) = \frac{1}{Z(T)} \sum_{r,r'} |\langle r|f_\sigma|r'\rangle|^2 \, \frac{e^{-E_r/k_BT} + e^{-E_{r'}/k_BT}}{\omega - (E_{r'} - E_r)}, \tag{70}$$

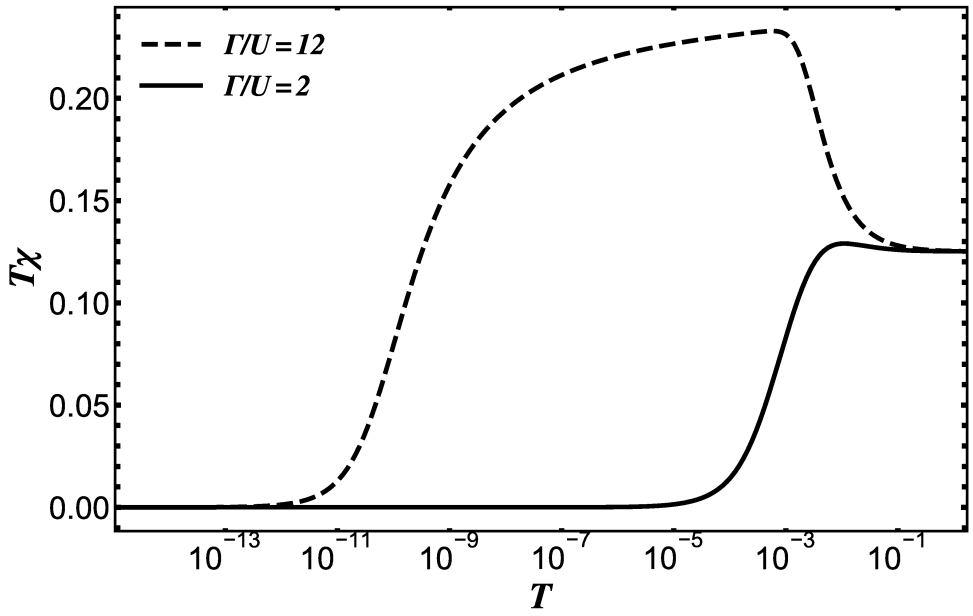

Figure 17 – Plots of $T\chi(T)$ as a function of T for the symmetric Anderson model with $U = 0.01$, considering $U/\pi\Gamma = 12$ (solid curve) and 1 (dashed curve). In the case of $U \gg \pi\Gamma$ (12), a well-defined local moment regime ($T \approx 1/4$) is observed, situated between the free orbital regime ($T\chi = 1/8$) and the strong coupling regime (constant χ). When $U \to \pi\Gamma$, a direct transition from the free orbital regime to the strong coupling regime occurs.

and the corresponding spectral function is

$$A_\sigma(\omega, T) = \frac{1}{Z(T)} \sum_{r,r'} |M_{r,r'}|^2 \left(e^{-E_r/k_BT} + e^{-E_{r'}/k_BT}\right) \delta(\omega - (E_{r'} - E_r)) \,, \tag{71}$$

where $M_{r,r'} = \langle r|f_\sigma|r'\rangle$. At $T = 0$, one obtains

$$A_\sigma(\omega, 0) = \frac{1}{Z(0)} \sum_{r} |M_{r,0}|^2 \, \delta(\omega + E_r - E_0) + \frac{1}{Z(0)} \sum_{r'} |M_{0,r'}|^2 \, \delta(\omega - E_{r'} + E_0) \,, \tag{72}$$

where E_0 denotes the ground-state energy. The impurity spectral function is obtained by considering a sequence of Hamiltonians H_N (with $N = 0, 1, 2, \ldots$). While the Lehmann representation involves a sum over all many-body states, in the NRG this sum is restricted to the truncated many-body eigenstates of H_N. At $T = 0$, the sum in Eq. 72 involves transitions from the ground state E_0 to all available excited states (11), yielding

$$A_\sigma(\omega, 0) \approx A_\sigma^N(\omega, 0). \tag{73}$$

To compute $A_{d,\mu}(\omega, 0)$, a typical frequency $\omega = 2\omega_N$ is chosen, with $\omega_N = k_B T_N$, allowing analysis at progressively smaller frequencies. The interest lies not in the discrete spectra of the Hamiltonians H_N, but in continuous spectra comparable to experimental results. To this end, the delta functions $\delta(\omega - E_n^N)$ are replaced by smooth functions $P_N(\omega - E_n^N)$, with width η_N typically of the order of the characteristic energy scale D_N. The most commonly employed distributions are the Gaussian and the logarithmic Gaussian.

Peaks with intrinsic width Γ are well resolved when $\Gamma \gg \eta$, as in the case of the Kondo resonance. At high frequencies, however, logarithmic resolution may fail to accurately capture the line shape of the peaks, which generally reflect single-particle processes and require alternative approaches, such as in two-state ohmic systems or strongly correlated networks. In Fig. 18, the spectral function of a magnetic impurity is represented by two curves. The solid black curve corresponds to the symmetric particle-hole case, with $\epsilon_d = -U/2$, where ϵ_d is the energy of the impurity orbital and U represents the Coulomb repulsion. The dashed black curve represents the asymmetric case, with $\epsilon_d = -3\Delta$.

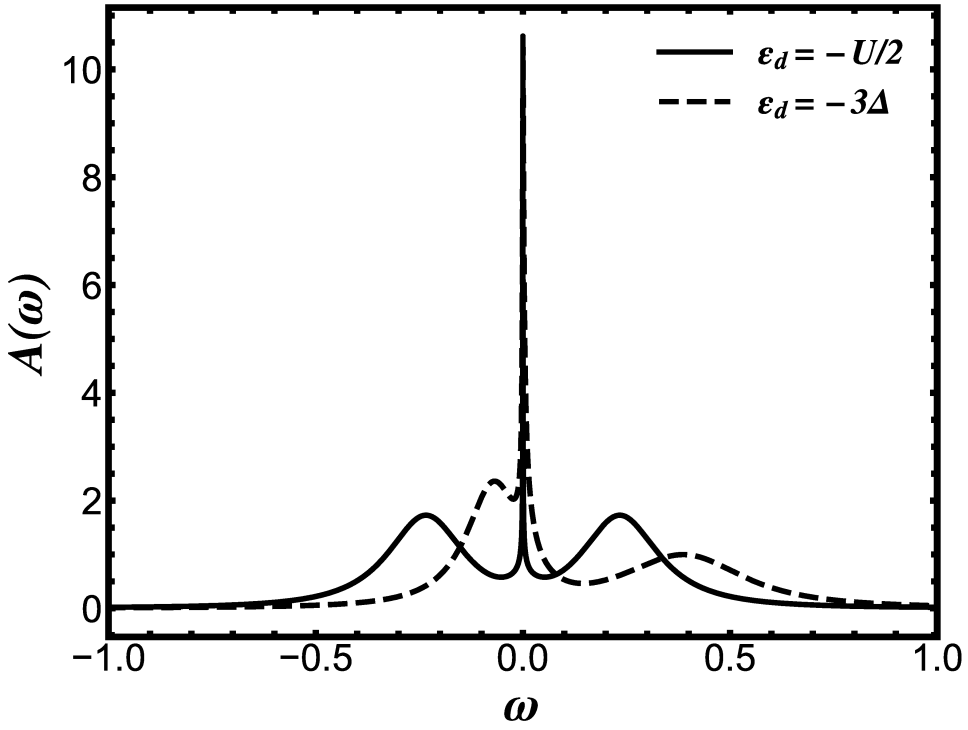

Figure 18 – Spectral function of a magnetic impurity. The solid black curve corresponds to the particle-hole symmetric case with $\epsilon_d = -U/2$, where ϵ_d is the impurity orbital energy and U is the Coulomb repulsion. The dashed black curve shows the asymmetric case with $\epsilon_d = -3\Delta$.

Chapter 4

Resonant Level

In this chapter, we investigate the behavior of a non-interacting Resonant Level (RL), generically referred to as an impurity, when placed near (or exactly at) the singularity $\omega^{-1/2}$ that naturally arises in a one-dimensional quantum wire. We demonstrate that the spectral function of the non-interacting RL, $\rho_{U=0}$, exhibits a bound state below the bottom of the density-of-state band ρ_{band}. This bound state possesses the properties of a Dirac delta function and carries a spectral weight determined by the coupling between the RL and the band, as well as by its distance from the singularity in ρ_{band}. Our analysis reveals two remarkable features of this non-interacting problem. First, a bound state emerges even when the RL is positioned near the band center, appearing at the band edge, but with negligible spectral weight even for moderate couplings. Second, when the RL is located exactly at the singularity, the bound state acquires a fixed spectral weight of 2/3, regardless of the coupling strength.

4.1 Spin-orbit coupling

When an electron with linear momentum $\vec{p}$ moves through a magnetic field $\vec{B}$, it experiences a Lorentz force perpendicular to its trajectory, given by $\vec{F} = -\frac{e}{m}\vec{p} \times \vec{B}$. Simultaneously, it acquires a Zeeman energy expressed as $\mu_B \vec{\sigma} \cdot \vec{B}$, where μ_B denotes the Bohr magneton and $\vec{\sigma}$ is the vector of Pauli spin matrices. Analogously, when traveling through an electric field $\vec{E}$, the electron perceives, in its rest frame, an effective magnetic field $\vec{B}_{\text{eff}} \sim \frac{\vec{E}\times\vec{p}}{mc^2}$, which leads to a momentum-dependent spin-orbit interaction energy (53).

Within the regime of weak relativistic effects, the Schrödinger-Pauli formalism is modified by incorporating Spin-Orbit Coupling (SOI). This interaction creates a connection between the electron's intrinsic spin $\vec{s}$ and its orbital angular momentum $\vec{l}$ in atomic systems (54). The SOI Hamiltonian is typically described by

$$H_{SO} = \frac{\hbar}{4m_0^2c^2}\,\boldsymbol{\sigma}\cdot[\nabla V(\mathbf{r})\times\mathbf{p}] \tag{74}$$

where $\hbar$ is the reduced Planck constant, m_0 is the mass of a free electron, c denotes the speed of light, $\mathbf{p}$ is the momentum operator, V refers to the Coulomb potential of the atomic nucleus, and $\boldsymbol{\sigma} = (\sigma_x, \sigma_y, \sigma_z)$ denotes the vector of Pauli matrices. In systems under the influence of electric fields generated by potentials that exhibit asymmetry under spatial inversion, spin degeneracy breaking can be observed. This phenomenon may occur even in the absence of an external magnetic field (Zeeman effect), as a direct consequence of SOI.

Within the framework of spin–orbit interaction, Time-Reversal Symmetry (TRS) is preserved. However, the presence of an electric field arising from an inversion-asymmetric potential breaks spatial inversion symmetry. In this scenario, we obtain

$$\begin{aligned} E(\mathbf{k},\uparrow) &= E(-\mathbf{k},\downarrow),\\ E(\mathbf{k},\downarrow) &= E(-\mathbf{k},\uparrow), \end{aligned} \tag{75}$$

reflecting the conservation of time-reversal symmetry. The SOI Hamiltonian can be represented as a sum of two distinct components, such that $H_{\mathrm{SOC}} = H_R + H_D$. Where, for a 2D-system (54), the terms are defined as:

$$\begin{cases} \text{Rashba:} \quad H_R = \alpha_R(k_y\sigma_x - k_x\sigma_y),\\ \text{Dresselhaus:} \quad H_D = \beta(k_x\sigma_x - k_y\sigma_y), \end{cases} \tag{76}$$

In these expressions, α_R and β denote the Rashba and Dresselhaus spin–orbit coupling constants, respectively. The variables k_x and k_y correspond to the components of the conduction electrons' wave vector along the x- and y-axes. The Rashba Hamiltonian is invariant under time reversal, as indicated by $\left[\hat{T}, H_{\mathrm{so}}\right] = 0$, where the time-reversal operator is given by $\hat{T} = i\sigma_y\hat{C}$, with $\hat{C}$ representing complex conjugation. Since lifting the degeneracy of electronic states at $k = 0$ requires the breaking of time-reversal symmetry, the Rashba term alone cannot induce spontaneous spin polarization. However it does lift the spin degeneracy when $k \neq 0$ (55). In crystalline systems lacking spatial inversion symmetry, the effective magnetic field arising from the Dresselhaus spin-orbit interaction originates exclusively from microscopic mechanisms. Within such frameworks, both the electric field vector $\vec{E}$ and the linear momentum vector $\vec{p}$ exhibit odd parity under the action of the parity symmetry operation.

4.2 Introduction to Quantum Wires

Quantum wires can be understood as physical realizations of Luttinger liquids because Fermi liquid theory fails in one dimension. Their design involves confining an electron gas within a narrow channel, where electronic transport occurs predominantly along a single direction. A representative example originates from a two-dimensional electron gas. The transition to a quasi-one-dimensional system can be achieved through lithographic techniques or by applying a repulsive potential from a gate, which effectively restricts the electrons to a single conducting channel. In Figure 19, we depict the energy dispersion of a system in which electrons are confined within a channel of width L_y.

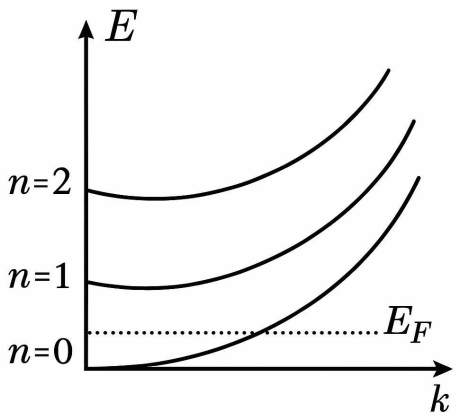

Figure 19 – The confinement of an electron gas within a one-dimensional wire is described, wherein only the positive branch of the dispersion relation $E(k)$ is considered. The vector k denotes the momentum component along the axis of the wire, while transverse quantization gives rise to discrete minibands characterized by the quantum number n. When the electronic confinement is sufficiently tight, the energy separation between these minibands exceeds the thermal energy scale, enabling occupation of a single miniband and consequently yielding one-dimensional

The system's wave function can be expressed as

$$\psi(x, y) = e^{ikx}\phi(y), \tag{77}$$

where $\phi(y)$ reflects the specific confinement potential profile (in the case of an infinite well, ϕ resembles a superposition of plane waves).

Assuming ϕ behaves as a plane wave for simplicity, the energy takes the form

$$E = \frac{k^2}{2m} + \frac{k_y^2}{2m}. \tag{78}$$

A key aspect here is that the narrow width l of the transverse channel causes significant quantization of k_y. Consequently, the energy spacing between transverse quantum states, such as from $n_y = 0$ to $n_y = 1$, is at minimum

$$\Delta E = \frac{(2\pi)^2}{2ml^2}. \tag{79}$$

As a consequence of transverse confinement, miniband structures emerge, as illustrated in Figure 19. When the energy separation between these bands surpasses the thermal energy scale, it becomes possible, through adjustment of the chemical potential via an external gate, to restrict electronic occupation to the lowest miniband. Under this condition, transverse states remain inactive, and only the longitudinal momentum k governs the system's behavior, which effectively corresponds to a one-dimensional electron gas. As an example, Figure 20 illustrates the formation of the electronic channel from a two-dimensional electron gas (2DEG), which is established at the interface between the GaAs semiconductor and the insulating AlGaAs layer (56).

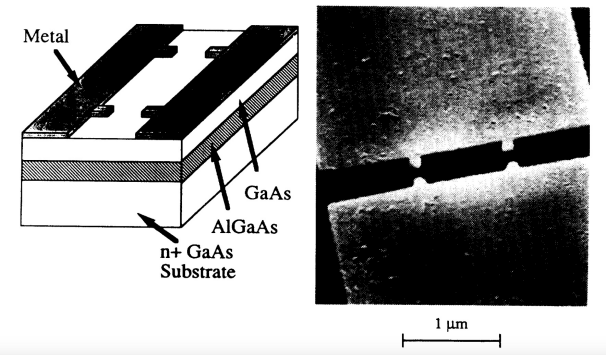

Figure 20 – A schematic representation of the device, along with a scanning electron micrograph, illustrates the electronic channel delineated at the GaAs–AlGaAs interface.

4.3 Noninteracting resonant level model

Here, the system under analysis will be characterized using the non-interacting Anderson model. This theoretical model describes a single fermionic energy level coupled by tunneling to a continuum of electronic states (57). The Hamiltonian of the model is expressed by:

$$H = \sum_{k,\sigma} \epsilon_k c^\dagger_{k,\sigma} c_{k,\sigma} + \epsilon_d \sum_{\sigma} d^\dagger_\sigma d_\sigma + \sum_{k,\sigma} V_k (d^\dagger_\sigma c_{k,\sigma} + \text{h.c}). \tag{80}$$

In this formulation, the creation operator $d_\sigma^\dagger$ corresponds to an impurity electron with spin σ. The term ϵ_d represents the energy of the impurity level. The parameter V_k is known as hybridization, and its function is to mediate the exchange of electrons between the impurity and the continuum of states. For simplicity, it is assumed that V_k is independent of the wave vector k and is therefore treated as a constant.

Additionally, Γ quantifies the coupling strength between the impurity and the electronic bath. Its definition is given by:

$$\Gamma = \pi V^2 \rho_{\text{band}}(E_F) \tag{81}$$

where $\rho_{\text{band}}(E_F)$ is the density of states (DOS) of the host material at the Fermi energy (E_F).

Next, we proceed to calculate the relevant quantities of the model. Neglecting spin degeneracy, our analysis focuses on the impurity spectral function. The spectral function, $A(\omega)$ as it extends the concept of the density of states by describing the distribution of electronic states as a function of energy. Specifically, for an impurity level, the local density of states (LDOS) is directly determined by the spectral function,

$$A_d(\omega) = \frac{1}{\pi} \frac{\Gamma}{(\omega - \epsilon_d)^2 + \Gamma^2}. \tag{82}$$

Figure 21 (a) illustrates the spectral function at the RL for different values of Γ. In this context, the impurity's density of states exhibits a Lorentzian profile. From a physical standpoint, it reflects the probability of detecting an excitation with energy ω. For a vanishing hybridization term, the spectral function at the impurity reduces to a Dirac delta function centered at $\omega = \epsilon_d$. Upon introducing hybridization, the delta peak broadens, acquiring a width proportional to Γ. The occupation number are expressed by:

$$n_{d,\sigma} = \frac{1}{2} - \frac{1}{\pi} \arctan\left(\frac{\epsilon_d}{\Gamma}\right) \tag{83}$$

The impurity level occupation, n_d, constitutes another fundamental observable that can be directly derived from the spectral function. This quantity expresses the average number of electrons localized at the impurity site. Under thermal equilibrium, the likelihood that a state of energy ω is occupied is governed by the Fermi–Dirac distribution, $f(\omega)$. Acting as a thermal filter, this distribution determines which electronic states, relative to the chemical potential μ and the temperature T, are effectively accessible. Consequently, the average occupation number is obtained through an integration of the

spectral function weighted by the Fermi–Dirac distribution over the entire energy spectrum. Figure 21(b) shows the occupation profile of the resonant level as a function of the impurity local energy.

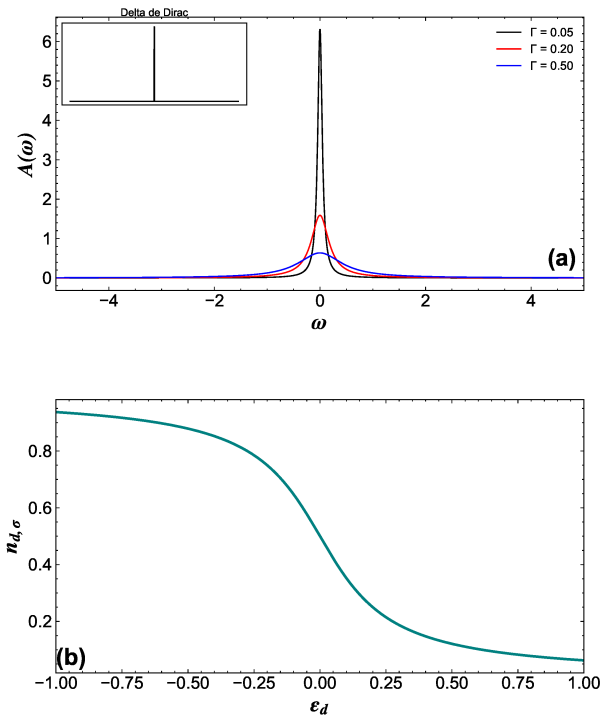

Figure 21 – (a) Shows the spectral function of the resonant model for different values of Γ. (b) Displays the electronic occupation as a function of the impurity level energy.

4.3.1 RL in a quantum wire

In this section, we discuss in detail what happens when a noninteracting RL is placed close (or at) the $\omega^{-1/2}$ singularity of the host. We wish to understand how the proximity of the RL to the singularity affects the RL spectral function. We note that Ref. (58) discusses a bound state out of the continuum in three dimensions (3D) in the presence of spin-orbit interaction SOI. By comparison, we now analyze the one-dimensional (1D) case, where the RL interacts with a quantum wire that also exhibits SOI.

The Hamiltonian governing the previously discussed system, consisting of a noninteracting impurity coupled to a nanowire, resembles the one presented in Eq. 80, with the only distinction that, in the present case, the host is described by

$$\mathcal{H}_{\text{wire}}(k) = (-2t\cos k - \mu)\sigma_0 + (\beta\sigma_x + \alpha\sigma_y)2\sin k, \tag{84}$$

where β and α are the Dresselhaus (59) and Rashba (60) spin-orbit interactions, respectively. σ_x and σ_y are spin Pauli matrices, and σ_0 is the 2×2 identity matrix. It can be

shown (61) that the energy dispersion associated with this Hamiltonian may be written as

$$\epsilon_{\kappa\sigma} = -2\sqrt{t^2 + |\gamma|^2}\cos(k - \sigma\varphi) - \mu, \tag{85}$$

where $\gamma = \beta + i\alpha$, $\varphi = \tan^{-1}(|\gamma|/t)$, and $\sigma = \pm$. The band structure and the density of states for this Hamiltonian are studied in the next section.

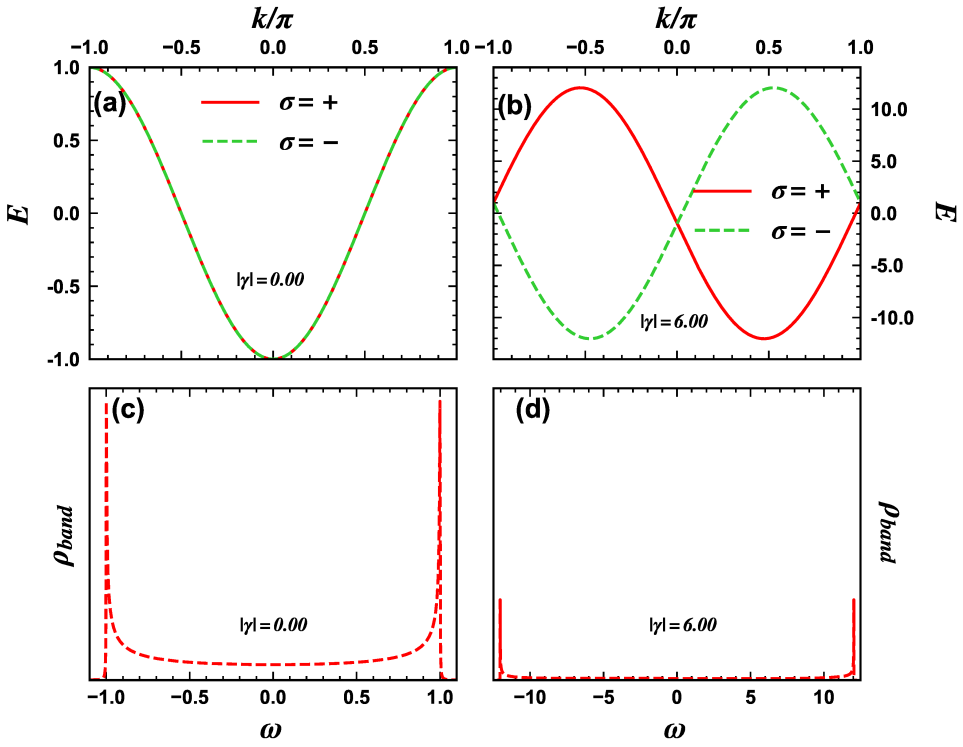

Figure 22 – Band structure for (a) $|\gamma| = 0.0$ and (b) $|\gamma| = 6.0$. Corresponding band density of states (DOS) for the same values of $|\gamma|$, in (c) and (d), respectively. Notice how the singularity for $|\gamma| = 6.0$ in (d) carries a considerably smaller spectral weight than the corresponding singularity for $|\gamma| = 0.0$ in (c). Note that the range in the vertical axes in (c) and (d) are the same, with the integral of ρ_{band} equal to 1 in both cases.

4.3.1.1 Band structure and spectral function in 1D with SOI

In this section, we show that the inclusion of SOI in 1D (which already has a singularity at the bottom of the band without SOI) decreases the spectral weight of the bound state. Figure 22 shows the band structure in panels (a) ($|\gamma| = 0.0$) and (b) ($|\gamma| = 6.0$), with the corresponding DOS in panels (c) ($|\gamma| = 0.0$) and (d) ($|\gamma| = 6.0$). It is clear that SOI decreases the spectral weight carried by the singularity at the bottom of the band. This happens because a finite SOI increases the bandwidth [compare the range in the horizontal axes in Figs. 22(c) and 22(d)].

We show next that this implies a loss of spectral weight of the bound state associated with the singularity. We calculate the RL Green's function $\hat{G}_{\rm imp}(\omega)$ (62), given by

$$\hat{G}_{\rm imp}(\omega) = \Big[(\omega - \epsilon_d)\sigma_0 - \hat{\Sigma}^{(0)}(\omega) + i\eta\Big]^{-1}, \tag{B1}$$

where $\hat{\Sigma}^{(0)}(\omega) = \sum_k \hat{V}\hat{G}_{\rm wire}(k,\omega)\hat{V}^\dagger$ is the hybridization self-energy, with $\hat{V} = V\sigma_0$, $\hat{G}_{\rm wire}(k,\omega) = [\omega\sigma_0 - \mathcal{H}_{\rm wire}(k)]^{-1}$ is the quantum wire Green's function. The RL spectral function, i.e., its DOS, is calculated through

$$\rho_U = -\frac{1}{\pi}{\rm Im}\ {\rm Tr}\hat{G}_{\rm imp}(\omega). \tag{86}$$

A comparison of both the 1D lattice DOS (blue curves) and the RL DOS (blue curves) is shown in Figure 23 for $|\gamma| = 0.0$ and $|\gamma| = 1.0$, panels (a) and (b), respectively, where we have set $\epsilon_d = \omega_{\rm sing} + \delta$ (with $\delta = 0.05$, and $\omega_{\rm sing}$ being the energy at the bottom of the band, with the band being symmetric around $\omega = 0.0$), and $V = 0.25$. A comparison of the RL DOS in both panels shows that a finite SOI decreases the spectral weight of the bound state. Thus, the area of the DOS inside the continuum in panel (b) is clearly larger than in panel (a). This is further detailed in what follows.

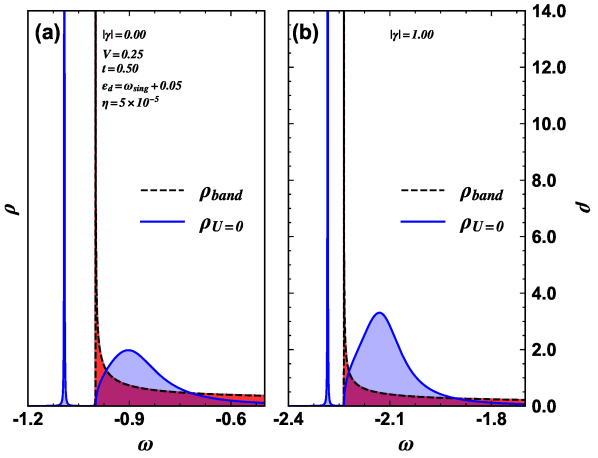

Figure 23 – Band density of states (DOS) $\rho_{\rm band}$ (red dashed curves) and the resonant level (RL) DOS $\rho_{U=0}$ (green curves) for (a) $|\gamma| = 0.0$ and (b) $|\gamma| = 1.0$. The RL orbital energy $\epsilon_d = \omega_{\rm sing} + \delta$ is placed at $\delta = 0.05$ above the bottom of the band $\omega_{\rm sing}$, in both cases. In (a), $Z_b = 0.554$, while in (b), $Z_b = 0.415$, showing that the increase of spin-orbit interaction (SOI) makes the bound state less bound and with a weaker spectral weight Z_b.

In Figure 24, we show results for Z_b, which is defined as

$$Z_b = \int_{-\infty}^{\omega_{\rm sing}} \rho_{U=0}(\omega)\, d\omega, \tag{87}$$

for the interval $0.0 \leq |\gamma| \leq 0.5$, where $\omega_{\rm sing}$ is the position of the singularity. It clearly shows that Z_b decreases monotonically with $|\gamma|$. This can be understood by analyzing the $\rho_{\rm band}$ results in Fig. 22, where we can easily see that, for $|\gamma| = 6.0$, there is considerably less spectral weight at the bottom of the band than for $|\gamma| = 0$. Indeed, integrating $\rho_{\rm band}$ from $\omega_{\rm sing}$ to $\omega_{\rm sing}+0.05$ yields approximately 0.09 for $|\gamma| = 0$ and 0.04 for $|\gamma| = 6.0$. Thus, one expects that the RL will be less affected by the singularity for finite SOI. Again, this occurs because a finite SOI increases the bandwidth.

We have established that the presence of SOI in 1D weakens both the band-edge singularity and the resulting bound state. This is in contrast to the 3D system in Ref. (58) that requires SOI to create a singular DOS. In what follows, we analyze the properties of the 1D system without SOI.

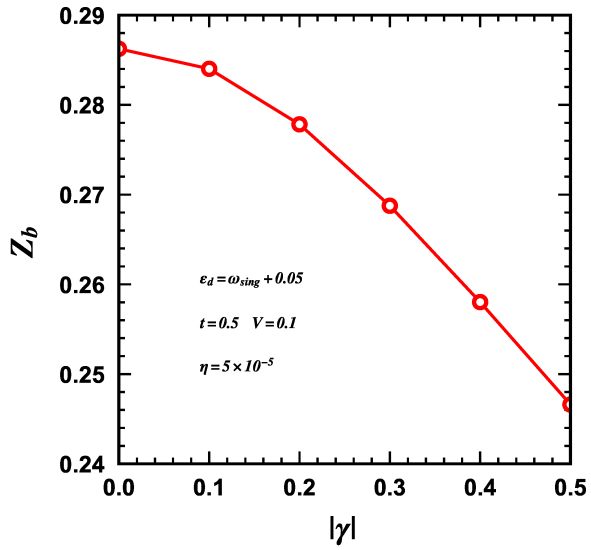

Figure 24 – Variation of the bound-state spectral weight Z_b with $|\gamma|$ for $V = 0.1$.

4.3.1.2 BOUND STATE PROPERTIES

Bound state and coupling to the band

First, we find that, no matter what the energy of the RL is in relation to the singularity, there is always a bound state located either at the singularity or below it. The latter occurs when the coupling of the RL to the band is strong or if the RL is close to the singularity. In Fig. 25, we show the RL density of states (DOS) $\rho_{U=0}$ for three different positions of the RL relative to the bottom of the band. In panel (a), the RL is located at the center of the band $\epsilon_d = 0$, and the singularity is at $\omega = -1.0$. We notice a vanishingly narrow DOS peak at the singularity. In panel (b), the RL is located at $\epsilon_d = -0.5$, midway between the

center of the band and the singularity. The DOS peak at the singularity has increased considerably. Finally, when the RL is just 0.2 above the singularity, $\epsilon_d = -0.8$, the bound-state spectral weight at the singularity has increased drastically. As ϵ_d approaches the bottom of the band, the spectral weight of the singularity increases significantly. Coupling strength is fixed at $V = 0.15$ in all panels. If the coupling increases and/or the RL approaches the singularity even more, the bound state detaches from the band continuum and moves to lower energies, as shown below.

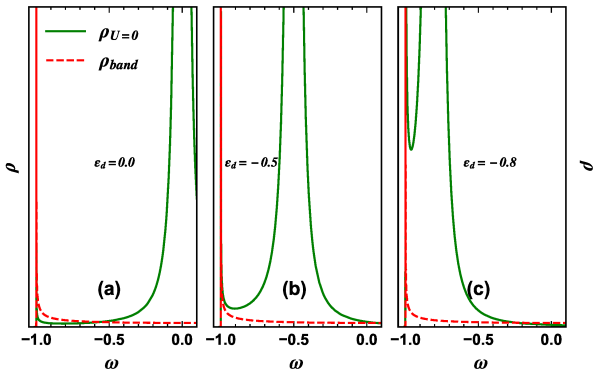

Figure 25 – Resonant level (RL) density of states (DOS) $\rho_{U=0}$ (green curve) for three different RL energies: (a) $\epsilon_d = 0.0$, (b) $\epsilon_d = -0.5$, and (c) $\epsilon_d = -0.8$. The red curve represents the band singularity.

Figure 26(a) presents the density of states (DOS) associated with the RL as its coupling to the conduction band, denoted by V, is varied over the range $(0.005 \leq V \leq 0.2)$. Throughout this analysis, the impurity energy is held constant at $\epsilon_d = \omega_{\text{sing}} + 0.05$, ensuring a fixed energetic offset from the band singularity. The plot reveals how the RL spectral features evolve in response to increasing hybridization. For the smallest value $V = 0.005$ (green curve), a bound state at the singularity is not visible, indicating vanishingly small spectral weight. For $V = 0.05$ (blue curve), a very sharp peak at the singularity is clearly observable, with spectral weight $Z_b = 0.044$. When $V = 0.1$ (cyan curve), the bound state detaches from the bottom of the band and shifts to lower energies, with its spectral weight increasing to $Z_b = 0.1566$. This trend persists as V increases. Figure 26(b) illustrates the growth of Z_b with increasing V, eventually reaching more than half of the total spectral weight at $V = 0.25$.

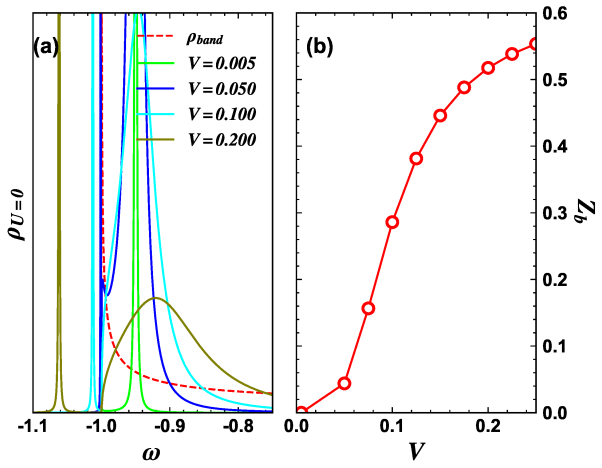

Figure 26 – (a) Variation of the resonant level (RL) density of states (DOS) $\rho_{U=0}$ with the coupling to the band in the interval $0.005 \leq V \leq 0.2$, for $|\gamma| = 0.0$ and $\delta = 0.05$. (b) The variation of Z_b for $0.01 \leq V \leq 0.25$.

Figure 27 shows the variation of the peaks associated with the impurity spectrum. The red curve highlights ω_{sing}, which represents the position of the band bottom—that is, the energy associated with the singularity. The green curve, ϵ_d, indicates the orbital energy position of the impurity. The blue curve, ϵ_d^r, shows the renormalized position of the resonant orbital level, while the cyan curve, ϵ_b, represents the position at which the bound state is formed. All these quantities are plotted as a function of V, and as V increases, the coupling between the impurity and the bath becomes stronger.

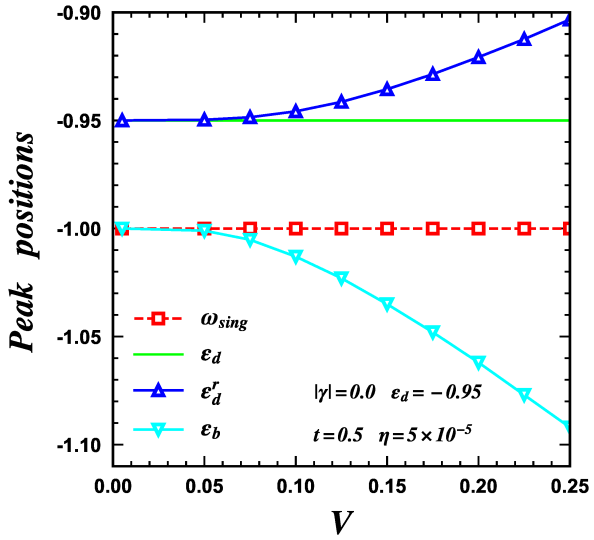

Figure 27 – Analysis of the formation of the bound state in the resonant level (RL) spectral function $\rho_{U=0}$ as a function of the coupling strength V, obtained from the results in Fig. 26(a). The red curve represents the bottom of the band (i.e., the position of the singularity); the green curve shows the position of ϵ_d, the RL orbital energy; the blue curve marks ϵ_r, the renormalized position of the RL level; and the cyan curve indicates the position of the bound state ϵ_b.

Bound state and distance to singularity

Now we analyze how the bound state varies as we move the RL ϵ_d closer to the singularity. We set $\epsilon_d = \omega_{\text{sing}} + \delta$, where ω_{sing} marks the bottom of the band. The results are shown in Figs. 28(a) and 28(b). The variation of $\rho_{U=0}$ as a function of δ, which represents the offset of ϵ_d from the bottom of the band, was carefully examined in two distinct intervals, revealing contrasting behaviors. In interval (a), covering values from $0.005 \leq \delta \leq 0.04$, the results show significant changes in both the renormalization factor Z_b and the positions of the peaks in the density of states. These changes become particularly notable when considering curves ranging from $\delta = 0.08$ (dark blue curve) to $\delta = 0.016$ (blue curve), indicating a strong sensitivity of the system to variations in δ within this regime. Conversely, in interval (b), which is narrower and spans $0.0005 \leq \delta \leq 0.004$, further approximating ϵ_d to the bottom of the band—especially for $\delta \leq 0.01$—does not result in substantial changes in the observed properties. This suggests that the effects of varying δ become gradually less relevant in this ultra-low range. It is worth emphasizing that all these results were obtained under specific conditions of hybrid coupling $V = 0.25$ and zero mixing interaction $|\gamma| = 0.0$, providing a clean framework to exclusively analyze the impact of δ displacement on $\rho_{U=0}$.

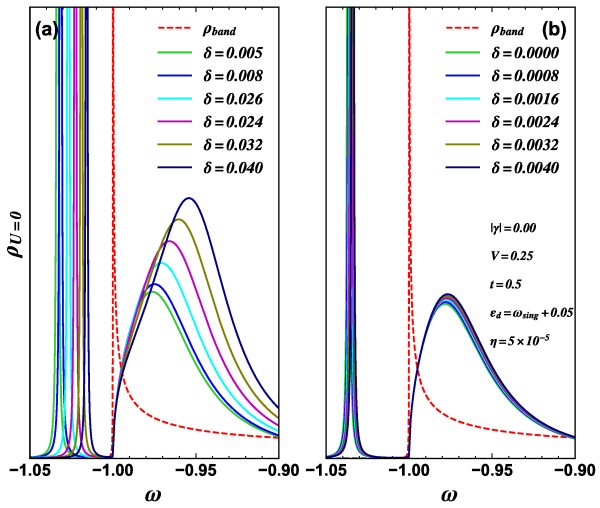

Figure 28 – Variation of $\rho_{U=0}$ with δ (ϵ_d offset from the bottom of the band) for two different intervals: (a) $0.005 \leq \delta \leq 0.04$ and (b) $0.0005 \leq \delta \leq 0.004$. (a) results show that, starting from $\delta = 0.08$ (dark blue curve), up to $\delta = 0.016$ (blue curve), changes in Z_b and peak positions are considerable, while (b) results show that further approaching ϵ_d from the bottom of the band ($\delta \leq 0.01$) has limited effects. Results obtained for $|\gamma| = 0.0$ and $V = 0.25$.

In Fig 29, we illustrate the variation of the impurity spectral weight Z_b as a function of δ, a parameter that quantifies the deviation of the impurity's orbital energy from the singularity at the bottom of the wire's conduction band. It is evident that as δ increases—that is, as the impurity moves energetically away from the singularity—the

spectral weight progressively decreases. The most intriguing aspect of this behavior occurs when $\delta = 0$, meaning the impurity is tuned precisely to the singular energy, and the spectral weight approaches a universal value of $Z_b = \frac{2}{3}$, suggesting the emergence of a regime with invariant characteristics. This shows the very interesting phenomenon that the $Z_b = \frac{2}{3}$ result does not depend on the details of the band, such as spatial dimensionality (3D vs 1D) and presence vs absence of SOI. The inset, with a log scale in the δ axis, emphasizes the gradual approach to the $Z_b = \frac{2}{3}$ value.

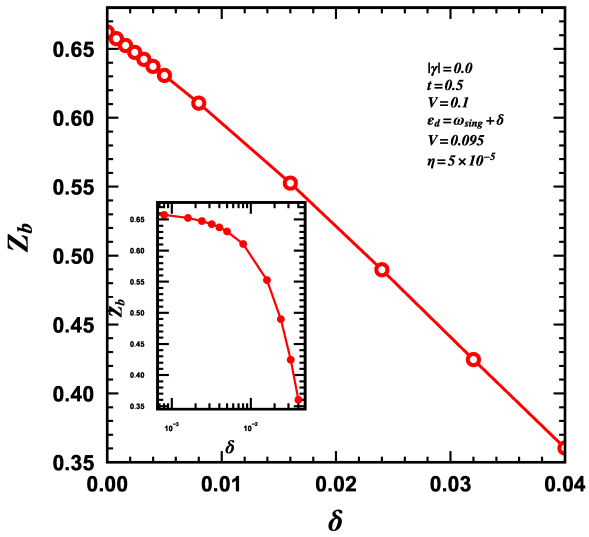

Figure 29 – Variation of the bound state spectral weight Z_b as a function of δ in the interval $0.001 \leq \delta \leq 0.08$. Results obtained from both panels in Fig. 28. The inset shows the same results but with a log scale in the δ axis, highlighting the approach to the $Z_b = \frac{2}{3}$ value.

Figure 30 illustrates the variation of peak positions as a function of the shift δ. The horizontal axis represents δ, while the vertical axis shows the corresponding peak positions. The four quantities analyzed are: ω_{sing} (red squares), ϵ_d (green circles), ϵ_r^d (blue triangles), and ϵ_b (cyan inverted triangles), allowing clear visualization of each variable's individual trends. Calculations were performed using the parameters: $|\gamma| = 0.0$, $V = 0.1$, $t = 0.5$, $\eta = 5 \times 10^{-5}$, and $\epsilon_d = \omega_{\text{sing}} + \delta$. The figure highlights how each component responds to changes in δ. ω_{sing} is held constant at -1 and $0.005 < \delta < 0.04$, with data extracted from Figure 28(a). Here, the green curve ϵ_d is positioned above the band bottom. This shows that the position associated with each curve does not display uniform behavior. As expected, ϵ_d grows almost linearly with δ (green curve). The blue curve, showing the evolution of the renormalized peak position, exhibits an increasingly smaller energy gap relative to ϵ_d, becoming less prominent. As the energy of the impurity orbital increases in relation to the singularity, ϵ_b, the position of the bound state, gets increasingly closer to the continuum.

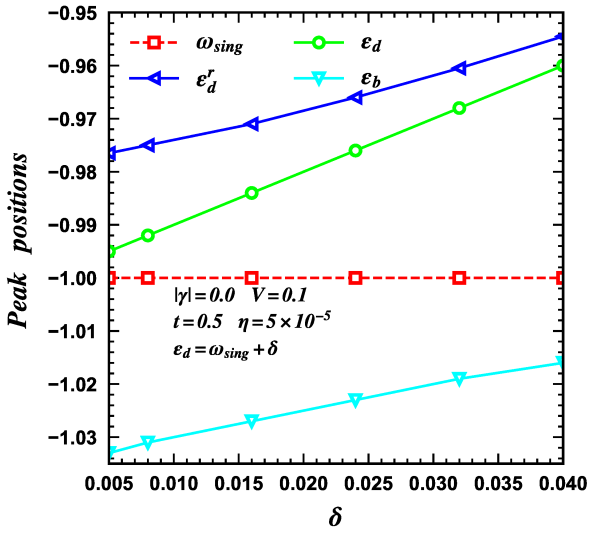

Figure 30 – Analysis of the formation of the bound state in the resonant level (RL) spectral function $\rho_{U=0}$ as a function of the parameter δ, obtained from the results shown in Fig. 28(a). The red curve represents the bottom of the band (i.e., the position of the singularity); the green curve shows the position of ϵ_d, which corresponds to the RL orbital energy; the blue curve marks ϵ_r, the renormalized position of the RL level; and the cyan curve indicates the position of the bound state ϵ_b.

Figure 31 examines the effects of a localized impurity with energy $\varepsilon_d = \omega_{\text{sing}} - \delta$, outside the continuum, on the electronic structure of a system, with $0.0 \leq \delta \leq 0.05$ and coupling $V = 0.1$. In panel (a), the variation of δ causes the peak in the density of states $\rho_{U=0}$ to split, indicating the emergence of bound states induced by the impurity. In panel (b), it is observed that the spectral weight Z_b of the bound state remains above 2/3 and increases with δ, highlighting the robustness and strengthening of the bound state with the impurity shift. Additionally, the density of states (DOS) within the continuum tends to accumulate at the band bottom as δ increases. Finally, Fig. 32 shows details of the results in Fig. 31(a).

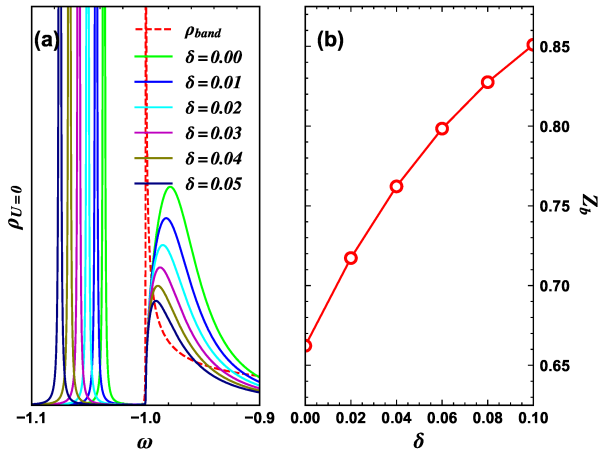

Figure 31 – Similar results as in Fig. 28 but now when the impurity is placed below the bottom of the band (note that $\epsilon_d = \omega_{sing} - \delta$) and $V = 0.1$. (a) Results for $\rho_{U=0}$, for $0.0 \leq \delta \leq 0.1$, showing again the peak splitting. (b) Spectral weight Z_b of the bound state, now $\geq \frac{2}{3}$

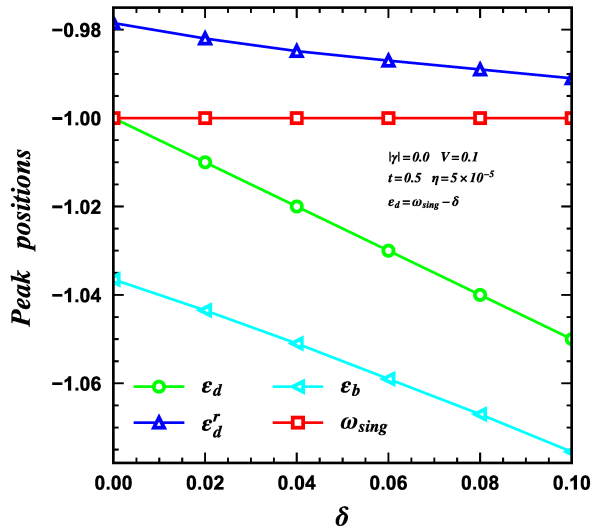

Figure 32 – Similar results as in Fig. 30, but now ε_d (green curve) is placed below the bottom of the band. Larger peak separations are obtained this way.

Chapter 5

Quantum wires with impurities: NRG approach

In this chapter, we investigate the Kondo state in a metallic system whose density of states exhibits a $\omega^{-1/2}$-type singularity, typical of the band bottom in one-dimensional chains. We model the interacting system using the SIAM, solved using the NRG method. The Hubbard interaction transforms the bound state, causing level splitting, spectral weight redistribution, spectral discontinuity, binding energy variation, and the emergence of a finite width. As ε_d approaches the singularity, the system partially recovers features of the Kondo regime, such as higher impurity occupancy and a lower T_K. Thermodynamic properties indicate that the local moment (LM) fixed point is also affected: near the singularity, it becomes resistant to charge fluctuations, unlike the behavior observed when ε_d is distant. Finally, we discuss a proposed experimental implementation using *armchair* graphene nanoribbons, which reproduce effects similar to those observed in quantum wires.

5.1 Introduction

The main properties of the Kondo state—the quenching of the impurity magnetic moment, universal temperature scaling, and existence of renormalization fixed points—are readily obtained when considering a featureless (flat) density of states (DOS) of the host around the Fermi energy (E_F), where most of the important physics occurs. This may be called a traditional Kondo effect. Things become more interesting, possibly including non-Fermi liquid physics (63), when the host DOS behaves like $\rho(\omega) = |\omega|^r$ at or near the Fermi energy. For $r > 0$, the DOS vanishes at $\omega = 0$, and the band is said to have a pseudogap. Many theoretical works have analyzed the Kondo model (no charge fluctuations) for bands presenting a pseudogap (64, 65, 66, 67, 52, 68, 69, 70, 71), while much less work has been devoted to the $r < 0$ case, i.e., when there is a divergent density of states (DOS) — a singularity — at the Fermi energy (63, 72, 73, 74), has been less

explored. Even fewer studies (75, 76, 77, 78, 79, 80) have investigated how a singularity near the E_F, which generates strong particle-hole (PH) asymmetry, affects the Kondo state. Recent work (58) has examined a Kondo state in which the impurity orbital level is resonant with a singularity at the bottom of the band — a scenario that arises in one-dimensional (1D) lattices, nanotubes (81), and nanoribbons (82) — while the Fermi energy lies slightly above the singularity, yielding intriguing results.

Here, we revisit a system similar to that studied in Ref. (58), employing NRG method. The NRG calculations were done using the NRG Ljubljana code (83). When the Hubbard interaction U is turned on, we find that the usual Kondo profile of the impurity spectral function [ρ_{NRG}] is modified. Indeed, the singularity strongly distorts the lower Coulomb blockade peak (CBP) of the impurity, which is now composed of a broadened bound state and a series of peaks. In addition, the T_K and the impurity occupancy are strongly affected when ε_d is close to the band singularity. Both quantities tend to values closer to those fully in the Kondo regime (higher occupancy and lower T_K) even when the system is in an intermediate valence regime. This reentrant Kondo regime can also be observed at temperatures around the LM fixed point. Indeed, the magnetic susceptibility in the intermediate valence regime takes values like those in the Kondo regime at temperatures associated with the LM fixed point. This behavior, also visible in the NRG energy flow, is clearly associated with the existence of the bound state. We present NRG results and analysis to explore these interesting regimes in detail below.

5.1.1 Singularity effect on the impurity spectral function and charge occupancy

As described in the literature (70, 71, 72, 73, 75), the Kondo state for Anderson-type systems (46) and highly asymmetric DOS (such as when the E_F is close to a Van Hove singularity) strongly depends on model parameters. Indeed, our detailed analysis of the Kondo state for E_F close to the 1D band singularity indicates that the impurity spectral function, impurity charge occupancy, and thermodynamic properties are very sensitive to the interplay between ϵ_d, U, V, and E_F. In other words, small changes in the parameters, like the position of E_F in relation to the singularity, strongly affect the Kondo state.

To reveal the most interesting aspects of the Kondo state when ϵ_d is at the singularity and E_F is close to the bottom of the band, we will contrast it to the Kondo state obtained when E_F is exactly in the middle of the band ($\mu = 0$), keeping all the other parameters equal. We take $\epsilon_d = -U/2$; thus, for $\mu = 0$, the system is in the PH-symmetric (PHS) point. These results are shown in Figure 33. Panels (a) and (b) show the impurity spectral function (green curve for the noninteracting case $\rho U = 0$ and blue curve for the interacting case ρ_{NRG}) for $\mu = 0$ and -0.995, respectively. The (red) dashed curves are the band DOS ρ_{band}. Note that all DOS results are normalized so that their integrals over

ω are 1. The parameters, kept fixed for both calculations, are $\epsilon_d = -0.005$, $U = 0.01$, and $\Gamma = 6.6667 \times 10^{-4}$ (thus $U/\Gamma = 15$). We have used V values for both calculations ($V = 0.026$ and 0.0082, for panels (a) and (b), respectively) such that Γ does not vary. The only change from one calculation to the other is the PH asymmetry around E_F: no asymmetry in panel (a) and very strong asymmetry in panel (b). Comparison of the ρ_{NRG} results (blue curves) in panels (a) and (b) shows how strongly the singularity affects the impurity spectral density. Indeed, from a traditional PHS Kondo peak at $\mu = 0$ [panel (a), blue curve], we move to a very rich impurity DOS when ϵ_d is at the singularity, showing a series of peaks around the Fermi energy ($E_F = 0.0$). The rightmost peak in ρ_{NRG} (the upper CBP), farthest from the singularity, is the least affected, while the Kondo peak (around $\omega = 0.0$) acquires slight asymmetry. Notice that the RL results (green curve, $\rho_{U=0}$) show that the singularity splits the noninteracting DOS into a Dirac δ-like bound state (below the bottom of the band) and a broad peak starting at the bottom of the band. As it turns out, this last peak becomes a superposition of three peaks in the continuum, while the bound state splits into two features below the band. One is very sharp, located at the band edge, and has very small spectral weight. The other, containing most of the spectral weight, is shifted to lower energy than the original bound state and acquires a sizable finite width. Thus, the interplay between the singularity and correlations results in very complex spectral behavior.

Figure 33(c) shows how the impurity occupancy $n_d = \langle n_{d\uparrow} + n_{d\downarrow} \rangle$ (for $U = 0.01$ and $U/\Gamma = 15$) varies when the Fermi energy moves from the center of the band ($\mu = 0$) to close to the bottom of the band ($\mu = -1.0 - \epsilon_d$), for different values of ϵ_d ($-0.005 \leq \epsilon_d \leq -0.0001$). Figure 33(d) shows a zoom of the results in panel (c) close to the lowest values of μ. Notice that the red-squares curve at the top for $\epsilon_d = -0.005$ is at the PHS point for $\mu = 0$, and the occupancy is pinned at $n_d = 1$ even as μ moves away from PHS. As expected, the average value of n_d decreases (from $n_d \approx 1.0$ to 0.45) as ϵ_d increases, from $\epsilon_d = -U/2 = -0.005$ (red squares) to very close to the Fermi energy $\epsilon_d = -0.0001$ (light green left triangles), moving the system from deep into the Kondo regime to an intermediate valence regime, even for $\mu = 0$. However, as the Fermi energy approaches the bottom of the band ($\mu \approx -1.0 - \epsilon_d$), n_d increases abruptly, with a faster rate the closer ϵ_d is to zero.

The variation of the bound state spectral weight Z_b [purple hexagons curve in Figure 33(c)] with μ, for the noninteracting case, indicates that once the system moves to the intermediate valence regime (larger values of ϵ_d), the presence of the bound state below the bottom of the band, with stronger spectral weight, strongly increases the charging of the impurity. This effect is negligible if the system is well into the Kondo regime ($\varepsilon_d = -0.005$, red squares) or close to it ($\varepsilon_d \lesssim -0.003$).

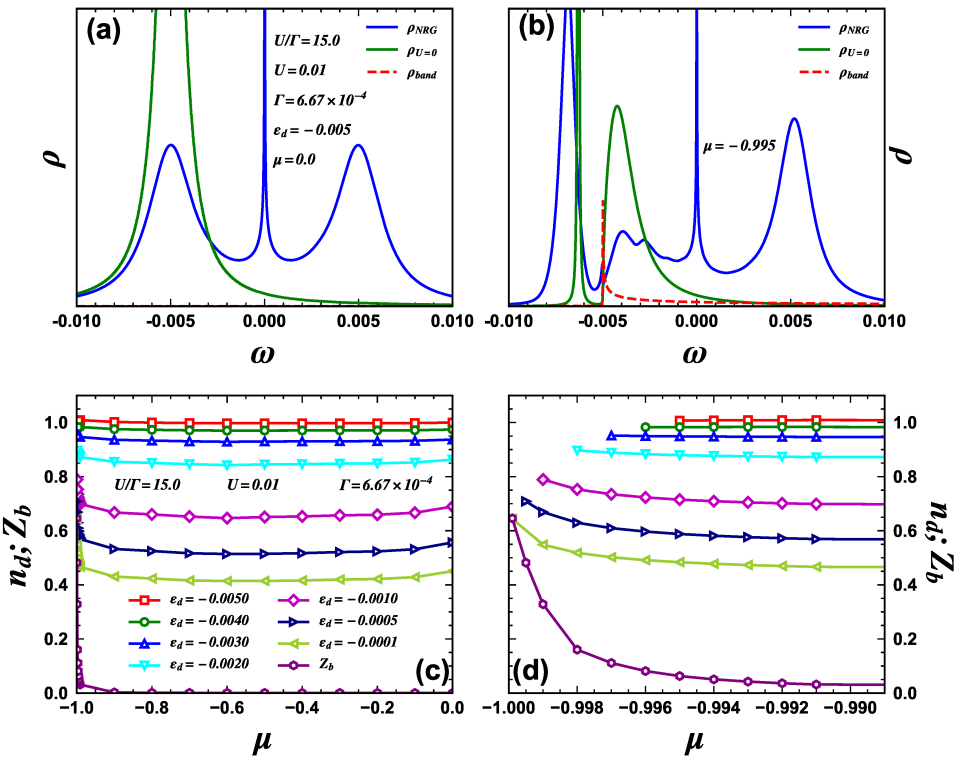

Figure 33 – Density of states (DOS) comparison and spectral weights for $U = 0$ and 0.01. (a) Impurity DOS for $U = 0$ ($\rho_{U=0}$, green curve) and for $U/\Gamma = 15$ (ρ_{NRG}, blue curve) for $\mu = 0$ (when E_F is at the center of the band, $\omega = 0.0$), $U = 0.01$ and $\epsilon_d = -U/2 = -0.005$ (notice dashed red curve close to the horizontal axis, showing the band DOS, ρ_{band}). (b) Same as in (a) but now with E_F very close to the singularity at the bottom of the band (depicted by the dashed red curve, ρ_{band}), $\mu = -0.995$, $\epsilon_d = -0.005$ (right at the singularity). In (a) and (b), the Γ value is the same for finite and vanishing U. (c) Finite $U = 0.01$ results for the evolution of $n_d = \langle n_{d\uparrow} + n_{d\downarrow} \rangle$ as E_F moves from the center of the band ($\mu = 0$, right side) to very near the singularity ($\mu = -1.0 - \epsilon_d$, left side), for different values of ϵ_d (the leftmost value of μ places the resonant level (RL) exactly at the singularity). The lowest (purple hexagons) curve with hexagons shows the bound state spectral weight Z_b (see the Appendixes), for $U = 0$ and $\epsilon_d = -0.0001$. (d) Zoom of the left side of (c) highlighting the abrupt increase in n_d. The lowest value of the chemical potential is $\mu = -1.0 - \epsilon_d$; thus, the curves above do not cover the same μ interval.

As n_d tends to approach its Kondo value of $n_d \approx 1.0$, despite ε_d approaching the intermediate valence regime, close to the bottom of the band, it is reasonable to expect that the T_K will be strongly affected. We expect T_K will tend to return to its Kondo value when we approach the bottom of the band in the intermediate valence regime. Indeed, this can be seen in Figure 34(a), showing a color map of the T_K for all the points in Figure 33(c). Focusing on the right side of the figure ($\mu = 0$, E_F at the center of the band), we see the usual increase in T_K as we move from top to bottom (from the Kondo to the intermediate valence regime). However, looking at the bottom of the figure, moving from right to left (from center to bottom of the band), we see that T_K decreases abruptly

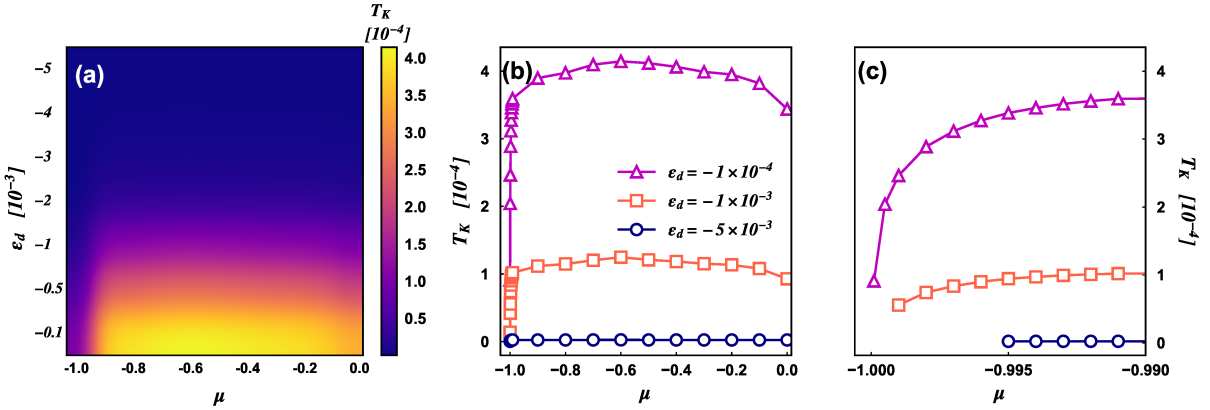

Figure 34 – (a) Color map of the T_K for all the points in Figure 33(c). The sudden drop of T_K at the bottom left corner indicates that the bound state near E_F moves the system back to the Kondo regime, which has a lower T_K than in the intermediate valence regime (bottom right corner). (b) Comparison of T_K vs μ results for $\epsilon_d = -1\times10^{-4}$ (magenta triangles, intermediate valence regime), $\epsilon_d = -1\times10^{-3}$ (orange squares, border between Kondo and intermediate valence regimes), and $\epsilon_d = -5\times10^{-3}$ (blue circles, deep into Kondo regime). (c) Zoom of the results in (b) close to the bottom of the band.

as we approach the bottom of the band, tending back to its low Kondo-regime value. Figure 34(b) shows a comparison of results for T_K vs μ for different $\varepsilon_d = -1\times10^{-4}$ (magenta triangles, intermediate valence regime), $\varepsilon_d = -1\times10^{-3}$ (orange squares, border between Kondo and intermediate valence regimes), and $\varepsilon_d = -5\times10^{-3}$ (blue circles, Kondo regime), highlighting the sharp drop in T_K as μ approaches the singularity, when the system is in the intermediate valence regime (magenta triangles) or in a region in between Kondo and intermediate valence (84) (orange squares). This contrasts the stable behavior of T_K when the system is deep into the Kondo regime (blue circles). Figure 34(c) shows a zoom of the results close to the singularity. Indeed, the formation of the bound state close to the Fermi energy seems to bring the system back to a Kondo regime.

5.1.2 Evolution of the bound state with correlations

With the objective of understanding the origin of the split peaks around the singularity visible in Figure 33(b), we present in Figure 35 the evolution of the interacting impurity spectral function as U decreases, keeping $\Gamma = 8.334\times10^{-4}$, $\epsilon_d = -U/2$, and varying μ so that, for all panels, ϵ_d is at the singularity ($\mu = -1-\epsilon_d$). Panels (a)-(f) show results for $U/\Gamma = 12.0$, 9.0, 6.0, 3.0, 0.5, and 0.001, respectively (as indicated in each panel). With decreasing U, the upper CBP moves to lower energy, eventually merging with a considerably broader Kondo peak [panel (c)], resulting from the system having entered an intermediate valence regime. We now focus our attention on the two peaks below the bottom of the band, whose position and spectral weight can be followed more accurately [peaks P_0 and P_1]. For decreasing U/Γ, the leftmost peak P_0 transfers its spectral weight

to peak P_1, located at the bottom of the band. Indeed, for $U/\Gamma \lesssim 0.5$ [panel (e)], P_0 has transferred almost all of its spectral weight to P_1, while in the interval $3 \lesssim U/\Gamma \lesssim 6$, peak P_0 splits into two peaks. For $U/\Gamma \approx 9.0$, P_1 detaches from the bottom of the band, moving away from it for smaller U, while its spectral weight increases at the expense of P_0. Panel (f), for $U/\Gamma = 0.001$, has a comparison of the NRG (blue curve) and U = 0 results (dashed green curve), showing that they are virtually the same. This demonstrates that the NRG spectral function results reproduce faithfully the evolution of the many-body processes that give origin to the split peaks around the singularity, deep into the Kondo regime [panel (a), $U/\Gamma = 12$].

We now analyze ρ_{NRG} in more detail in panels (a) and (b), where we still have strong correlations. In both panels, a well-formed Kondo peak and an upper CBP are clearly visible. For $U/\Gamma = 9$, at energies below the Kondo peak (but still inside the continuum), a structure with two features is clearly visible. For $U/\Gamma = 12$, the Kondo peak and the upper CBP are clearly consolidated, and further structure (a third smooth feature) emerges between the Kondo peak and the bottom of the band.

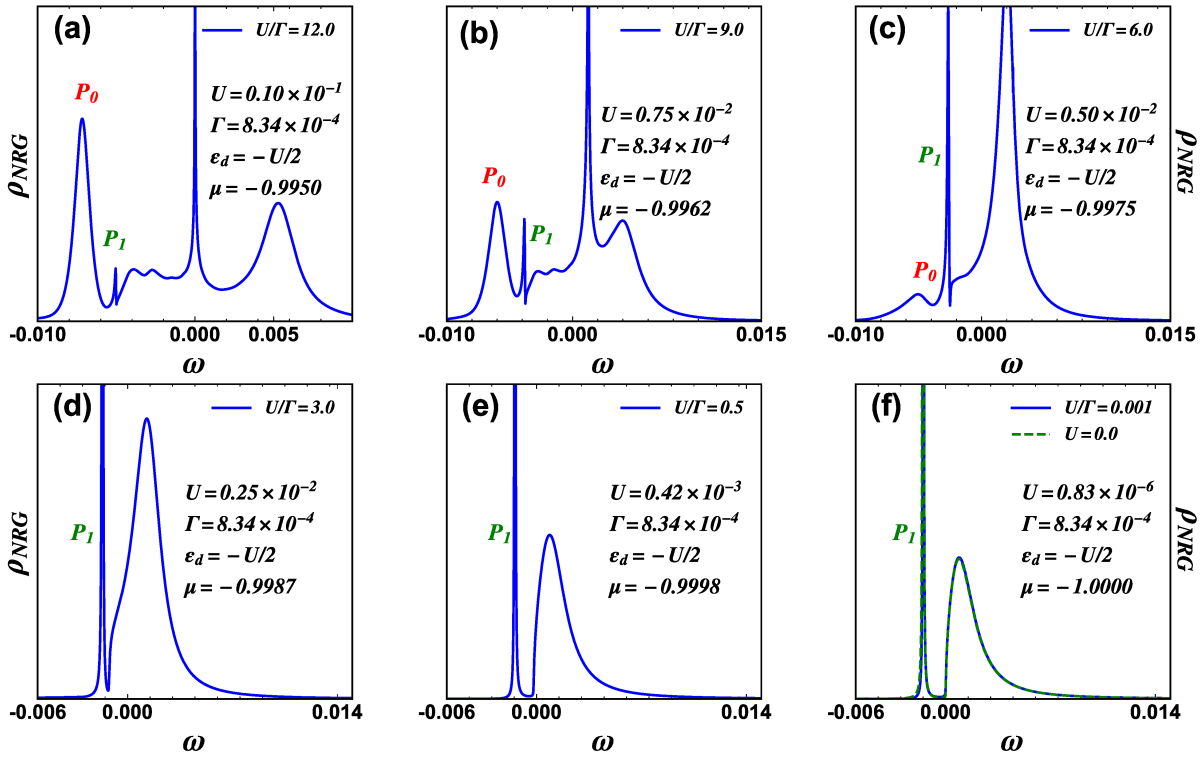

Figure 35 – Evolution of the interacting impurity spectral density $\rho_{\rm NRG}$ (blue curves), for $\Gamma = 8.34 \times 10^{-4}$, $\epsilon_d = -U/2$, and $\mu = -1.0 - \epsilon_d$, as U varies from (a) $U/\Gamma = 12$ to (f) 0.001. The value of μ places ϵ_d at the singularity in all panels. The dashed green curve in (f) is the noninteracting $\rho_{U=0}$ spectral function, showing excellent agreement with the $U \approx 0$ numerical renormalization group (NRG) result. The peaks P_0 and P_1 are associated with the bound state seen in $\rho_{U=0}$.

Figure 36 presents the spectral weight [panel (a)] and position [panel (b)], in relation

to the bottom of the band, of peaks P_0 and P_1 for different values in the interval $0.001 \leq \frac{U}{\Gamma} \leq 12.0$. In panel (b), we also plot the position of the noninteracting bound state (blue circles), for $U = 0$ and the same ϵ_d and V values used in the NRG calculations (note that the noninteracting results depend on $-\epsilon_d/\Gamma$, which labels the upper horizontal axes in panel (b) and its inset). Following the spectral weight curves for peaks P_0 (green squares) and P_1 (red right triangles), in Figure 36(a), we see that, when $\frac{U}{\Gamma}$ decreases from 12 to 0.5, the spectral weight of P_0 is almost all transferred to P_1 (although part of the spectral weight of P_0 is also transferred to the continuum and then, with further decrease of $\frac{U}{\Gamma}$, to peak P_1). In the interval $0.5 \geq \frac{U}{\Gamma} \geq 0.001$, P_1 quickly acquires spectral weight from inside the continuum, reaching $\approx \frac{2}{3}$ for very small values of $\frac{U}{\Gamma}$, as expected. The inset in Figure 36(a) shows the spectral weight of P_1 in a log scale to emphasize the formation of a $\frac{2}{3}$ plateau as $U \to 0$.

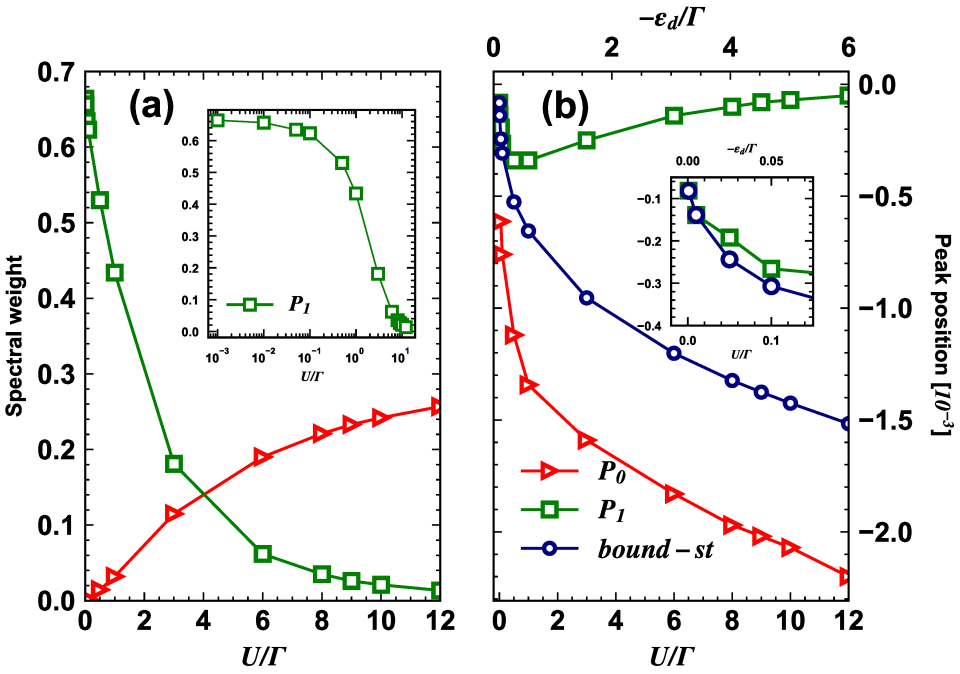

Figure 36 – (a) Spectral weight, as a function of U/Γ, for peak P_0 (red right triangles) and peak P_1 (green squares), as defined in the discussion of Figure 35. The inset shows P_1 spectral weight in a log scale, highlighting the $\frac{2}{3}$ plateau for vanishing U. (b) Energy position, in relation to the bottom of the band, of P_0 (red right triangles), P_1 (green squares), and the noninteracting bound state (blue circles). The inset shows the exact agreement between P_1 and the bound-state positions for the smallest values of U. Note that the noninteracting ($U = 0$) bound-state results (blue circles) are dependent on $-\epsilon_d/\Gamma$ (upper horizontal axes in the main panel and its inset), with $\epsilon_d = -U/2$, where the U and V values are defined by the NRG results.

Figure 36(b) shows the evolution of the position of P_0 (red right triangle) and P_1 (green squares), measured in relation to the bottom of the band. Their variation in position is contrasted to that of the noninteracting bound state (blue circles). Starting

from $\frac{U}{\Gamma} = 12$, P_1 (green squares) moves away from the bottom of the band as $\frac{U}{\Gamma}$ decreases, until, at $\frac{U}{\Gamma} \approx 1$, it reverses course and starts to approach the bottom of the band again. The position of P_1, the dominant peak for small values of U, progressively approaches the position of the bound state, until they coincide for the two smallest values of U, as emphasized in the inset. Peak P_0, on the other hand, monotonically approaches the bottom of the band as $\frac{U}{\Gamma}$ decreases, initially linearly, but then, around the same region where P_1 reverses course, starts to show a faster rate of approach to the bottom of the band as a function of $\frac{U}{\Gamma}$. Note that, to simplify the presentation, even after P_0 split into two peaks, we are considering it a single peak and taking a point halfway between the split peaks as the position of P_0.

Finally, the results for the position of P_1 [red right triangles in panel (b)] can be interpreted in the following way. As U decreases at fixed Γ, the Fermi energy approaches the bottom of the band since $\epsilon_d = -U/2$ is at the singularity. Since the Kondo peak becomes broader (as U/Γ decreases), P_1 is initially slowly forced away from the bottom of the band. However, for very small U values $U/\Gamma \lesssim 1$, the Fermi energy gets very close to the singularity, and since $\Gamma = \pi\rho_0 V^2$ is fixed, V decreases (since ρ_0 increases), and P_1, which has become the bound state (check comparison with blue circles curve in the inset), approaches the bottom of the band again (check also ϵ_b in Fig. 15).

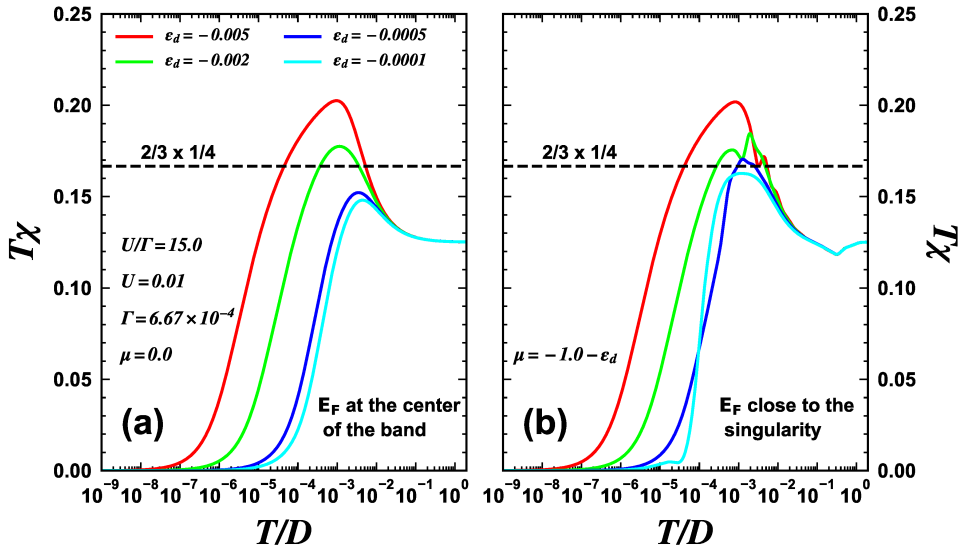

Figure 37 – Impurity magnetic susceptibility χ (as a function of temperature, in units of D, half bandwidth), for some of the ϵ_d values in Figure 33(d). (a) The Fermi energy is fixed at the center of the band and, as ϵ_d gradually increases, the system moves into the intermediate valence regime. Note that, for $\epsilon_d = -0.005$, the system is in the particle-hole-symmetric PHS point. (b) Same as in (a) but now the chemical potential is such that ϵ_d remains fixed at the singularity, and it is the Fermi energy that moves closer to the bottom of the band; thus, $\mu = -1.0 - \epsilon_d$. The values of Γ and U are the same as in Figure 33 for all calculations.

5.1.3 Thermodynamic properties: Fractional LM

Figure 37 shows the impurity magnetic susceptibility for four values of ϵ_d (-0.005, -0.002, -0.0005, and -0.0001). In panel (a), the Fermi energy is fixed at the center of the band ($\mu = 0$), and the system stays in a more standard Kondo regime. In contrast, in panel (b), $\mu = -1.0 - \epsilon_d$, E_F is located close to the bottom of the band, such that ϵ_d is at the singularity for all cases. Starting at the PHS point $\epsilon_d = -0.005$ [red curve, panel (a)], the system progressively moves into the intermediate valence regime as ϵ_d increases (ϵ_d approaches the Fermi level). As expected, the broad peak around $T \approx 0.001 \ll U = 0.01$, seen in the red curve, is indicative of the LM fixed point. As ϵ_d moves closer to the Fermi energy, charge fluctuations become more prominent, suppressing the formation of a LM at the impurity (cyan curve). On panel (b), however, where ϵ_d is at the singularity, and the Fermi energy progressively approaches it, the picture that emerges is substantially different. Although there is little difference between both panels for $\epsilon_d = -0.005$ (red curves), once the Fermi energy approaches ϵ_d, the suppression of the LM peak seems to be arrested in panel (b). The LM peak in χ stays pinned close to the $\frac{2}{3} \times \frac{1}{4}$ value, indicative of the presence of the bound state with spectral weight $Z_b = \frac{2}{3}$, even as ϵ_d changes by an order of magnitude.

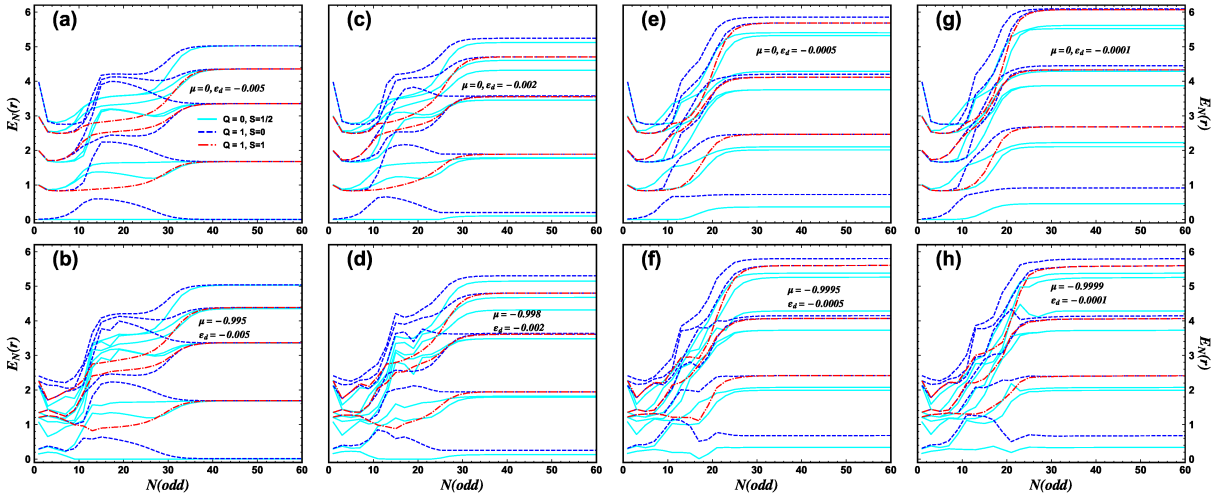

Figure 38 – Numerical renormalization group energy flow for odd N for the same parameters as in Figure 37. The ϵ_d values, from left to right, are -0.005, -0.002, -0.0005, and -0.0001. The top panels correspond to the Fermi energy at the center of the band, while the lower panels correspond to a Fermi energy close to the bottom of the band (ϵ_d at the singularity). Q is the charge in the system, measured in relation to half-filling, while S indicates the total spin (see Ref. (11) for details). The parameter values for U and Γ are the same as in Figure 37. For these NRG calculations specifically, $\Lambda = 2.5$.

The behavior of χ shown in Figure 37(b) suggests that the existence of the bound state makes the LM impervious to charge fluctuations. This is corroborated by the NRG energy flows, as shown in Figure 38, for the same parameters as in Figure 37. It is

well known that the three SIAM fixed points are associated with energy plateaus in the spectra as the number of NRG iterations varies. The free-orbital, LM, and strong-coupling fixed points are successively approached as N increases (which corresponds to a decrease in temperature or energy scale behavior). This can be easily spotted in Figure 38(a), corresponding to the PHS point, see Refs. (10, 11) for comparison. In the upper-row panels (Fermi energy at the center of the band, $\mu = 0$), we see that the plateaus starting at approximately $N = 10$ [Figure 38(b)] are gradually erased as charge fluctuations increase [panels (c), (e), and (g)]. For example, in Figure 38(g), the lowest energy state with $Q = 1$ and $S = 0$ (dashed blue curve) transitions directly (around $N = 10$) from a high- to a low-temperature value without going through an intermediate stage. This does not happen for the lower-row panels (E_F close to the bottom of the band). The plateau present in Figure 38(b) (between $N = 10$ and 30) is still present in panel (h) (although it now finishes at around $N = 20$). This is consistent with the results for a robust Kondo state seen in the impurity magnetic susceptibility in Figure 37.

For completeness, Figure 39 shows the impurity entropy as a function of $\frac{T}{D}$, for the same parameters as in Fig. 37. We note in panel (a) (E_F at the center of the band), for $\epsilon_d = -0.005$ (red curve), the usual evolution. As temperature decreases, the impurity entropy goes from the free-orbital (ln 4) plateau to the LM (ln 2) plateau, until it reaches the strong-coupling (ln 1) Kondo limit. Panel (b) shows the corresponding results when the Fermi energy is close to the bottom of the band, with ε_d at the singularity, as in Fig. 37. We notice again a pinning tendency around the LM plateau as ε_d increases, especially for $\varepsilon_d = -0.002$ (green curve), whose oscillation, also observed in the corresponding result in Figure 6, may be ascribed to the many-body states that appear between the Kondo peak and the singularity [see Figure 33(b)]. It is important to note the nonuniversal low-temperature behavior of the cyan curve in panel (b), which shows the impurity entropy being negative in the range $10^{-5} \lesssim T/D \lesssim 10^{-4}$. This behavior (which accompanies the nonmonotonic behavior of the cyan curve in T_χ, Figure 37) is reminiscent of the behavior seen in other Kondo problems in the presence of a sharp singularity or discontinuity in the DOS (75, 76, 85) and is clearly most prominent here when the RL is closest to the band singularity.

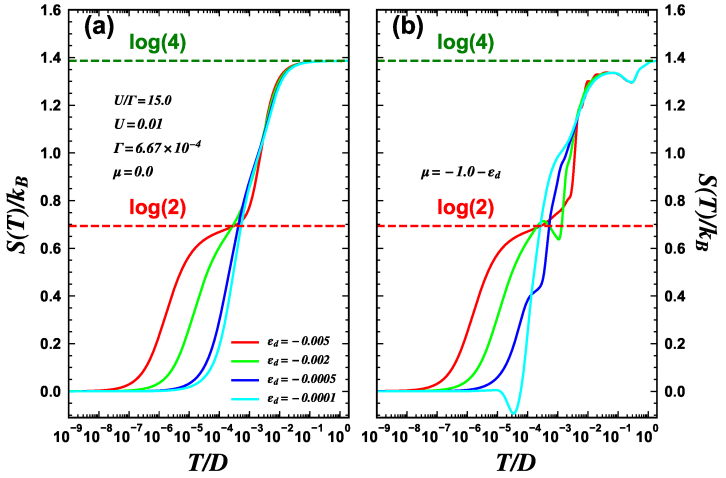

Figure 39 – Impurity entropy (as a function of temperature) for the same parameters as in Figure 37.

5.1.4 Results for an AGNR

We now discuss a possible physical implementation of the model NRG results presented in the previous sections. We study the Kondo states associated with band-edge singularities present in the DOS of an AGNR made by three carbon rows (3-AGNR), which is known to be a semiconductor (86, 87). Such nanoribbons can be fabricated from molecular precursors (88), for example, and have been used to study Kondo resonances in experiments (89). One interesting recent study is that of subgap states in the Kondo regime (90). Figure 40(a) shows the DOS of an undoped 3-AGNR with symmetric valence and conduction bands. The Fermi energy can, in principle, be gated down until it is close to the bottom singularity of the valence band (leftmost vertical dashed line), or we may gate-dope it with slightly more electrons and bring the Fermi energy just above the bottom singularity of the conduction band (rightmost vertical dashed line). Both cases reproduce the situation studied in the previous sections for the quantum wire. Figure 40(b) compares the ω dependence of these two singularities with that of the quantum wire, showing that they are virtually the same. Notice that panel (b) shows the hybridization function $\Delta(\omega) = \pi V^2 \rho(\omega)$ is the same for all three cases. These results in Figure 40(b) imply that the NRG results for the 3-AGNR and the quantum wire should be very similar. Indeed, the finite-U impurity spectral function [same parameters as in Figure 33(b)], shown in Figure 40(c), for the conduction band singularity, is quantitatively similar to the quantum wire results in Figure 33(b). The same occurs for the valence band singularity [Figure 40(d)].

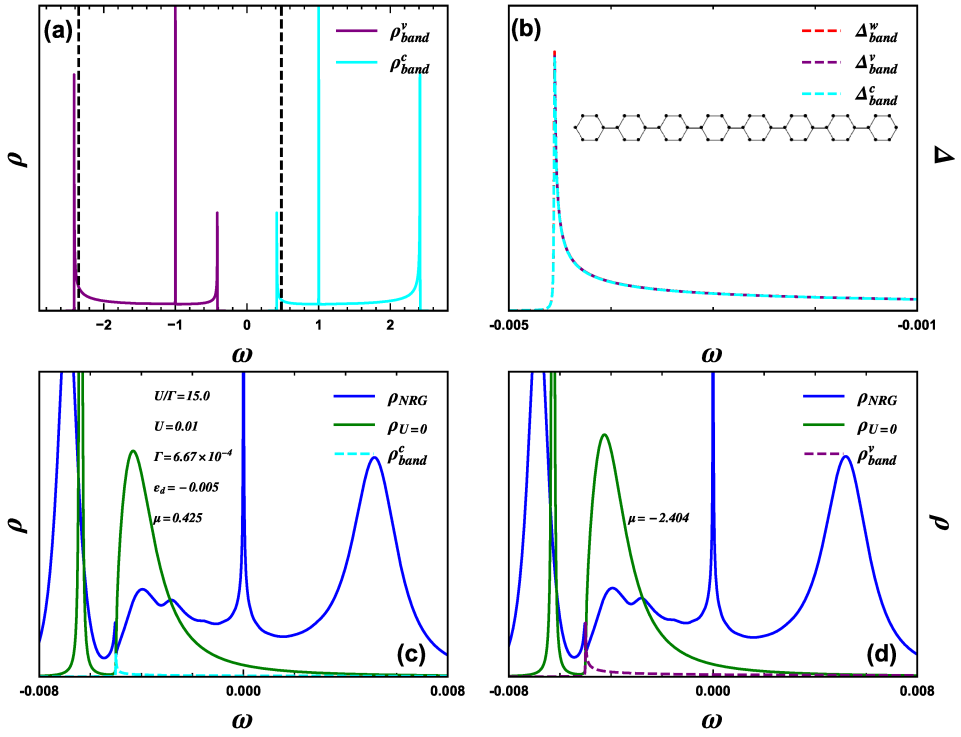

Figure 40 – (a) Armchair graphene nanoribbon made by three carbon rows (3-AGNR) density of states (DOS), showing the very symmetric valence (purple curve) and conduction (cyan) bands. The vertical black dashed lines indicate the approximate position of the Fermi energy for the calculations in (c) and (d). (b) Comparison of the quantum wire singularity ($\Delta^w_{\rm band}$, dashed red curve) with the 3-AGNR valence ($\Delta^v_{\rm band}$, dashed purple) and conduction ($\Delta^c_{\rm band}$, dashed cyan) hybridization functions lower singularities, showing they are identical. The inset shows a sketch of the 3-AGNR system. (c) Impurity DOS (blue curve, $\rho_{\rm NRG}$) when ϵ_d is at the singularity at the bottom of the conduction band. The result is very similar to Figure 33(b), for the quantum wire singularity. (d) Same as in (c) but now ϵ_d is at the valence band singularity. Also like (c). Parameter values (except for μ) are as in Figure 33(b).

5.1.5 Summary

We have analyzed the effect of Van Hove singularities near the Fermi energy and a magnetic impurity on the Kondo effect. Such singularities are present at the band edges of a quantum wire and of different AGNRs. The singularities present at the bottom of the valence and conduction bands of a 3-AGNR result in effective hybridization functions (at fixed Γ) with an $\omega^{-1/2}$ dependence. Thus, the spectral functions of the magnetic impurity are quantitatively similar to those obtained for a quantum wire and provide a convenient physical implementation of our model calculations (88, 89, 91). The main results we obtained are as follows. For a noninteracting impurity, we have characterized a Dirac δ bound state below the band minimum, with properties that depend on the near resonance of ϵ_d with the singularity, and on the coupling of the impurity to the band. As expected, the larger the coupling and the closer ϵ_d is to the singularity, the larger the spectral weight

Z_b of the bound state and the farther it is below the band minimum. The spectral weight Z_b is vanishingly small if ϵ_d is not close to the singularity, while it quickly increases as it approaches, reaching the value $Z_b = \frac{2}{3}$ at resonance, in agreement with previous work (58), where the singularity is due to SOI. In addition, the impurity level ϵ_d is slightly renormalized upward due to its interaction with the singularity. Once the Hubbard U is present, we see several interesting effects. First, starting with the Fermi energy at the PHS point in the middle of the band [Figure 33(a)] and then moving to the bottom of the band [Figure 33(b)], at fixed U and Γ, we see that the noninteracting bound state acquires a finite width and moves further away from the bottom of the band; in addition, a discontinuity appears in the impurity DOS at the band edge. Additional structure in the spectral function appears between this discontinuity and the Kondo peak which, aside from acquiring some asymmetry, is barely affected. An analysis of the evolution of the impurity DOS as U decreases, at fixed Γ, from $U/\Gamma = 12$ to occupancy of the impurity and its T_K value, show that the system partially recovers its strong coupling regime properties, i.e., higher occupancy and lower T_K, once the presence of the singularity is felt at the intermediate valence regime. This occurs because of the formation of the bound state.

In addition, the magnetic susceptibility shows that, for Fermi energy near the bottom of the band and in the intermediate valence regime, the LM fixed point is more resilient, as the impurity suppresses charge fluctuations. Figure 37(b) shows that the LM plateau is somewhat restored around the $\frac{2}{3} \times \frac{1}{4}$ value, indicating the influence of the bound state. This evolution is corroborated by an analysis of the NRG energy flow, shown in Figure 38, as well as the impurity entropy (Figure 39).

Chapter 6

Modeling the Two-Stage Kondo Regime via NRG

In this chapter, we investigate the behavior of a composite impurity in a metal, which can explore different configurations where its net magnetic moment may be screened by the electrons of the host. A particularly interesting case is the two-stage Kondo (TSK) system, in which the screening process occurs successively at distinct, progressively smaller energy scales. In contrast, the impurities may prefer a local singlet disconnected from the metal. This competition is decided by fine-tuning of the couplings in the system, as has been studied before. A double quantum dot T-shape geometry, where a 'hanging' dot is connected to current leads only via another dot, represents a flexible system in which these different regimes can be explored experimentally. It has been difficult, however, to clearly differentiate the two regimes. Here, we provide a prescription to better identify the regime where the TSK occurs in such double dot geometry. The TSK regime requires a balance of the ratio $\frac{t_{01}}{\Gamma_0}$ between the inter-dot coupling (t_{01}) and the coupling of the QD connected to the Fermi sea (Γ_0). Above a certain value of this ratio, the system crosses over to a molecular regime, where the quantum dots form a local singlet, and no Kondo screening occurs. Here, we establish that there is a region in the $t_{01}-\Gamma_0$ parameter space where a pure TSK regime occurs, i.e., where the properties of the second Kondo stage can be accurately described by a single impurity Anderson model with effective/renormalized parameters. By examining the magnetic susceptibility of the hanging QD, we show that a single parameter, Γ_{eff}, can accurately simulate this susceptibility. This effective model also provides the hanging QD spectral function with great accuracy in a limited range of the $t_{01}-\Gamma_0$ parameter space, thus defining the region where a true TSK regime occurs. We also show that in this parameter range, the spin correlations between both quantum dots show a universal behavior. Our results may guide experimental groups to choose parameter values that will place the system either in the TSK regime or in the crossover to the molecular regime.

6.1 Introduction

Point defects in semiconductors—in the form of vacancies, for example—may greatly affect the electrical conductivity of a host crystal (92). Similarly, magnetic impurities can qualitatively alter the electrical conductivity of their metallic hosts at low temperatures (19). A vacancy in a semiconductor, being a single-electron problem, does not lead to qualitatively different properties when a few more vacancies are added. In contrast, two magnetic impurities in a metallic host may interact with each other, even indirectly, leading to a completely different ground-state, depending on the ratio of the relevant parameters (93, 94). The phenomenology of the so-called two-impurity Anderson model (95) lies at the heart of the current understanding of important classes of compounds, such as heavy-fermions (96) and Kondo insulators (97).

Research on single-impurity systems received a large boost at the closing of last century with the observation of the Kondo effect in QDs (98) and magnetic impurities on metal surfaces (99). The ability to continuously tune the relevant Kondo-parameters in lithographically defined QDs opened the doors to detailed studies of the Kondo effect (100). Subsequently, systems with two QDs were built (101) and, a few years later, indirect coupling between two QDs was being analyzed (102, 103). In addition, in systems where there is competition between Kondo screening and other many-body interactions, a quantum phase transition (QPT) may occur, including the existence of non-Fermi liquid phases (104, 105). This behavior may be experimentally studied in multi-QD systems (106, 107), in a single QD where there is orbital degeneracy (108), in single-molecule junctions (109, 110), and, more recently, in coupled hybrid metal–semiconductor islands (111).

Here, we are interested in revisiting, using the numerical NRG method (112, 113, 114), one specific double-QD (DQD) arrangement [see Figure 41(a)], where only one of the QDs (QD_0) is connected to the leads, while the other (QD_1) is side-connected to QD_0, forming a T-shape or hanging dot geometry. This system has been shown to exhibit the well-known TSK effect (115, 116, 117, 118, 119, 120, 106, 107, 121, 122, 123, 124, 125, 126, 127, 110), which may happen in a variety of systems where there is more than one localized magnetic moment involved, thus creating an interplay between local and itinerant couplings (115, 116).

For the DQD system with T-shape geometry [see Figure 41(a)] in the TSK regime, QD_0 forms a Kondo state with the leads below a characteristic temperature T_{K_0}, while for $T < T_{K_1} \ll T_{K_0}$, QD_1 forms a Kondo state with the Fermi liquid resulting from the first-stage Kondo effect (117). Our goal is to find an effective *single*-QD system that will reproduce QD_1's Kondo physics (more specifically, its magnetic susceptibility and impurity spectral function) when QD_1 is in the second stage of the TSK effect. Based on the well-known universality of the Kondo effect, one expects that the Kondo physics of QD_1 should be *identical* to that of an effective *single* impurity Anderson model over

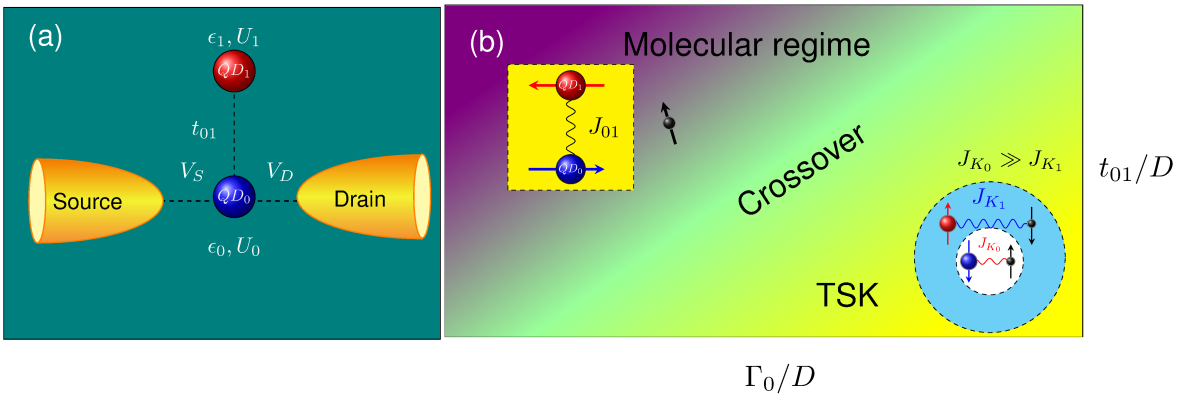

Figure 41 – (a) Schematic diagram of the DQD system in T-shape geometry. Only QD_0 is coupled to the source and drain leads through hoppings V_D and V_S. QD_0 and QD_1 are coupled by a hopping parameter t_{01} and their local energies are given by ϵ_0 and ϵ_1, respectively. The on-site QD Coulomb interactions are U_0 and U_1, where we take $U_0 = U_1 = U$, and we work in the PHS point, i.e., $\epsilon_0 = \epsilon_1 = -U/2$. (b) A schematic representation, in the $t_{01} - \Gamma_0$ parameter space, of the two regimes present in the DQD T-shape geometry system: right lower corner depicts the TSK regime, while the left upper corner contains the molecular regime (see text). The crossover region between these two regimes presents interesting effects resulting from competing interactions between the molecular regime, characterized by $J_{01} \simeq 4t_{01}^2 U$, and the Kondo couplings J_{K_1} and J_{K_0}, which control the TSK regime.

a well-defined region of the $t_{01} - \Gamma_0$ parameter space with $U_{eff} = U_1$, $\epsilon_{eff} = \epsilon_1$, and with effective hybridization Γ_{eff} that is a function of t_{01} and Γ_0. How well this effective model reproduces the Kondo properties of QD_1 can then be used to establish the range of values of t_{01} and Γ_0 where the DQD system is indeed in a TSK regime. We will see that this approach is very useful in defining that range, and that, in reality, it is found to be quite restricted.

As depicted in Figure 41(b), the main result obtained in this work is the determination of a region in the $t_{01} - \Gamma_0$ parameter space where a true TSK regime occurs. This regime, located in the lower right-corner of Figure 41(b), lies below a critical ratio $\frac{t_{01}}{\Gamma_0}$, where the dominance of the coupling to the leads over the interdot coupling allows the sequential Kondo effects to occur. In this regime, the dominant interactions are the Kondo interactions J_{K_0} and J_{K_1} (128), with $J_{K_0} \gg J_{K_1}$. On the opposite corner, in Fig. 41(b), lies the molecular regime, where the ratio $\frac{t_{01}}{\Gamma_0}$ is such that $J_{01} \simeq \frac{4t_{01}^2}{U}$ dominates, locking the QDs into a singlet, effectively disconnecting the DQD spins from the Fermi sea. The TSK and molecular regimes are separated by a crossover region, where these interactions compete. Finding the effective model that defines the TSK region may help design T-shape experimental setups to precisely tune the system into this region, and from there move into the crossover region and explore its properties.

6.2 Model and Hamiltonian

In Figure 41(a), we show the system being analyzed in this work. Quantum dot QD_0 is connected to source and drain leads through hoppings V_S and V_D, respectively, while QD_1 is coupled only to QD_0 through a hopping t_{01}. We model this system through a double-impurity Anderson model, whose Hamiltonian is given by $H = H_{\rm DQD} + H_{\rm leads} + H_{\rm hyb}$, where the first term ($H_{\rm DQD}$), describing the DQD, is

$$H_{\rm DQD} = \sum_{i\sigma} \epsilon_i n_{i\sigma} + \sum_i U_i n_{i\uparrow} n_{i\downarrow} - t_{01} \sum_\sigma \left(d^\dagger_{0\sigma} d_{1\sigma} + \text{ H.c. } \right), \tag{88}$$

where $i = 0, 1$ labels the QDs, $n_{i\sigma} = d^\dagger_{i\sigma} d_{i\sigma}$ is the number operator for QD_i, thus $d_{i\sigma}$ annihilates an electron with spin $\sigma = \uparrow, \downarrow$ in QD_i, while U_i is the Coulomb repulsion in QD_i and ϵ_i is its orbital energy. Finally, t_{01} is the amplitude for interdot hopping. The second term ($H_{\rm leads}$), describing the source ($r = S$) and drain ($r = D$) leads, is given by

$$H_{\rm leads} = \sum_{\vec{k}\sigma r} \epsilon_{r\vec{k}\sigma} n_{r\vec{k}\sigma}, \tag{89}$$

where $n_{r\vec{k}\sigma} = c^\dagger_{r\vec{k}\sigma} c_{r\vec{k}\sigma}$ is the number operator for a state with energy $\epsilon_{r\vec{k}\sigma}$ in lead r. The third term, containing the coupling between QD_0 and the leads, is given by

$$H_{\rm hyb} = \sum_{\vec{k}\sigma r} \left(V_{r\vec{k}\sigma} d^\dagger_{0\sigma} c_{r\vec{k}\sigma} + \text{ H.c. } \right), \tag{90}$$

where $V_{r\vec{k}\sigma}$ is the (spin conserving) hopping from QD_0 to lead $r = S, D$. Taking $V_{S\vec{k}\sigma} = V_{D\vec{k}\sigma} = V_0$, QD_0 couples only to the symmetric combination of both leads, through hopping $V = \sqrt{2} V_0$; then the hybridization between QD_0 and the band is given by $\Gamma_0 = \pi V^2 \rho_0$, where ρ_0 is the lead density of states (DOS) at the Fermi energy. For simplicity, we chose to take $V_S = V_D$, since, as is well known in Kondo physics, this simplifies the problem, without introducing any spurious effects (128). We also consider the metallic host as having a uniform (flat) DOS in the interval $-D \leq \omega \leq D$, where $D = 1$, half of the bandwidth, is the energy unit. In addition, for simplicity, we consider $U_0 = U_1 = U$ and $\epsilon_0 = \epsilon_1 = \frac{-U}{2}$, i.e., that the system is in the particle-hole symmetric (PHS) point. For most of the calculations, we have used the discretization parameter $\Lambda = 2.0$ and kept at least 5000 states at each iteration. We also employ the z-trick (129) (with $z = 0.25$, 0.5, 0.75, and 1.0, i.e., $N_z = 4$) to remove oscillations (artifacts) in the physical quantities (for examples of its use, see Ref. (130)). The thermodynamic quantities were calculated using the traditional single-shell approximation, while the dynamical quantities (spectral function) were calculated using the density matrix NRG approximation (131).

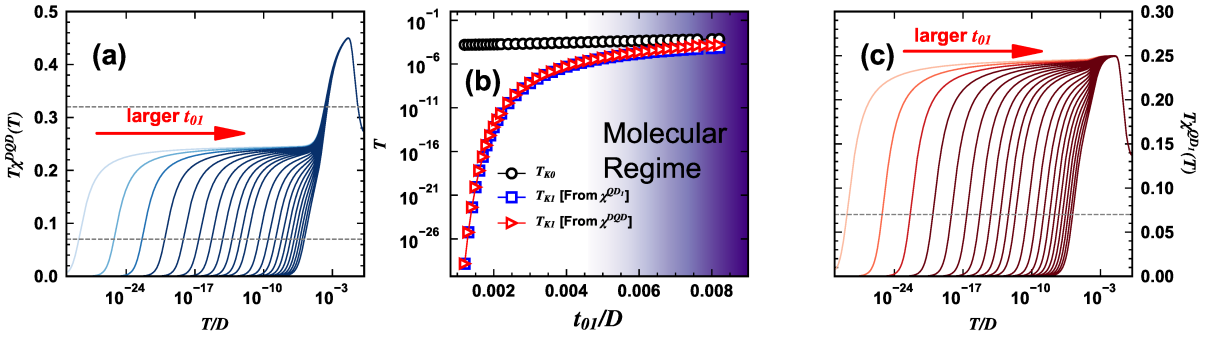

Figure 42 – (a) $T\ \chi^{DQD}(T)$ vs T for $U = 0.5$, $\Gamma_0 = 0.035$ and $0.0012 \leq t_{01} \leq 0.0022$ in steps of 0.0001, and for $0.0024 \leq t_{01} \leq 0.0044$ in steps of 0.0002. The red arrow indicates increasing t_{01} values. (b) Variation of both Kondo temperatures with t_{01}, T_{K_0} (black circles) and T_{K_1} (blue squares and red triangles), for the same Γ_0 as in (a). As expected, T_{K_0} is very weakly dependent on t_{01}, while T_{K_1} varies by ≈ 20 orders of magnitude and takes extremely low values for the smaller t_{01} values. The different ways of obtaining T_{K_1} are discussed in the text. The shading on the right side of the panel is to indicate the region where the system is increasingly in a molecular regime, and no longer in a TSK regime. (c) $T\ \chi^{QD_1}(T)$ vs T for the same parameters as in panel (a). The red arrow has the same meaning as in panel (a). The horizontal gray dashed lines in panels (a) and (c) indicate the values of the Wilson criterion parameter α_i discussed in the text.

6.3 NRG Results

6.3.1 Obtaining T_{K_1} in two different ways: defining the magnetic susceptibility for QD_1

We use the Wilson criterion (128) for obtaining T_{K_0} and T_{K_1}, *viz.*, $T_{K_i}\,\chi^{DQD}(T_{K_i}) = \alpha_i$, where $\alpha_0 = 0.25 + 0.07 = 0.32$ and $\alpha_1 = 0.07$. Here, χ^{DQD} is the DQD contribution to the total susceptibility, and it is obtained by calculating the total system susceptibility (including the leads) and subtracting the susceptibility of a reference system, i.e., the system without the DQD (i.e., the Fermi sea or 'bath'). Figure 42(a) shows $T\chi^{DQD}(T)$ as a function of temperature, for $\Gamma_0 = 0.035$, in the interdot coupling range $0.0012 \leq t_{01} \leq 0.0044$. The two horizontal dashed lines indicate the α_i values mentioned above, used to obtain T_{K_i}. Figure 42(b) shows T_{K_0} (black circles) and T_{K_1} (red triangles), as a function of t_{01}, obtained as in Figure 42(a), but now for t_{01} up to 0.0082, i.e., very much inside the molecular regime. The results in panel (b) show that, as t_{01} decreases, T_{K_0} remains almost constant (as expected, since it should depend much more strongly on Γ_0 than on t_{01}), while T_{K_1} decreases by several orders of magnitude. As it will become clearer below, for a fixed value of Γ_0 there is a t_{01} value above which the system crosses into the molecular regime, and there is no more Kondo screening and the quantities T_{K_0} and T_{K_1} cease to be meaningful. The shading in Figure 42(b) is meant to depict the molecular

regime (see Ref. (117)).

By choosing a different reference system, we may calculate the contribution of *just* QD_1 to the susceptibility. Indeed, by subtracting, from the total system susceptibility, the susceptibility of the Fermi sea *plus* QD_0 (coupled to the Fermi sea by Γ_0), we obtain χ^{QD_1}, the QD_1 susceptibility. For the same parameters as in Figure 42(a), $T\chi^{QD_1}(T)$ is shown in Figure 42(c). Applying the Wilson criterion, with $\alpha_1 = 0.07$ [horizontal dashed line in panel (c)], to $T\chi^{QD_1}$, we obtain the blue squares in panel (b). The excellent agreement between the two methods [compare blue squares and red triangles in Figure 42(b)] confirms that the definition of the susceptibility of QD_1 is sound. It is the susceptibility of QD_1, χ^{QD_1}, that will be used to asses the validity of a single impurity Anderson model, here dubbed an effective model, as described in the next section.

6.3.2 The effective model: fixed Γ_0 and varying t_{01}

Based on the universality of the Kondo effect, we expect that the Kondo physics of QD_1 should be, at least in some region of the $t_{01} - \Gamma_0$ parameter space, identical to that of an effective SIAM with $U_{eff} = U_1$, $\epsilon_{eff} = \epsilon_1 = -U2$, and with an effective hybridization Γ_{eff} that should depend on t_{01} and Γ_0. Indeed, Figure 43(a) shows the fitting (black dashed curves) of $T\chi^{QD_1}$ (solid color curves) for the interval $0.0012 \leq t_{01} \leq 0.0038$. By appropriately adjusting the value of Γ_{eff} (which functions as a fitting parameter), for each different value of t_{01} (for $\Gamma_0 = 0.035$), we are able to accurately reproduce the $T\chi^{QD_1}$ results (color curves) in Figure 43(a) over a range of t_{01} values. This is shown by the dashed black curves in Figure 43(a), which faithfully reproduce the $T\chi^{QD_1}$ up to temperatures several orders of magnitude higher than T_{K_1}. As t_{01} increases [panels (b) to (d)], the fitting is accurate only up to lower and lower temperatures, since the system is crossing over to the molecular regime, where the QDs form a local singlet among themselves, and not even the first Kondo stage occurs. It is interesting to contrast what happens in panel (a) (TSK regime), around the local moment (LM) fixed point, for QD_1 and the effective model [see the inset in panel (b)]: since QD_1 is not connected directly to the Fermi sea, it undergoes very small charge fluctuations, thus its susceptibility is very close to 1/4 for all t_{01} values (colored solid curves), while it decreases considerably as Γ_{eff} increases for the effective SIAM (black dashed curves).

Figure 44 presents the Γ_{eff} values as a function of t_{01}. It is interesting to see that the region for smaller values of t_{01} where one expects the TSK to occur (117), presents an almost linear dependence of Γ_{eff} with t_{01}.

6.3.3 QD_1 susceptibility for fixed t_{01} and varying Γ_0

We now analyze χ^{QD_1} for varying coupling to the leads Γ_0 and a fixed t_{01} value. To help interpret these results, one should note that $T\chi$ (if we take a unit value for the

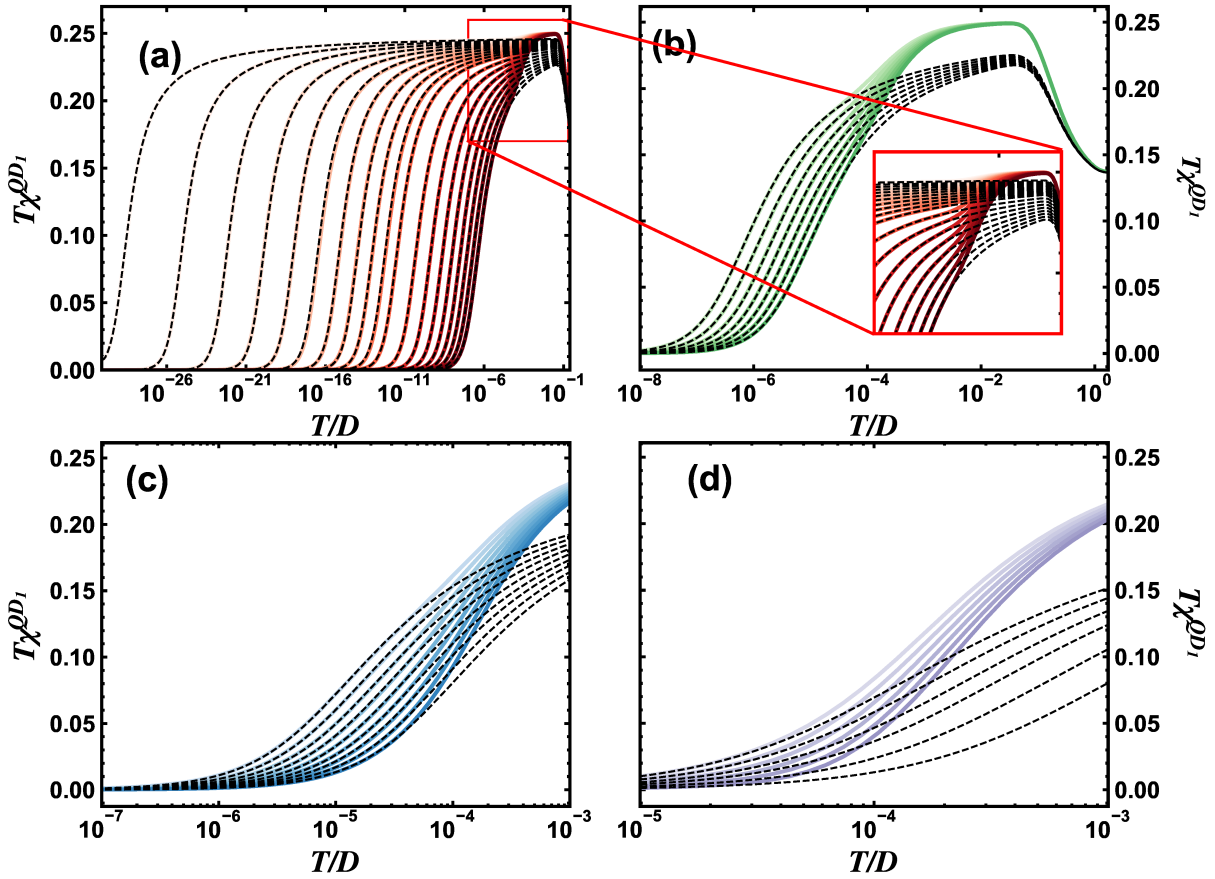

Figure 43 – $T\chi^{QD_1}$ vs. T results (colored solid curves) compared to the results obtained through an effective SIAM (black dashed curves) for different values of t_{01}. Parameters are $U_0 = U_1 = 0.5$, $\epsilon_0 = \epsilon_1 = -U2$, and $\Gamma_0 = 0.035$. (a) $0.0012 \leq t_{01} \leq 0.0022$ in steps of 0.0001 and $0.0024 \leq t_{01} \leq 0.0038$ in steps of 0.0002; (b) $0.0040 \leq t_{01} \leq 0.0052$ in steps of 0.0002; (c) $0.0054 \leq t_{01} \leq 0.0070$ in steps of 0.0002; (d) $0.0072 \leq t_{01} \leq 0.0082$ in steps of 0.0002. The inset in panel (b) is a zoom in of the data in panel (a) of the local moment fixed point temperature range. Panel (a) displays excellent agreement with the effective model in that t_{01} range, which dissipates for higher t_{01} in (b)-(d).

giromagnetic factor g, Bohr magneton μ_B, and Boltzmann constant k_B) measures S_z^2, i.e., the square of the z-component of the magnetic impurity spin. Thus, χ^{DQD} measures $S_{DQD,z}^2$ and χ^{QD_1} measures $S_{1,z}^2$, where $\vec{S}_{DQD} = \vec{S}_0 + \vec{S}_1$. The left panel in Figure 45 shows $T\chi^{QD_1}$ as a function of temperature, in the PHS point, for $0.002 \leq \Gamma_0 \leq 0.042$, $t_{01} = 0.0018$, and $U = 0.5$. The red curve is for $\Gamma_0 = 0.042$ (largest Γ_0 and lowest T_{K_1}), where T_{K_1} increases as Γ_0 decreases (the red arrow points in the direction of decreasing Γ_0 curves). The black curve is for $\Gamma_0 = 0.035$, resulting in $T_{K_1} = 1.05 \times 10^{-15}$. Figure 45(b) shows a zoom of the LM fixed point temperature region. It is interesting to note that, for temperatures just below the LM temperature region (marked by the $S_{1,z}^2 = 14$ plateau), the QD_1 susceptibility for $\Gamma_0 = 0.023$ (gray curve) becomes slightly negative, before vanishing. For progressively smaller Γ_0 values, the susceptibility will dip into more and more negative values, before going through an upturn and then vanishing as $T \to 0$.

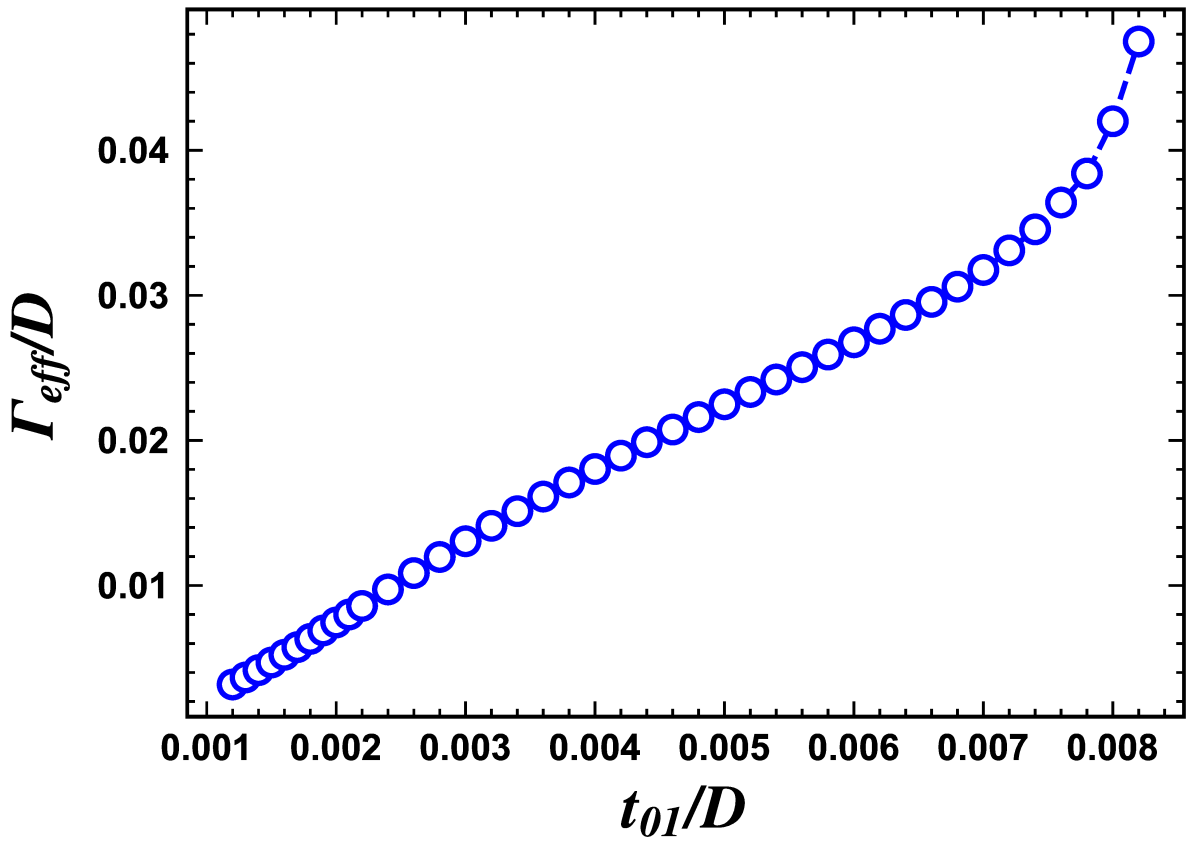

Figure 44 – Γ_{eff} vs t_{01} results (blue circles), as obtained through the fittings done in Figure 43. Notice the initial near linear dependence of Γ_{eff} on t_{01}.

For even smaller Γ_0 values, the dip approaches -14, forming a plateau at this value, eventually upturning and vanishing. This behavior reflects the procedure used to obtain χ^{QD_1} as follows. For $0.001 \leq \Gamma_0 \leq 0.023$ (the smaller Γ_0 values) and $t_{01} = 0.0018$, the system is in the molecular regime (as will be shown in Figure 51). There, for temperatures just below the LM fixed point, the DQD system has $S^2_{DQD,z} \approx 0$, because of the inter-QD singlet formation (see Figure 46). However, since we subtract the susceptibility of QD_0 (our reference in the χ^{QD_1} calculation), which, for this temperature and Γ_0 interval, is of the order of $S^2_{0,z} \lesssim 14$, the result for $T\chi^{QD_1}$ must become negative and then (as Γ_0 decreases) form a plateau at ≈ -14. For temperatures below T_{K_0}, when $S^2_{0,z}$ (the reference) vanishes (due to Kondo), then $S^2_{1,z} - S^2_{0,z}$ also vanishes (since both are ≈ 0). Thus, this calculation of the susceptibility for QD_1 for the smaller Γ_0 values is revealing. It is able to clearly spot the molecular regime (the onset of negative values for $T\,\chi^{QD_1}$), an effect that is not as apparent when we analyze $T\,\chi^{DQD}$ (Fig. 46). Note that the results in Figure 45 indicate that, for $\Gamma_0 \approx 0.023$ (and $t_{01} = 0.0018$) the system is in the final stage of the crossover into the molecular regime.

Figure 46 presents results for $T\,\chi^{DQD}$, as a function of temperature, for the same parameters as in Figure 45. It is interesting to note that there is one specific temperature at which the susceptibility is the same ($T\chi^{DQD} \approx 14$) for all Γ_0, indicated by a blue

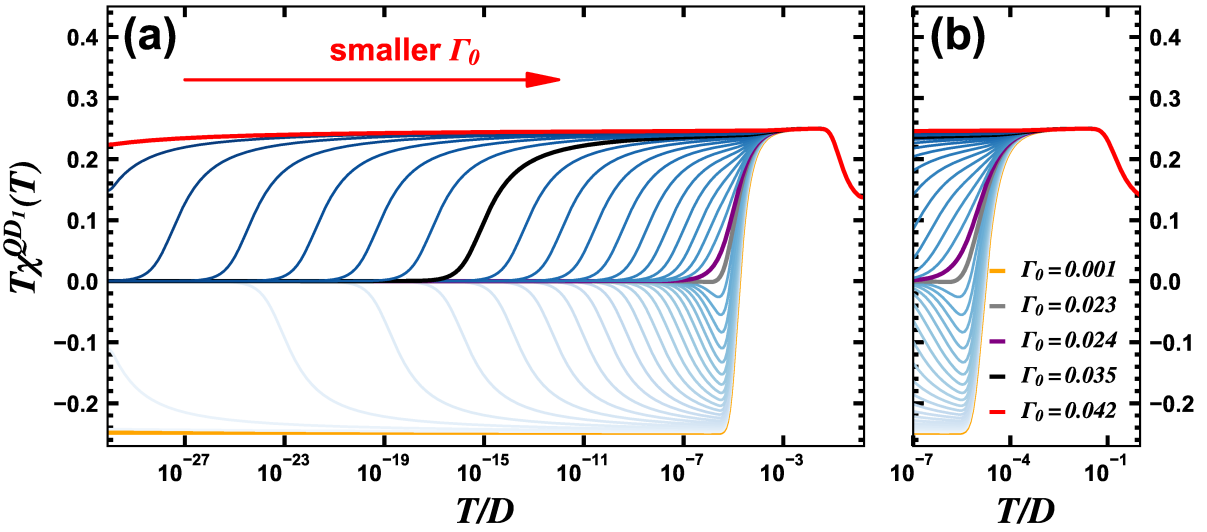

Figure 45 – (a) $T\chi^{QD_1}$ vs T, for $0.002 \leq \Gamma_0 \leq 0.042$. The system is in the PSH point, $U = 0.5$, and $t_{01} = 0.0018$. The red arrow indicates the direction of decreasing Γ_0. (b) Zoom in, around the LM temperature interval, of the data in panel (a). The legend applies to both panels.

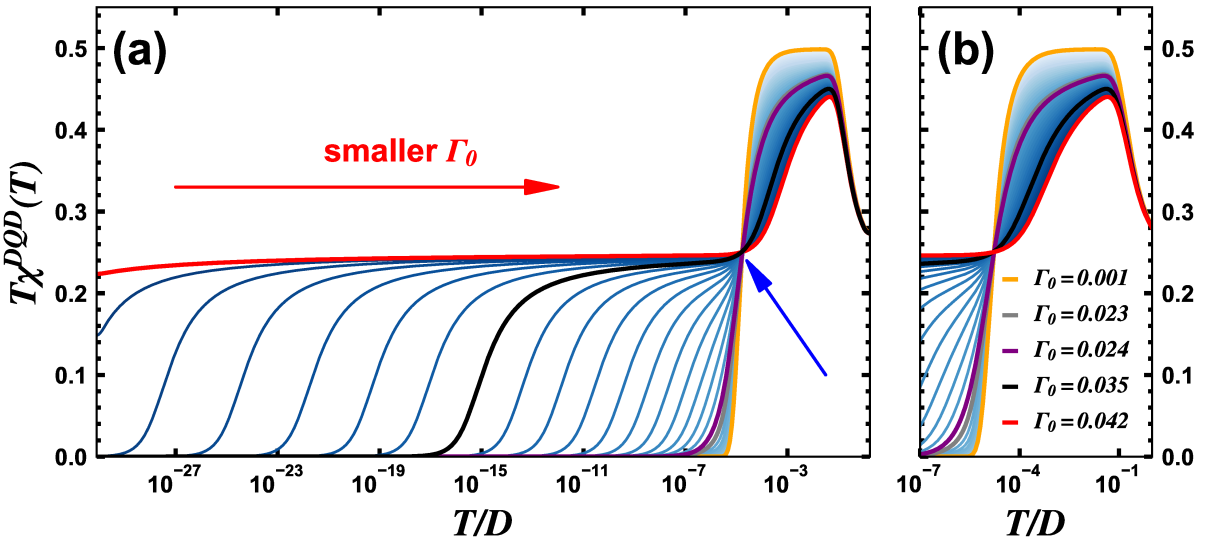

Figure 46 – (a) $T\chi^{DQD}$ vs T for several Γ_0 values. Same parameters and same colors as in Fig. 45. The red arrow points in the direction of decreasing Γ_0 curves. The blue arrow points to the peculiar crossing of all curves in a single point. (b) Zoom in, around the LM temperature interval, of the data in panel (a). The legend applies to both panels.

arrow. This energy scale is of the same order of magnitude as that signaling the crossover into the molecular regime, $\approx 10^{-5}$. We redid the calculations in Figure 46 for different t_{01} values, and obtained that the crossing still occurs at $T\chi^{DQD} \approx 14$, albeit at slightly different temperatures, while the crossing has no dependence on ϵ_d.

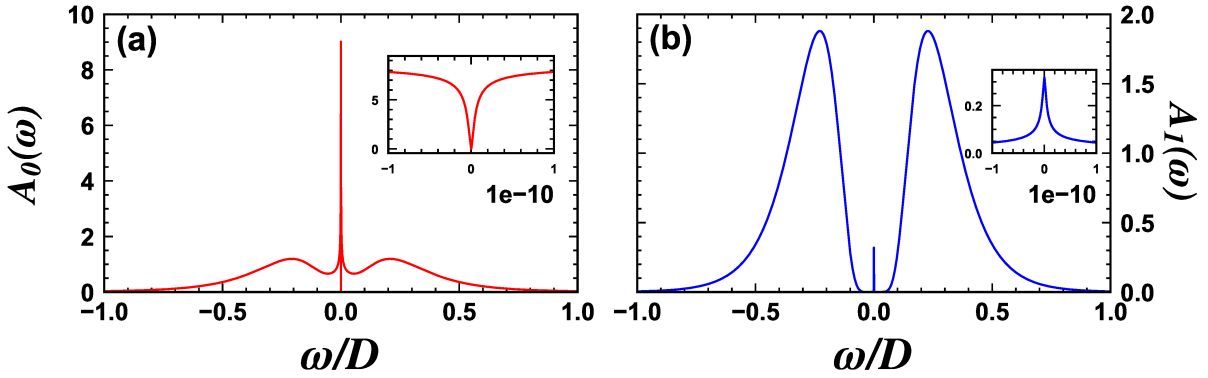

Figure 47 – (a) QD_0 spectral function $A_0(\omega)$ for $\Gamma_0 = 0.035$, $U = 0.5$, and $t_{01} = 0.0022$, in the PHS point. The inset shows the antiresonance 'inside' the Kondo peak. (b) QD_1 spectral function $A_1(\omega)$ for the same parameters as in (a). The inset shows a zoom of the very small Kondo peak in QD_1. The spectral functions in both panels integrate to unity.

6.3.4 QD_1 spectral function and the effective SIAM

As shown in the previous two subsections, the effective model provides an excellent description of the magnetic susceptibility of QD_1, yields a good understanding of the physics around the LM fixed point [see inset in Figure 43(b)], and affords a quantitative way of determining when the system enters the molecular regime. Then, one may ask whether the effective model can describe the dynamic properties of QD_1. Figure 47 shows the spectral functions $A_0(\omega)$ and $A_1(\omega)$, for QD_0 and QD_1, in panels (a) and (b), respectively. The spectral functions were calculated using the density matrix NRG approximation (131). It is well known (117) that an antiresonance appears at the Fermi energy in $A_0(\omega)$, with a characteristic width T_{K_1}. This has been well studied in the literature and it is shown in the inset to Figure 47(a). However, $A_1(\omega)$ has received much less attention (125). Its peculiar shape [blue curve in Figure 47(b)], with a Kondo peak much shorter than the Coulomb blockade peaks, has its origin in the fact that the Friedel Sum Rule for the DQD system has a much different expression from the well-known one for the SIAM (128), as illustrated in the case of a two-level QD system (132), for example. Because of that, it is clear that $A_{eff}(\omega)$ will not simulate $A_1(\omega)$ for an ω-range that includes the Coulomb blockade peaks.

Thus, as shown in Figure 48, we limit the comparison of the spectral functions to an ω-range around the Fermi energy that excludes the Hubbard peak. We normalize to 1 the height of both Kondo peaks, the one obtained from the effective model (black dashed curves) (133) and the one from the DQD (colored solid curves), to facilitate comparison. It is important to stress that no further adjustments are needed to the effective model. In other words, the values of Γ_{eff} used to obtain $A_{eff}(\omega)$ are the ones obtained from the susceptibility fittings in Fig. 43, and shown explicitly in Figure 44 (134). The spectral function comparisons are shown in Figure 48, for $\Gamma_0 = 0.035$ and t_{01} in the interval

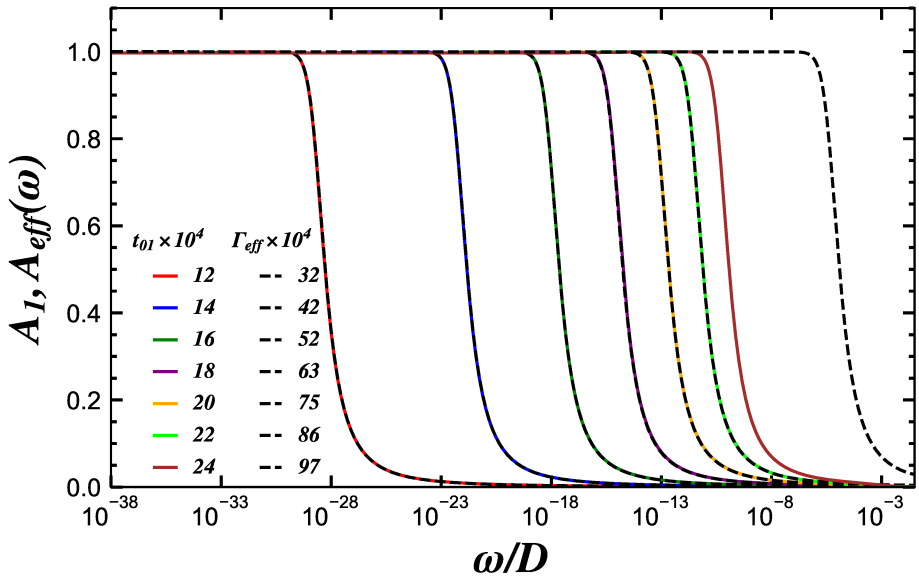

Figure 48 – Comparison between the spectral functions $A_1(\omega)$ (colored solid curves) and $A_{eff}(\omega)$ (dashed black curves) in the range $10^{-38} \leq \omega D \lesssim 10^{-2}$ for several values of t_{01} (as indicated in the legend). Parameters used are $0.0012 \leq t_{01} \leq 0.0024$, $U = 0.5$, $\Gamma_0 = 0.035$, and the system is in the PHS point. The corresponding values of Γ_{eff} are indicated. Note that for $t_{01} = 0.0024$ there is no agreement between $A_1(\omega)$ (solid curve) and $A_{eff}(\omega)$ (dashed curve).

$0.0012 \leq t_{01} \leq 0.0024$, as indicated in the legend. The agreement between $A_1(\omega)$ (colored solid curves) and $A_{eff}(\omega)$ (black dashed curves), up to $t_{01} = 0.0022$ is remarkable. For $t_{01} \geq 0.0024$, the Kondo peaks for QD_1 and the effective model deviate from each other (as shown for $t_{01} = 0.0024$). These results suggest a different criterion to determine the range of t_{01} values where the second Kondo effect can be truly simulated by the SIAM. The spectral function comparisons indicate that the upper limit for t_{01} is considerably smaller than what transpires from the $T\,\chi^{QD_1}$ fittings in Figure 43(a), and what has been often determined in the literature as the TSK-regime range (117).

In the next subsections, we will study some aspects of the inter-QD spin correlation $\langle \vec{S}_0 \cdot \vec{S}_1 \rangle$ and show that its variation with the system parameters (Γ_0 and t_{01}) may be used to further characterize the TSK regime.

6.3.5 Inter-QD spin correlations: Dependence on t_{01}

Figure 49 presents $\langle \vec{S}_0 \cdot \vec{S}_1 \rangle$ for $0.0012 \leq t_{01} \leq 0.0082$, $\Gamma_0 = 0.035$, $U = 0.5$, $T \simeq 10^{-27}$ (ground state), for the system in the PHS point. Three different regions may be discerned. For very small t_{01} values, when the system is in the TSK regime and thus each QD is 'locked' into its own Kondo state, there is very little correlation between the QDs. On the other hand, for the largest t_{01} values (molecular regime), the first Kondo stage does not occur (thus, neither the second), since the two QDs are strongly

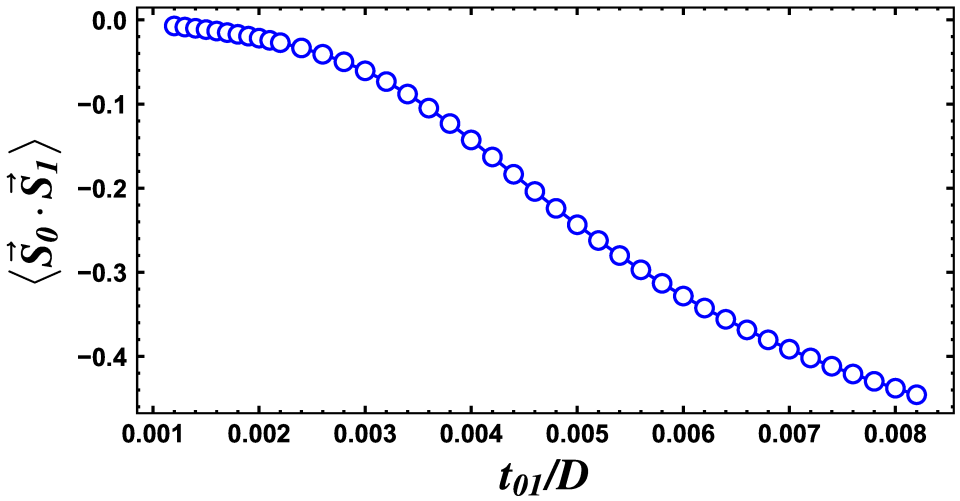

Figure 49 – Ground state ($T \simeq 10^{-27}$) interdot spin correlations. $\langle \vec{S}_0 \cdot \vec{S}_1 \rangle$ vs t_{01} for $U = 0.5$, $\Gamma_0 = 0.035$, with the system in the PHS point.

antiferromagnetically linked by its correlation, which tends to the full singlet value of -34. Then, in an intermediate region of t_{01} values, there is a crossover between the TSK and the molecular regimes.

It is interesting to study $\langle \vec{S}_0 \cdot \vec{S}_1 \rangle$ as a function of temperature in the interval $0.0012 \leq t_{01} \leq 0.0036$, for $\Gamma_0 = 0.035$, $U = 0.5$, in the PHS point. This is shown in Fig. 50(a), also with values of T_{K_1} (yellow circles), T_{K_0} (green up-triangles), and $J_{01} = 4t_{01}^2/U$ (orange right-triangles, representing the effective antiferromagnetic (AF) coupling between the two QDs). The symbols for each of these three energy scales, which depend on t_{01}, are placed on top of the corresponding $\langle \vec{S}_0 \cdot \vec{S}_1 \rangle$ vs T curve. The red curve indicates $t_{01} = 0.0022$, which marks the end of the TSK regime, according to the spectral function analysis of the effective model. At high temperatures, the correlations vanish for all t_{01} values, as expected. As the temperature decreases, AF correlations between the QDs start to develop, and they are enhanced (becoming more negative) even for temperatures below T_{K_0} [marked by the green up-triangles, see zoom ins in panels (b) and (c)], indicating that QD_0 develops singlet correlations simultaneously with the conduction electrons (forming the Kondo singlet) and with QD_1, mainly when in the crossover regime ($t_{01} > 0.0022$). Indeed, inside the crossover regime, $0.0022 < t_{01} \leq 0.0036$, the singlet correlations between the two QDs are strongly enhanced, for temperatures below T_{K_0}, finally settling into a plateau. This can be seen as a precursor to the full molecular regime.

Now, let us analyze the onset of the second Kondo stage for the larger values of t_{01}. It is clear that down to $t_{01} \approx 0.003$ [fourth curve from bottom to top in panel (a)], T_{K_1} marks the temperature where the plateau in $\langle \vec{S}_0 \cdot \vec{S}_1 \rangle$ starts. In contrast, for the smallest values of t_{01}, as shown in panel (b), it is the energy scale J_{01} (orange right-triangles) that marks the onset of the $\langle \vec{S}_0 \cdot \vec{S}_1 \rangle$ plateau. For intermediate values of t_{01}, the plateau onset occurs for an energy scale that is intermediate between J_{01} and T_{K_1}. Note that this

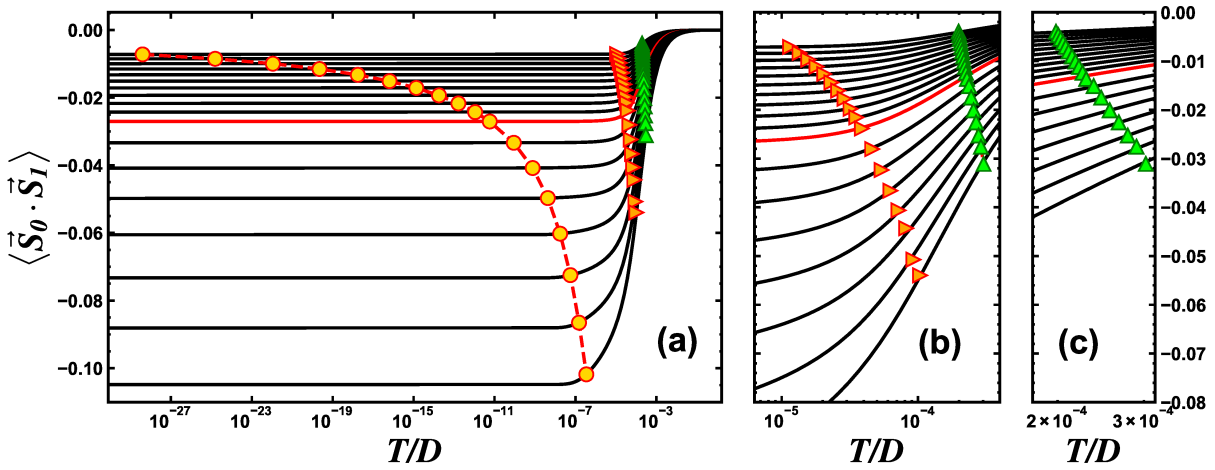

Figure 50 – (a) $\langle \vec{S}_0 \cdot \vec{S}_1 \rangle$ vs T for $0.0012 \leq t_{01} \leq 0.0022$, in steps of 0.0001, and for $0.0022 \leq t_{01} \leq 0.0036$, in steps of 0.0002. Parameters used are $U = 0.5$, $\Gamma_0 = 0.035$, and system in the PHS point. The red curve is for $t_{01} = 0.0022$. The yellow circles indicate T_{K_1}, the orange triangles $J_{01} = 4t_{01}^2 U$, and the green triangles T_{K_0}. (b) and (c) are progressive zoom ins on the data in panel (a) at higher temperatures.

analysis, for $t_{01} > 0.0036$ (for $\Gamma_0 = 0.035$), becomes questionable, since the very use of the T_{K_0} and T_{K_1} energy scales loses its meaning.

One interesting aspect of the results in Figure 50(a) is that for temperatures below T_{K_1} (yellow circles), there is virtually no change in $\langle \vec{S}_0 \cdot \vec{S}_1 \rangle$ as the QD_1 spin is screened by the conduction electrons via the formation of the second Kondo state. This is especially true inside the TSK regime, where the plateau starts at temperatures well above T_{K_1}. In other words, the formation of a correlated state between QD_1 and the conduction electrons (the second Kondo state) does not alter the spin correlation of QD_1 with QD_0.

6.3.6 Inter-QD spin correlations: Dependence on Γ_0

Figure 51 shows how $\langle \vec{S}_0 \cdot \vec{S}_1 \rangle$ varies with Γ_0 for three different t_{01} values, *viz.*, 0.0018, 0.0040, and 0.0082, for $T \simeq 10^{-27}$ (ground state). For very small values of Γ_0 (up to ≈ 0.015) the QDs form a strong singlet ($\langle \vec{S}_0 \cdot \vec{S}_1 \rangle \approx -0.75$, indicated by the solid gray horizontal line), independent of the value of t_{01}. Thus, all three t_{01} values place the system in the molecular regime for such small Γ_0 values. Larger Γ_0 values ($\Gamma_0 \geq 0.025$), show a clear separation between the three curves: for the lowest $t_{01} = 0.0018$ (red circles), $\langle \vec{S}_0 \cdot \vec{S}_1 \rangle$ rapidly vanishes with increasing Γ_0, while for $t_{01} = 0.0040$ (green squares), $\langle \vec{S}_0 \cdot \vec{S}_1 \rangle$ is still strongly AF, but approaches zero as Γ_0 increases, as it will eventually crossover into the TSK regime. The $\langle \vec{S}_0 \cdot \vec{S}_1 \rangle$ results for $t_{01} = 0.0082$ (blue triangles), however, display sizeable AF values for nearly the whole Γ_0 interval in Figure 51, have a markedly different dependence on Γ_0, and become negligible only for Γ_0 values large enough to place QD_0 close to (or into) an intermediate valence regime (128).

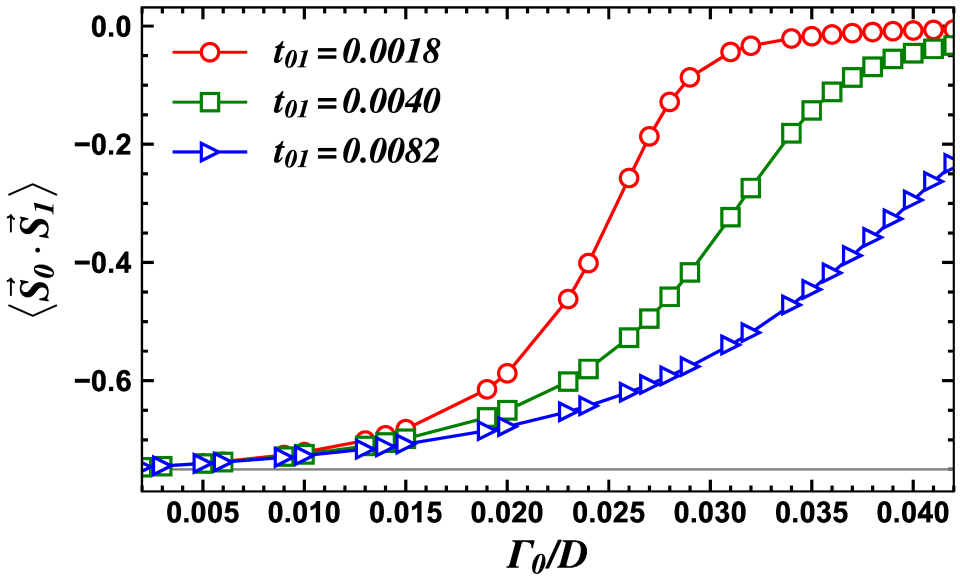

Figure 51 – Ground state $\langle \vec{S}_0 \cdot \vec{S}_1 \rangle$ vs. Γ_0 for $t_{01} = 0.0018$ (red circles), $t_{01} = 0.0040$ (green squares), and $t_{01} = 0.0082$ (blue triangles) for $0.002 \leq \Gamma_0 \leq 0.042$, $U = 0.5$, and system in the PHS point. The horizontal light-gray line indicates the full-singlet value $\langle \vec{S}_0 \cdot \vec{S}_1 \rangle = -3/4$.

Coming back to the $t_{01} = 0.0018$ results (red circles), the spectral function in Fig 48(d) shows that for $\Gamma_0 = 0.035$ the system is well into the TSK regime, since the QD_1 dynamical properties agree with the SIAM effective model. Obviously, larger values of Γ_0 will maintain the system in the TSK regime. The functional form of the red circles curve in Figure 51 seems related to that of the other two curves, which motivates one to explore re-scaling properties. This probing for universal behavior is carried out in the next subsection.

6.3.7 Collapse of the inter-QD spin correlations

Figure 52(a) shows the $\langle \vec{S}_0 \cdot \vec{S}_1 \rangle$ vs Γ_0 curves in the interval $0.0012 \leq t_{01} \leq 0.0082$. In accordance to the discussion above, we use the lowest $t_{01} = 0.0012$ curve in Figure 52(a) as the 'target' curve, and try to collapse higher t_{01}-value curves onto it. We apply the following procedure. First, we choose a 'reference' value, denoted Γ_0^{ref}, inside the TSK region of the target curve. Next, we find what is the Γ_0 value (denoted $\Gamma_0^{0.0012}$) for which $\langle \vec{S}_0 \cdot \vec{S}_1 \rangle (t_{01} = 0.0012, \Gamma_0^{0.0012}) = \langle \vec{S}_0 \cdot \vec{S}_1 \rangle (t_{01}, \Gamma_0^{ref})$, providing the re-scaling factor by which we divide the Γ_0 axis for the t_{01} curve in question, $\xi = \Gamma_0^{ref}/\Gamma_0^{0.0012}$. Panel (b) shows the re-scaled results in the interval $0.0013 \leq t_{01} \leq 0.0023$, using $\Gamma_0^{ref} = 0.027$, where all curves collapse onto the curve for $t_{01} = 0.0012$ (black solid curve). Panel (c) shows that applying the same re-scaling procedure for $t_{01} > 0.0023$ curves does not produce as good a collapse onto the target curve.

It should be noted that the $\langle \vec{S}_0 \cdot \vec{S}_1 \rangle$ curves for larger values of t_{01} [see panel (c)] may

re-scale for larger values of Γ_0^{ref}, at least until a certain value of t_{01}. This reflects the fact that it is the ratio $t_{01}\Gamma_0$ that determines if the system is in the TSK regime or not (as long as Γ_0 does not result in a mixed valence regime).

Figure 53 shows $\langle \vec{S}_0 \cdot \vec{S}_1 \rangle$ as a color map in the $t_{01} - \Gamma_0$ parameter space. We can use it to delineate a region where the TSK regime resides. For that, we use the spectral function results obtained previously, where we found the maximum $t_{01} = 0.0022$ (for $\Gamma_0 = 0.035$) for which the QD_1 Kondo peak could be accurately simulated through the effective model. For these values we obtain $\langle \vec{S}_0 \cdot \vec{S}_1 \rangle (0.0022, 0.035) = -0.027$. Taking that as the lower limit for $\langle \vec{S}_0 \cdot \vec{S}_1 \rangle$, that defines the border of the TSK regime, we obtain the slanted black line close to the lower right corner in Fig. 53. In other words, this is the line where $\langle \vec{S}_0 \cdot \vec{S}_1 \rangle (t_{01}, \Gamma_0) = -0.027$ in the $t_{01} - \Gamma_0$ plane. The yellow region, for which $\langle \vec{S}_0 \cdot \vec{S}_1 \rangle (t_{01}, \Gamma_0) > -0.027$, defines the TSK regime.

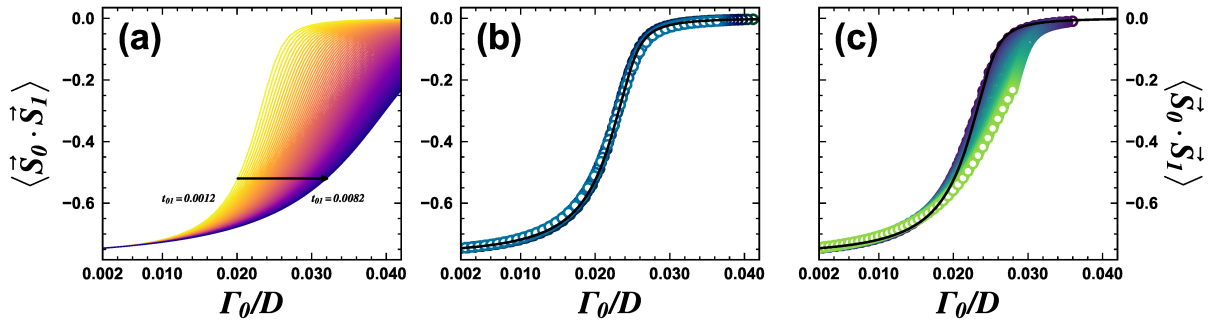

Figure 52 – (a) Ground state $\langle \vec{S}_0 \cdot \vec{S}_1 \rangle$ vs Γ_0 for $0.0012 \leq t_{01} \leq 0.0082$ (from left to right, see horizontal arrow). (b) Re-scaled $0.0012 \leq t_{01} \leq 0.0023$ results, showing their collapse onto the $t_{01} = 0.0012$ curve (black solid line). (c) $\langle \vec{S}_0 \cdot \vec{S}_1 \rangle$ results for the interval $0.0024 \leq t_{01} \leq 0.0082$, showing that these results do not share universality with the lower t_{01} results in panel (b).

6.4 Summary and Conclusions

In summary, we have analyzed a T-shape geometry for a DQD system, using NRG. Our simulation through a two-impurity Anderson model is focused on determining the $t_{01} - \Gamma_0$ parameter region in which the second Kondo stage can be well defined. We were able to show, using an effective SIAM, that the TSK regime occupies a rather restricted sector of parameter space (see Figure 53). The process of obtaining this result required the calculation of the QD_1 susceptibility, its comparison with the susceptibility of an effective SIAM, as well as the comparison of the dynamic properties of QD_1. We found that in the region where the "better-defined" TSK occurs (for fixed Γ_0 and small values of t_{01}), Γ_{eff} depends linearly on t_{01} (see Figure 44).

To supplement the information and perspective that χ^{QD_1} and $A_1(\omega)$ can provide, we also carried out a thorough analysis of the inter-QD spin correlations $\langle \vec{S}_0 \cdot \vec{S}_1 \rangle$. This

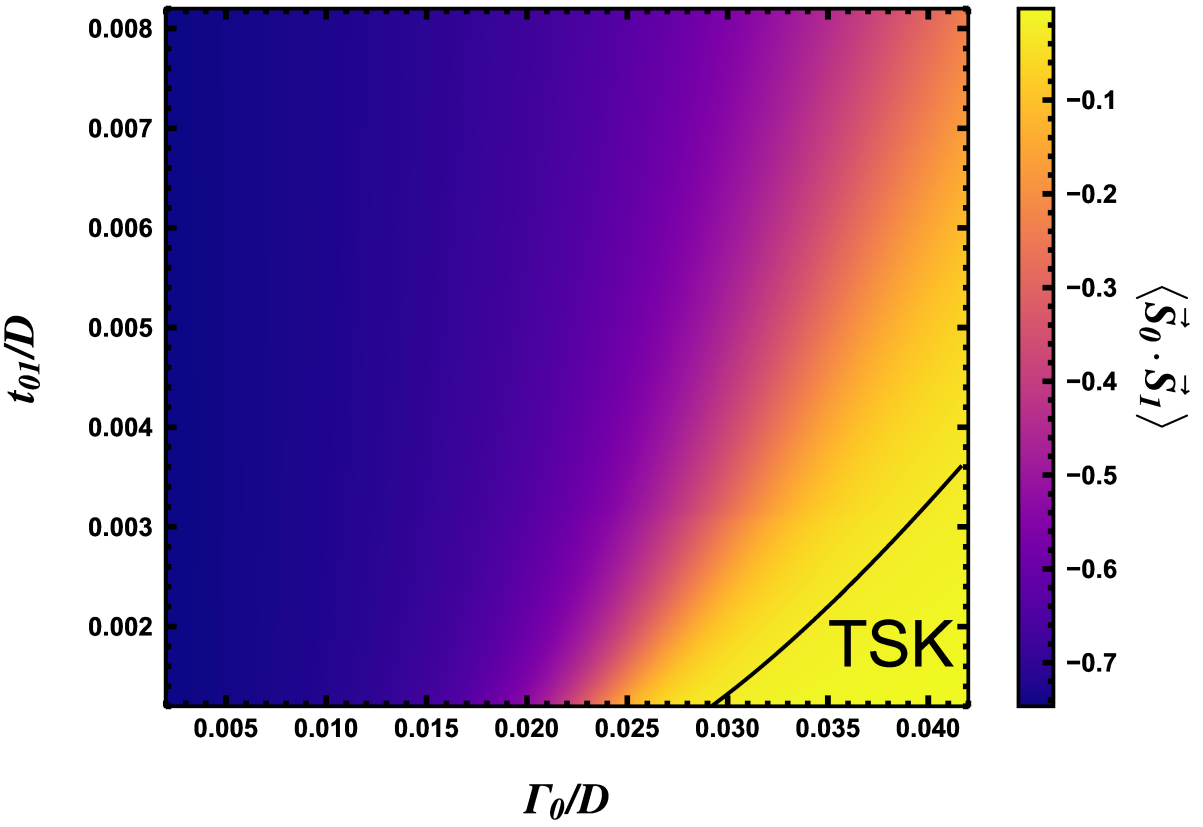

Figure 53 – $\langle \vec{S}_0 \cdot \vec{S}_1 \rangle$ color map in the $t_{01} - \Gamma_0$ parameter space. The solid line is defined as $\langle \vec{S}_0 \cdot \vec{S}_1 \rangle(t_{01}, \Gamma_0) = -0.027$ and delimits the location of the TSK regime, as defined in this work.

allowed us to uncover interesting features of the DQD system, *viz.*, the TSK manifests itself through the appearance of a plateau in the interdot spin correlation for $T < J_{01}$ (see Figure 50) and through the universality of the $\langle \vec{S}_0 \cdot \vec{S}_1 \rangle$ vs Γ_0 curves for small enough t_{01} values.

We anticipate that our results could guide the study of related DQD systems. For example, when the QDs are in a parallel geometry (135), with both QDs connected to the leads (in that case, QD_1 connects through Γ_1 to the Fermi sea, while in T-geometry $\Gamma_1 = 0$). In that system, there is the possibility of a singlet/triplet QPT (136, 137, 125) through variation of the coupling parameters. For instance, when increasing Γ_1 (for fixed Γ_0 and t_{01}), the system eventually goes through a singlet/triplet QPT (as shown in Figure 7(a) in Ref. (125)) (138). It would be important to distinguish what is the character of the singlet-side of the QPT, viz., the TSK, the molecular, or the crossover between them. Our results may provide guidance to experimentalists to better place the system in the desired regime.

Thus, we trust that our analysis allows experimental groups to tune the parameters of a DQD system with T-shape geometry into the true TSK regime. Varying parameters accordingly, they could study the crossover to the molecular regime, and turn on Γ_1 to

study the singlet/triplet QPT starting from different singlet regimes.

Chapter 7

Conclusion

In this work, we have presented a analysis into the physics of magnetic quantum impurity systems, focusing on the Kondo effect and how it manifests within host environments characterized by non-trivial geometries and densities of states, resulting in what we dubbed as "extreme conditions", characterized by either extreme particle-hole asymmetry or energy scales spanning 20 orders of magnitude. For this purpose, we employ the NRG method, originally developed by Wilson in the 1970s, as a fundamental tool. Our work explored the competition between strongly correlated physics in one-dimensional (1D) systems exhibiting spectral singularities and a double quantum dot system arranged in a T-shape geometry. Here, the competition between local and itinerant interactions determines two distinct quantum regimes, characterized by either a "local" singlet (molecular regime) or a sequence of two many-body Kondo singlets (Two Stage Kondo regime). The former system, when non-interacting (Resonant Level model), presents a bound-state below the bottom of the band, whose spectral weight, when the resonant level is positioned right at the singularity, is exactly 2/3 , regardless of its coupling to the conduction electrons. On the other hand, a Hubbard interaction causes the bound state to suffer a series of transformations, including level splitting, transfer of spectral weight, appearance of a spectral discontinuity, changes in binding energy, and development of a finite width.

Study of Kondo regime dependence of bound-state below the continuum

First, we concentrated on analyzing the properties of a magnetic impurity embedded in a host environment that exhibits a density of states singularity of the $\omega^{-1/2}$ type at his bottom, characteristic of 1D quantum wires and graphene nanoribbons. Here, we present a comparison between the non-interacting Resonant Level model with the interacting Single Impurity Anderson Model, revealing discoveries that expand the traditional understanding of the Kondo effect to regimes of extreme particle-hole asymmetry. Non-interacting regimes demonstrated the rise of Dirac δ bound state outside of the continuum. The position and the spectral weight of this bound state were mapped as a function of the

impurity's energy proximity to the singularity and the coupling strength. A key finding is that tuning the impurity resonant level exactly to the energy of the singularity, the bound-state spectral weight approaches a universal value of $Z_b = 2/3$. This universality is notable, as it was verified to be independent of the presence of spin-orbit interaction. When the impurity's resonant level was placed below the band end, the spectral weight of the bound state was consistently larger than 2/3 and increased with δ (distance to the band edge).

The inclusion of the Hubbard U interaction significantly modified the impurity spectrum. NRG revealed that the singularity distorts the lower Coulomb blockade peak, resulting in a complex spectral profile. The non-interacting bound state acquires a finite width, being shifted to lower energies, and the Hubbard correlation generates a discontinuity in the impurity density of states at the band extremity. By analyzing the impurity occupancy as a function of both chemical potential and impurity level energy, we were able to identify the emergence of the re-entrant Kondo regime. Indeed, it was shown that, as the Fermi energy approaches the singularity at the band bottom, the occupancy n_d increases abruptly, and the system partially recovers the characteristics of the strong-coupled Kondo regime. This behavior is accompanied by an abrupt drop in T_K, which returns to values characteristic of the single-valence Kondo regime T_K, even when the parameters would suggest an intermediate-valence regime, where T_K is typically higher. The competition between the singularity and correlations seems to suggest that the bound state forming near the Fermi energy E_F could make the local moment somewhat more stable against charge fluctuations.

Thermodynamic properties confirmed this "resilience" of the local moment fixed point. The impurity magnetic susceptibility indicates that the plateau associated with the local moment fixed point remains around $2/3 \times 1/4$. This pinning of the susceptibility in the local moment fixed point region is attributed to the influence of the bound state with spectral weight $Z_b = 2/3$, suggesting that it renders the local moment more resistant to charge fluctuations. A non-universal finding was the behavior of the impurity entropy, which exhibited temporarily negative values at low temperatures when the resonant level was closer to the singularity. This phenomenon is rare but has been observed in Kondo problems with singularities or discontinuities in the density of states, and here it is more prominent when the impurity orbital level is closer to the band singularity. The evolution of the NRG energy flux near the singularity also showed that the local moment plateau is persistent, compared to the case of E_F at the band center, which validates the conclusion that the system sustains a Kondo state in the vicinity of the singularity.

The findings described above contribute to the understanding of the mechanisms of local moment formation and screening in strongly correlated systems. The observation of a fractional local moment and the stabilization of the local moment near the singularity may contribute to the study of heavy fermions. In practical applications, the results are

important for nanoelectronics and the development of quantum devices based on quantum dots. We also suggest a viable physical implementation for experimental testing of our results: the equivalence between the quantum wire singularity and the density of states of armchair graphene nanoribbons was established, indicating that these semiconductor materials can serve as controllable hosts for the study of Kondo in one-dimensional hosts.

T-shape Double Quantum Dot: Molecular vs. Two-stage-Kondo regimes

We then turned our attention to the Two-Stage Kondo effect (TSK) in a double quantum dot system in a T-shaped geometry. The TSK is required to understand the competition between a Kondo singlet and a "molecular" singlet. This establishes a criterion for delimiting a "pure" TSK regime. We demonstrated that this regime occurs in a restricted sector of the parameter space $t_{01} - \Gamma_0$ (inter-dot coupling and hybridization of the QD connected to the leads), in which the physics of the second Kondo stage can be described with high accuracy by an effective Single Impurity Anderson model. Fitting the magnetic susceptibility of QD_1 revealed that the effective hybridization is the only necessary fitting parameter, which exhibits a nearly linear dependence on t_{01} for small values of the effective coupling.

The analysis of QD_1 spectral weight revealed the need for an even more strict criterion to determine the real TSK regime. The comparison between the QD_1 spectral function and the effective model spectral function showed that the excellent agreement diminished for higher values of t_{01}, especially for the Kondo peak. This suggests that the upper limit for the region of interest is more restricted than inferred from the χ_{QD1} results alone. The investigation of inter-QD spin correlations in the ground state complemented this delimitation, revealing three regions: TSK, enhanced crossing below T_{K_0}, and molecular (trending toward the full singlet value $-3/4$). The TSK regime limit was quantitatively defined by the contour line $\langle \vec{S}_0 \cdot \vec{S}_1 \rangle = -0.027$ in the parameter space $t_{01} - \Gamma_0$. Additionally, it was shown that in this specific phase, the $\langle \vec{S}_0 \cdot \vec{S}_1 \rangle$ versus Γ_0 curves exhibit universal curve collapse when rescaled.

The TSK effect is a prototypical system for the study of multiple competing quantum moments. The parameter map and the $\langle \vec{S}_0 \cdot \vec{S}_1 \rangle$ criterion provide experimenters with an exact prescription for tuning T-shape DQD devices in the TSK or crossover regimes. In DQD systems, understanding of the TSK could be seen as significant for directing experiments toward tuning T-shaped geometries, specifically with the goal of reaching the pure TSK regime.

In summary, we believe this work achieves its goals by mapping and characterizing strong correlation regimes in quantum impurity systems under different host environments through the use of the NRG method.

Bibliography

1 COLEMAN, P. Heavy fermions and the kondo lattice: a 21st century perspective (2015). **arXiv preprint arXiv:1509.05769**. Disponível em: <https://arxiv.org/abs/1509.05769>.

2 SARACHIK, M.; CORENZWIT, E.; LONGINOTTI, L. Resistivity of mo-nb and mo-re alloys containing 1% fe. **Physical Review**, APS, v. 135, n. 4A, p. A1041, 1964. Disponível em: <https://doi.org/10.1103/PhysRev.135.A104>.

3 PAVARINI, E.; COLEMAN, P.; KOCH, E. **Many-body physics: from Kondo to Hubbard**. [S.l.], 2015. Disponível em: <https://juser.fz-juelich.de/record/205123>.

4 FABRIZIO, M. Kondo effect and the physics of the anderson impurity model. In: **A Course in Quantum Many-Body Theory: From Conventional Fermi Liquids to Strongly Correlated Systems**. Springer, 2022. p. 313–343. Disponível em: <https://link.springer.com/chapter/10.1007/978-3-031-16305-0_7>.

5 MOCA, C. P. et al. Kondo cloud in a superconductor. **Physical Review Letters**, APS, v. 127, n. 18, p. 186804, 2021. Disponível em: <https://doi.org/10.1103/PhysRevLett.127.186804>.

6 BORZENETS, I. V. et al. Observation of the kondo screening cloud. **Nature**, Nature Publishing Group UK London, v. 579, n. 7798, p. 210–213, 2020. Disponível em: <https://doi.org/10.1038/s41586-020-2058-6>.

7 COLEMAN, P. Local moment physics in heavy electron systems. **arXiv preprint cond-mat/0206003**, 2002. Disponível em: <https://doi.org/10.48550/arXiv.cond-mat/0206003>.

8 SASAKI, S. et al. Kondo effect in an integer-spin quantum dot. **Nature**, Nature Publishing Group UK London, v. 405, n. 6788, p. 764–767, 2000. Disponível em: <https://doi.org/10.1038/35015509>.

9 CRONENWETT, S. M.; OOSTERKAMP, T. H.; KOUWENHOVEN, L. P. A tunable kondo effect in quantum dots. **Science**, American Association for the Advancement of Science, v. 281, n. 5376, p. 540–544, 1998. Disponível em: <https://www.science.org/doi/10.1126/science.281.5376.540>.

10 KRISHNA-MURTHY, H.; WILKINS, J.; WILSON, K. Renormalization-group approach to the anderson model of dilute magnetic alloys. i. static properties for the symmetric case. **Physical Review B**, APS, v. 21, n. 3, p. 1003, 1980. Disponível em: <https://doi.org/10.1103/PhysRevB.21.1003>.

11 BULLA, R.; COSTI, T. A.; PRUSCHKE, T. Numerical renormalization group method for quantum impurity systems. **Reviews of Modern Physics**, APS, v. 80, n. 2, p. 395–450, 2008. Disponível em: <https://doi.org/10.1103/RevModPhys.80.395>.

12 SI, Q. et al. Locally critical quantum phase transitions in strongly correlated metals. **Nature**, Nature Publishing Group UK London, v. 413, n. 6858, p. 804–808, 2001. Disponível em: <https://doi.org/10.1038/35101507>.

13 SHIBA, H. Properties of strongly correlated fermi liquid in valence fluctuation system—a variational monte-carlo study. **Journal of the Physical Society of Japan**, The Physical Society of Japan, v. 55, n. 8, p. 2765–2776, 1986. Disponível em: <https://doi.org/10.1143/JPSJ.55.2765>.

14 SHAGINYAN, V. et al. Scaling behavior of heavy fermion metals. **Physics reports**, Elsevier, v. 492, n. 2-3, p. 31–109, 2010. Disponível em: <https://doi.org/10.1016/j.physrep.2010.03.001>.

15 MIRANDA, E.; DOBROSAVLJEVIĆ, V. Disorder-driven non-fermi liquid behaviour of correlated electrons. **Reports on Progress in Physics**, IOP Publishing, v. 68, n. 10, p. 2337, 2005. Disponível em: <https://iopscience.iop.org/article/10.1088/0034-4885/68/10/R02>.

16 COLEMAN, P. **Introduction to many-body physics**. Cambridge University Press, 2015. Disponível em: <https://doi.org/10.1017/CBO9781139020916>.

17 GEGENWART, P.; SI, Q.; STEGLICH, F. Quantum criticality in heavy-fermion metals. **nature physics**, Nature Publishing Group UK London, v. 4, n. 3, p. 186–197, 2008. Disponível em: <https://www.nature.com/articles/nphys892>.

18 CUSTERS, J. et al. The break-up of heavy electrons at a quantum critical point. **Nature**, Nature Publishing Group UK London, v. 424, n. 6948, p. 524–527, 2003. Disponível em: <https://www.nature.com/articles/nature01774>.

19 de Haas, W.; de Boer, J.; van den Berg, G. The electrical resistance of gold, copper and lead at low temperatures. **Physica**, v. 1, p. 1115, 1934. Disponível em: <https://doi.org/10.1016/S0031-8914(34)80310-2>.

20 ALLDREDGE, O. R.; DEFORD, J.; SOSIN, A. Deviation from matthiessen's rule in electron-irradiated copper. **Physical Review B**, APS, v. 11, n. 8, p. 2860, 1975. Disponível em: <https://doi.org/10.1103/PhysRevB.11.2860>.

21 KONDO, J. Resistance minimum in dilute magnetic alloys. **Prog. Theor. Exp. Phys.**, v. 32, p. 37, 1964. Disponível em: <https://doi.org/10.1143/PTP.32.37>.

22 WILSON, K. G. The renormalization group: Critical phenomena and the kondo problem. **Reviews of modern physics**, APS, v. 47, n. 4, p. 773, 1975. Disponível em: <https://doi.org/10.1103/RevModPhys.47.773>.

23 NOZIERES, P.; BLANDIN, A. Kondo effect in real metals. **Journal de Physique**, Société Française de Physique, v. 41, n. 3, p. 193–211, 1980. Disponível em: <https://doi.org/10.1051/jphys:01980004103019300>.

24 GOLDHABER-GORDON, D. et al. Kondo effect in a single-electron transistor. **Nature**, Nature Publishing Group UK London, v. 391, n. 6663, p. 156–159, 1998. Disponível em: <https://doi.org/10.1038/34373>.

25 GAN, J.; WONG, E. Non-fermi-liquid behavior in quantum critical systems. **Physical review letters**, APS, v. 71, n. 25, p. 4226, 1993. Disponível em: <https://doi.org/10.1103/PhysRevLett.71.4226>.

26 PARCOLLET, O. et al. Overscreened multichannel su (n) kondo model: Large-n solution and conformal field theory. **Physical Review B**, APS, v. 58, n. 7, p. 3794, 1998. Disponível em: <https://journals.aps.org/prb/abstract/10.1103/PhysRevB.58.3794>.

27 TSUNETSUGU, H.; SIGRIST, M.; UEDA, K. The ground-state phase diagram of the one-dimensional kondo lattice model. **Reviews of Modern Physics**, APS, v. 69, n. 3, p. 809, 1997. Disponível em: <https://doi.org/10.1103/RevModPhys.69.809>.

28 KOUWENHOVEN, L.; GLAZMAN, L. Revival of the kondo effect. **Physics world**, IOP Publishing, v. 14, n. 1, p. 33, 2001. Disponível em: <https://iopscience.iop.org/article/10.1088/2058-7058/14/1/28>.

29 HANSON, R. et al. Spins in few-electron quantum dots. **Reviews of modern physics**, APS, v. 79, n. 4, p. 1217–1265, 2007. Disponível em: <https://doi.org/10.1103/RevModPhys.79.1217>.

30 MATSUSHITA, Y. et al. Evidence for charge kondo effect in superconducting tl-doped pbte. **Physical review letters**, APS, v. 94, n. 15, p. 157002, 2005. Disponível em: <https://doi.org/10.1103/PhysRevLett.94.157002>.

31 ZENG, H. et al. Kondo effect and superconductivity in niobium with iron impurities. **Scientific Reports**, Nature Publishing Group UK London, v. 11, n. 1, p. 14256, 2021. Disponível em: <https://www.nature.com/articles/s41598-021-93731-6>.

32 XIN, X.; ZHOU, D. Kondo effect in a topological insulator quantum dot. **Physical Review B**, APS, v. 91, n. 16, p. 165120, 2015. Disponível em: <https://doi.org/10.1103/PhysRevB.91.165120>.

33 KOURRIS, C.; VOJTA, M. Kondo screening and coherence in kagome local-moment metals: Energy scales of heavy fermions in the presence of flat bands. **Physical Review B**, APS, v. 108, n. 23, p. 235106, 2023. Disponível em: <https://doi.org/10.1103/PhysRevB.108.235106>.

34 TRAN, M.-T.; NGUYEN, T. T. Molecular kondo effect in flat-band lattices. **Physical Review B**, APS, v. 97, n. 15, p. 155125, 2018. Disponível em: <https://doi.org/10.1103/PhysRevB.97.155125>.

35 AFFLECK, I. Quantum impurity problems in condensed matter physics. **Exact Methods in Low-dimensional Statistical Physics and Quantum Computing**, v. 89, p. 3–65, 2008. Disponível em: <https://books.google.com.br/books?hl=pt-BR&lr=&id=cLEVDAAAQBAJ&oi=fnd&pg=PA3&dq=Quantum+impurity+problems+

in+condensed+matter+physics&ots=Na2IcGYUd1&sig=LIut4I2oQZlT6NSiP_MNtlNN-sU&redir_esc=y#v=onepage&q&f=false>.

36 GULL, E. et al. Continuous-time monte carlo methods for quantum impurity models. **Reviews of Modern Physics**, APS, v. 83, n. 2, p. 349–404, 2011. Disponível em: <https://doi.org/10.1103/RevModPhys.83.349>.

37 SMITH, J.; KMETKO, E. Magnetism or bonding: A nearly periodic table of transition elements. **Journal of the Less Common Metals**, Elsevier, v. 90, n. 1, p. 83–88, 1983. Disponível em: <https://doi.org/10.1016/0022-5088(83)90119-4>.

38 FISK, Z. et al. The physics and chemistry of heavy fermions. **Proceedings of the National Academy of Sciences**, v. 92, n. 15, p. 6663–6667, 1995. Disponível em: <https://doi.org/10.1073/pnas.92.15.6663>.

39 MOSALI, V. S. S.; BOND, A. M.; ZHANG, J. Alloying strategies for tuning product selectivity during electrochemical co 2 reduction over cu. **Nanoscale**, Royal Society of Chemistry, v. 14, n. 42, p. 15560–15585, 2022. Disponível em: <https://pubs.rsc.org/en/content/articlehtml/2022/nr/d2nr03539a?casa_token=zWxfIwz4eAIAAAAA:1nAzfNm-SQ0Kcd5NQW3WIMevo3g9g6KSWDsNKCyIiSh9Xw1wOz7NotluT_5EIeHwEUV7Ubyoun59wAqW>.

40 KASUYA, T. A theory of metallic ferro-and antiferromagnetism on zener's model. **Progress of theoretical physics**, Oxford University Press, v. 16, n. 1, p. 45–57, 1956. Disponível em: <https://doi.org/10.1143/PTP.16.45>.

41 HEWSON, A. C. **The Kondo problem to heavy fermions**. Cambridge university press, 1997. Disponível em: <https://doi.org/10.1017/CBO9780511470752>.

42 MADHAVAN, V. et al. Tunneling into a single magnetic atom: spectroscopic evidence of the kondo resonance. **Science**, American Association for the Advancement of Science, v. 280, n. 5363, p. 567–569, 1998. Disponível em: <https://www.science.org/doi/10.1126/science.280.5363.567>.

43 AFFLECK, I.; BORDA, L.; SALEUR, H. Friedel oscillations and the kondo screening cloud. **Physical Review B—Condensed Matter and Materials Physics**, APS, v. 77, n. 18, p. 180404, 2008. Disponível em: <https://journals.aps.org/prb/abstract/10.1103/PhysRevB.77.180404>.

44 SIMON, P.; AFFLECK, I. Kondo screening cloud effects in mesoscopic devices. **Physical Review B**, APS, v. 68, n. 11, p. 115304, 2003. Disponível em: <https://doi.org/10.1103/PhysRevB.68.115304>.

45 AFFLECK, I.; SIMON, P. Detecting the kondo screening cloud around a quantum dot. **Physical Review Letters**, APS, v. 86, n. 13, p. 2854, 2001. Disponível em: <https://doi.org/10.1103/PhysRevLett.86.2854>.

46 ANDERSON, P. W. Localized magnetic states in metals. **Physical Review**, APS, v. 124, n. 1, p. 41, 1961. Disponível em: <https://doi.org/10.1103/PhysRev.124.41>.

47 KOUWENHOVEN, L. P. et al. Electron transport in quantum dots. In: **Mesoscopic electron transport**. Springer, 1997. p. 105–214. Disponível em: <https://doi.org/10.1007/978-94-015-8839-3_4>.

48 KASTNER, M. A. The single-electron transistor. **Reviews of modern physics**, APS, v. 64, n. 3, p. 849, 1992. Disponível em: <https://doi.org/10.1103/RevModPhys.64.849>.

49 KLOEFFEL, C.; LOSS, D. Prospects for spin-based quantum computing in quantum dots. **Annu. Rev. Condens. Matter Phys.**, Annual Reviews, v. 4, n. 1, p. 51–81, 2013. Disponível em: <https://doi.org/10.1146/annurev-conmatphys-030212-184248>.

50 KOUWENHOVEN, L.; MARCUS, C. Quantum dots. **Physics World**, IOP Publishing, v. 11, n. 6, p. 35, 1998. Disponível em: <https://iopscience.iop.org/article/10.1088/2058-7058/11/6/26>.

51 COSTI, T. Wilson's numerical renormalization group. In: SPRINGER. **Density-Matrix Renormalization: A New Numerical Method in Physics Lectures of a Seminar and Workshop Held at the Max-Planck-Institut für Physik komplexer Systeme Dresden, Germany, August 24th to September 18th, 1998**. 2007. p. 3–25. Disponível em: <https://link.springer.com/chapter/10.1007/BFb0106063>.

52 BULLA, R.; PRUSCHKE, T.; HEWSON, A. Anderson impurity in pseudo-gap fermi systems. **Journal of Physics: Condensed Matter**, IOP Publishing, v. 9, n. 47, p. 10463, 1997. Disponível em: <https://iopscience.iop.org/article/10.1088/0953-8984/9/47/014>.

53 MANCHON, A. et al. New perspectives for rashba spin–orbit coupling. **Nature materials**, Nature Publishing Group UK London, v. 14, n. 9, p. 871–882, 2015. Disponível em: <https://doi.org/10.1038/nmat4360>.

54 WINKLER, R. et al. Spin-orbit coupling in two-dimensional electron and hole systems. In: **Advances in Solid State Physics**. Springer, 2001. p. 211–223. Disponível em: <https://link.springer.com/chapter/10.1007/3-540-44946-9_18>.

55 MIRELES, F.; KIRCZENOW, G. Ballistic spin-polarized transport and rashba spin precession in semiconductor nanowires. **Physical Review B**, APS, v. 64, n. 2, p. 024426, 2001. Disponível em: <https://doi.org/10.1103/PhysRevB.64.024426>.

56 MEIRAV, U.; KASTNER, M.; WIND, S. Single-electron charging and periodic conductance resonances in gaas nanostructures. **Physical review letters**, APS, v. 65, n. 6, p. 771, 1990. Disponível em: <https://doi.org/10.1103/PhysRevLett.65.771>.

57 BRUCH, A. et al. Quantum thermodynamics of the driven resonant level model. **Physical Review B**, APS, v. 93, n. 11, p. 115318, 2016. Disponível em: <https://doi.org/10.1103/PhysRevB.93.115318>.

58 AGARWALA, A.; SHENOY, V. B. Quantum impurities develop fractional local moments in spin-orbit coupled systems. **Physical Review B**, APS, v. 93, n. 24, p. 241111, 2016. Disponível em: <https://doi.org/10.1103/PhysRevB.93.241111>.

59 DRESSELHAUS, G. Spin-orbit coupling effects in zinc blende structures. **Physical Review**, APS, v. 100, n. 2, p. 580, 1955. Disponível em: <https://doi.org/10.1103/PhysRev.100.580>.

60 BYCHKOV, Y. A.; RASHBA, E. I. Oscillatory effects and the magnetic susceptibility of carriers in inversion layers. **Journal of physics C: Solid state physics**, IOP Publishing, v. 17, n. 33, p. 6039, 1984. Disponível em: <https://doi.org/10.1088/0022-3719/17/33/015>.

61 LOPES, V. et al. Kondo effect under the influence of spin–orbit coupling in a quantum wire. **Journal of Physics: Condensed Matter**, IOP Publishing, v. 32, n. 43, p. 435604, 2020. Disponível em: <https://iopscience.iop.org/article/10.1088/1361-648X/aba45c>.

62 BRUUS, H.; FLENSBERG, K. **Many-body quantum theory in condensed matter physics: an introduction**. Oxford university press, 2004. Disponível em: <https://books.google.com.br/books?hl=pt-BR&lr=&id=CktuBAAAQBAJ&oi=fnd&pg=PP1&dq=Many-Body+Quantum+Theory+in+Condensed+Matter+Physics&ots=KfemyYyCZt&sig=bdxOHiJ4ULrNctsB0hDM-gsuL9c&redir_esc=y#v=onepage&q&f=false>.

63 VOJTA, M.; BULLA, R. A fractional-spin phase in the power-law kondo model. **The European Physical Journal B-Condensed Matter and Complex Systems**, Springer, v. 28, p. 283–287, 2002. Disponível em: <https://doi.org/10.1140/epjb/e2002-00231-9>.

64 WITHOFF, D.; FRADKIN, E. Phase transitions in gapless fermi systems with magnetic impurities. **Physical review letters**, APS, v. 64, n. 15, p. 1835, 1990. Disponível em: <https://doi.org/10.1103/PhysRevLett.64.1835>.

65 BORKOWSKI, L. S.; HIRSCHFELD, P. Kondo effect in gapless superconductors. **Physical Review B**, APS, v. 46, n. 14, p. 9274, 1992. Disponível em: <https://doi.org/10.1103/PhysRevB.46.9274>.

66 CHEN, K.; JAYAPRAKASH, C. The kondo effect in pseudo-gap fermi systems: a renormalization group study. **Journal of Physics: Condensed Matter**, IOP Publishing, v. 7, n. 37, p. L491, 1995. Disponível em: <https://iopscience.iop.org/article/10.1088/0953-8984/7/37/003>.

67 INGERSENT, K. Behavior of magnetic impurities in gapless fermi systems. **Physical Review B**, APS, v. 54, n. 17, p. 11936, 1996. Disponível em: <https://doi.org/10.1103/PhysRevB.54.11936>.

68 GONZALEZ-BUXTON, C.; INGERSENT, K. Renormalization-group study of anderson and kondo impurities in gapless fermi systems. **Physical Review B**, APS, v. 57, n. 22, p. 14254, 1998. Disponível em: <https://doi.org/10.1103/PhysRevB.57.14254>.

69 BULLA, R. et al. The soft-gap anderson model: comparison of renormalization group and local moment approaches. **Journal of Physics: Condensed Matter**, IOP Publishing, v. 12, n. 23, p. 4899, 2000. Disponível em: <https://iopscience.iop.org/article/10.1088/0953-8984/12/23/302>.

70 INGERSENT, K.; SI, Q. Critical local-moment fluctuations, anomalous exponents, and ω/t scaling in the kondo problem with a pseudogap. **Physical Review Letters**, APS, v. 89, n. 7, p. 076403, 2002. Disponível em: <https://doi.org/10.1103/PhysRevLett.89.076403>.

71 SILVA, L. G. Dias da et al. Tunable pseudogap kondo effect and quantum phase transitions<? format?> in aharonov-bohm interferometers. **Physical review letters**, APS, v. 102, n. 16, p. 166806, 2009. Disponível em: <https://doi.org/10.1103/PhysRevLett.102.166806>.

72 ŽITKO, R.; BONČA, J.; PRUSCHKE, T. Van hove singularities in the paramagnetic phase of the hubbard model: Dmft study. **Physical Review B—Condensed Matter and Materials Physics**, APS, v. 80, n. 24, p. 245112, 2009. Disponível em: <https://doi.org/10.1103/PhysRevB.80.245112>.

73 MITCHELL, A. K.; FRITZ, L. Kondo effect with diverging hybridization: Possible realization in graphene with vacancies. **Physical Review B—Condensed Matter and Materials Physics**, APS, v. 88, n. 7, p. 075104, 2013. Disponível em: <https://doi.org/10.1103/PhysRevB.88.075104>.

74 MITCHELL, A. K. et al. Quantum phase transitions and thermodynamics of the power-law kondo model. **Physical Review B—Condensed Matter and Materials Physics**, APS, v. 88, n. 19, p. 195119, 2013. Disponível em: <https://doi.org/10.1103/PhysRevB.88.195119>.

75 ZHURAVLEV, A. Negative impurity magnetic susceptibility and heat capacity in a kondo model with narrow peaks in the local density of electron states. **The Physics of Metals and Metallography**, Springer, v. 108, n. 2, p. 107–115, 2009. Disponível em: <https://doi.org/10.1134/S0031918X09080018>.

76 ZHURAVLEV, A.; IRKHIN, V. Y. Kondo effect in the presence of van hove singularities: A numerical renormalization group study. **Physical Review B—Condensed Matter and Materials Physics**, APS, v. 84, n. 24, p. 245111, 2011. Disponível em: <https://doi.org/10.1103/PhysRevB.84.245111>.

77 ŽITKO, R.; BONČA, J. Kondo effect in the presence of rashba spin-orbit interaction. **Physical Review B—Condensed Matter and Materials Physics**, APS, v. 84, n. 19, p. 193411, 2011. Disponível em: <https://doi.org/10.1103/PhysRevB.84.193411>.

78 SHCHADILOVA, Y. E.; VOJTA, M.; HAQUE, M. Single-impurity kondo physics at extreme particle-hole asymmetry. **Physical Review B**, APS, v. 89, n. 10, p. 104102, 2014. Disponível em: <https://doi.org/10.1103/PhysRevB.89.104102>.

79 ŽITKO, R.; HORVAT, A. Kondo effect at low electron density and high particle-hole asymmetry in 1d, 2d, and 3d. **Physical Review B**, APS, v. 94, n. 12, p. 125138, 2016. Disponível em: <https://doi.org/10.1103/PhysRevB.94.125138>.

80 WONG, A. et al. Influence of rashba spin-orbit coupling on the kondo effect. **Physical Review B**, APS, v. 93, n. 7, p. 075148, 2016. Disponível em: <https://doi.org/10.1103/PhysRevB.93.075148>.

81 CHARLIER, J.-C.; BLASE, X.; ROCHE, S. Electronic and transport properties of nanotubes. **Reviews of modern physics**, APS, v. 79, n. 2, p. 677–732, 2007. Disponível em: <https://doi.org/10.1103/RevModPhys.79.677>.

82 WAKABAYASHI, K. et al. Electronic states of graphene nanoribbons and analytical solutions. **Science and technology of advanced materials**, IOP Publishing, v. 11,

n. 5, p. 054504, 2010. Disponível em: <https://iopscience.iop.org/article/10.1088/1468-6996/11/5/054504/meta>.

83 ZITKO, R. **NRG Ljubljana**. Zenodo, 2021. Disponível em: <https://doi.org/10.5281/zenodo.4841076>.

84 COSTI, T.; ZLATIĆ, V. Thermoelectric transport through strongly correlated quantum dots. **Physical Review B—Condensed Matter and Materials Physics**, APS, v. 81, n. 23, p. 235127, 2010. Disponível em: <https://doi.org/10.1103/PhysRevB.81.235127>.

85 MASTROGIUSEPPE, D. et al. Kondo effect in graphene with rashba spin-orbit coupling. **Physical Review B**, APS, v. 90, n. 3, p. 035426, 2014. Disponível em: <https://doi.org/10.1103/PhysRevB.90.035426>.

86 LIN, H.-H. et al. Ferromagnetism in armchair graphene nanoribbons. **Physical Review B—Condensed Matter and Materials Physics**, APS, v. 79, n. 3, p. 035405, 2009. Disponível em: <https://doi.org/10.1103/PhysRevB.79.035405>.

87 ALMEIDA, P. et al. Ferromagnetism in armchair graphene nanoribbon heterostructures. **Physical Review B**, APS, v. 105, n. 5, p. 054416, 2022. Disponível em: <https://doi.org/10.1103/PhysRevB.105.054416>.

88 CAI, J. et al. Atomically precise bottom-up fabrication of graphene nanoribbons. **Nature**, Nature Publishing Group UK London, v. 466, n. 7305, p. 470–473, 2010. Disponível em: <https://doi.org/10.1038/nature09211>.

89 LI, Y. et al. Anomalous kondo resonance mediated by semiconducting graphene nanoribbons in a molecular heterostructure. **Nature Communications**, Nature Publishing Group UK London, v. 8, n. 1, p. 946, 2017. Disponível em: <https://doi.org/10.1038/s41467-017-00881-1>.

90 ZALOM, P.; ŽONDA, M. Subgap states spectroscopy in a quantum dot coupled to gapped hosts: Unified picture for superconductor and semiconductor bands. **Physical Review B**, APS, v. 105, n. 20, p. 205412, 2022. Disponível em: <https://doi.org/10.1103/PhysRevB.105.205412>.

91 KITAO, T. et al. Scalable and precise synthesis of armchair-edge graphene nanoribbon in metal–organic framework. **Journal of the American Chemical Society**, ACS Publications, v. 142, n. 12, p. 5509–5514, 2020. Disponível em: <https://pubs.acs.org/doi/10.1021/jacs.0c00467>.

92 ASHCROFT, N. W.; MERMIN, N. D. **Solid State Physics**. [S.l.]: Holt-Saunders, 1976.

93 JONES, B. A.; VARMA, C. M.; WILKINS, J. W. Low-temperature properties of the two-impurity kondo hamiltonian. **Phys. Rev. Lett.**, v. 61, p. 125, 1988. Disponível em: <https://doi.org/10.1103/PhysRevLett.61.125>.

94 JONES, B. A.; VARMA, C. M. Critical point in the solution of the two magnetic impurity problem. **Phys. Rev. B**, v. 40, p. 324, 1989. Disponível em: <https://doi.org/10.1103/PhysRevB.40.324>.

95 SAKAI, O.; SHIMIZU, Y.; KASUYA, T. Excitation-spectra of 2 impurity anderson model. **Solid State Commun.**, v. 75, p. 81, 1990. Disponível em: <https://doi.org/10.1016/0038-1098(90)90346-D>.

96 STEWART, G. R. Heavy-fermion systems. **Rev. Mod. Phys.**, v. 56, p. 755, 1984. Disponível em: <https://doi.org/10.1103/RevModPhys.56.755>.

97 TSUNETSUGU, H.; SIGRIST, M.; UEDA, K. The ground-state phase diagram of the one-dimensional kondo lattice model. **Rev. Mod. Phys.**, v. 69, p. 809, 1997. Disponível em: <https://doi.org/10.1103/RevModPhys.69.809>.

98 GOLDHABER-GORDON, D. et al. Kondo effect in a single-electron transistor. **Nature**, v. 391, p. 156, 1998. Disponível em: <https://doi.org/10.1038/34373>.

99 KOUWENHOVEN, L.; GLAZMAN, L. Revival of the Kondo effect. **Phys. World**, v. 14, p. 33, 2001. Disponível em: <https://iopscience.iop.org/article/10.1088/2058-7058/14/1/28>.

100 PUSTILNIK, M.; GLAZMAN, L. Kondo effect in quantum dots. **J. Phys. Condens. Matter**, v. 16, p. R513, 2004. Disponível em: <10.1126/science.281.5376.526>.

101 OOSTERKAMP, T. et al. Microwave spectroscopy of a quantum-dot molecule. **Nature**, v. 395, p. 873, 1998. Disponível em: <https://doi.org/10.1038/27617>.

102 CRAIG, N. et al. Tunable nonlocal spin control in a coupled-quantum dot system. **Science**, v. 304, p. 565, 2004. Disponível em: <https://www.science.org/doi/10.1126/science.1095452>.

103 MARTINS, G. B. et al. Transport properties of strongly correlated electrons in quantum dots studied with a simple circuit model. **Phys. Rev. Lett.**, v. 96, p. 066802, 2006. Disponível em: <https://doi.org/10.1103/PhysRevLett.96.066802>.

104 BULLA, R.; VOJTA, M. Quantum phase transitions in models of magnetic impurities. In: HEWSON, A. C.; ZLATIĆ, V. (Ed.). **Concepts in Electron Correlation**. Springer Dordrecht, 2003. cap. 9, p. 209. Disponível em: <https://doi.org/10.48550/arXiv.cond-mat/0210015>.

105 VOJTA, M. Impurity quantum phase transitions. **Philos. Mag.**, v. 86, n. 13-14, p. 1807, 2006. Disponível em: <https://doi.org/10.1080/14786430500070396>.

106 SASAKI, S. et al. Fano-Kondo interplay in a side-coupled double quantum dot. **Phys. Rev. Lett.**, v. 103, p. 266806, 2009. Disponível em: <https://doi.org/10.1103/PhysRevLett.103.266806>.

107 ZITKO, R. Fano-Kondo effect in side-coupled double quantum dots at finite temperatures and the importance of two-stage Kondo screening. **Phys. Rev. B**, v. 81, p. 115316, 2010. Disponível em: <https://doi.org/10.1103/PhysRevB.81.115316>.

108 ZARÁND, G. Orbital fluctuations and strong correlations in quantum dots. **Philos. Mag.**, v. 86, p. 2043, 2006. Disponível em: <https://doi.org/10.1080/14786430500469069>.

109 EVERS, F. et al. Advances and challenges in single-molecule electron transport. **Rev. Mod. Phys.**, v. 92, p. 035001, 2020. Disponível em: <https://doi.org/10.1103/RevModPhys.92.035001>.

110 GUO, X. et al. Evolution and universality of two-stage kondo effect in single manganese phthalocyanine molecule transistors. **Nat. Commun.**, v. 12, p. 1566, 2021. Disponível em: <https://doi.org/10.1038/s41467-021-21492-x>.

111 POUSE, W. et al. Quantum simulation of an exotic quantum critical point in a two-site charge kondo circuit. **Nat. Phys.**, v. 19, p. 492, 2023. Disponível em: <https://doi.org/10.1038/s41567-022-01905-4>.

112 WILSON, K. G. The renormalization group: Critical phenomena and the kondo problem. **Rev. Mod. Phys.**, v. 47, p. 773, 1975. Disponível em: <https://doi.org/10.1103/RevModPhys.47.773>.

113 KRISHNA-MURTHY, H. R.; WILKINS, J. W.; WILSON, K. G. Renormalization-group approach to the anderson model of dilute magnetic alloys. i. static properties for the symmetric case. **Phys. Rev. B**, v. 21, p. 1003, 1980. Disponível em: <https://doi.org/10.1103/PhysRevB.21.1003>.

114 BULLA, R.; COSTI, T. A.; PRUSCHKE, T. Numerical renormalization group method for quantum impurity systems. **Rev. Mod. Phys.**, v. 80, p. 395, 2008. Disponível em: <https://doi.org/10.1103/RevModPhys.80.395>.

115 HOFSTETTER, W.; SCHOELLER, H. Quantum phase transition in a multilevel dot. **Phys. Rev. Lett.**, v. 88, p. 016803, 2001. Disponível em: <https://doi.org/10.1103/PhysRevLett.88.016803>.

116 VOJTA, M.; BULLA, R.; HOFSTETTER, W. Quantum phase transitions in models of coupled magnetic impurities. **Phys. Rev. B**, v. 65, p. 140405(R), 2002. Disponível em: <https://doi.org/10.1103/PhysRevB.65.140405>.

117 CORNAGLIA, P. S.; GREMPEL, D. R. Strongly correlated regimes in a double quantum dot device. **Phys. Rev. B**, v. 71, p. 075305, 2005. Disponível em: <https://doi.org/10.1103/PhysRevB.71.075305>.

118 ZITKO, R.; BONcA, J. Enhanced conductance through side-coupled double quantum dots. **Phys. Rev. B**, v. 73, p. 035332, 2006. Disponível em: <https://doi.org/10.1103/PhysRevB.73.035332>.

119 _____. Correlation effects in side-coupled quantum dots. **J. Phys. Condens. Matter**, v. 19, p. 255205, 2007. Disponível em: <10.1088/0953-8984/19/25/255205>.

120 CHUNG, C.-H.; ZARAND, G.; WÖLFLE, P. Two-stage Kondo effect in side-coupled quantum dots: Renormalized perturbative scaling theory and numerical renormalization group analysis. **Phys. Rev. B**, v. 77, p. 035120, 2008. Disponível em: <https://doi.org/10.1103/PhysRevB.77.035120>.

121 TAMURA, H.; SASAKI, S. Fano-Kondo effect in side-coupled double quantum dot. **Physica E**, v. 42, p. 864, 2010. Disponível em: <https://doi.org/10.1103/PhysRevB.81.115316>.

122 FERREIRA, I. L. et al. Capacitively coupled double quantum dot system in the kondo regime. **Phys. Rev. B**, v. 84, p. 205320, 2011. Disponível em: <https://doi.org/10.1103/PhysRevB.84.205320>.

123 TANAKA, Y.; KAWAKAMI, N.; OGURI, A. Crossover between two different Kondo couplings in side-coupled double quantum dots. **Phys. Rev. B**, v. 85, p. 155314, 2012. Disponível em: <https://doi.org/10.1103/PhysRevB.85.155314>.

124 BAINES, D. Y. et al. Transport through side-coupled double quantum dots: From weak to strong interdot coupling. **Phys. Rev. B**, v. 85, p. 195117, 2012. Disponível em: <https://doi.org/10.1103/PhysRevB.85.195117>.

125 LIAO, Y.-H.; HUANG, J.; WANG, W.-Z. Real two-stage Kondo effect in parallel double quantum dot. **J. Magn. Magn. Mater.**, v. 377, p. 354, 2015. Disponível em: <https://doi.org/10.1016/j.jmmm.2014.10.138>.

126 CRISAN, M.; GROSU, I.; TIFREA, I. An equation of motion analysis of the two stage Kondo effect in T-shaped double-quantum-dot systems. **Physica E**, v. 66, p. 245, 2015. Disponível em: <https://doi.org/10.1016/j.physe.2014.10.017>.

127 CHEN, X.-W. et al. Kondo physics in the T-shaped structure with two detuned quantum dots. **Physica E**, v. 134, p. 114928, 2021. Disponível em: <https://doi.org/10.1016/j.physe.2021.114928>.

128 HEWSON, A. C. **The Kondo Problem to Heavy Fermions**. [S.l.]: Cambridge University Press, 1993. (Cambridge Studies in Magnetism).

129 CAMPO, V. L.; OLIVEIRA, L. N. Alternative discretization in the numerical renormalization-group method. **Phys. Rev. B**, v. 72, p. 104432, 2005. Disponível em: <https://doi.org/10.1103/PhysRevB.72.104432>.

130 ALMEIDA, P. A. et al. Quantum impurity with 2/3 local moment in one-dimensional quantum wires: A numerical renormalization group study. **Phys. Rev. B**, v. 109, p. 045112, 2024. Disponível em: <https://doi.org/10.1103/PhysRevB.109.045112>.

131 HOFSTETTER, W. Generalized numerical renormalization group for dynamical quantities. **Phys. Rev. Lett.**, v. 85, p. 1508, 2000. Disponível em: <https://doi.org/10.1103/PhysRevLett.85.1508>.

132 LOGAN, D. E.; WRIGHT, C. J.; GALPIN, M. R. Correlated electron physics in two-level quantum dots: Phase transitions, transport, and experiment. **Phys. Rev. B**, v. 80, p. 125117, 2009. Disponível em: <https://doi.org/10.1103/PhysRevB.80.125117>.

133 Note that, as expected, $A_{eff}(\omega)$ obbeys the Friedel Sum Rule, i.e., $\pi\Gamma_{eff}A_{eff}(0) = 1$.

134 As in the case of the possible use of the Bethe-Ansatz for the calculation of the effective model universal-susceptibility (139), here, we could alternatively use a universal expression for $A_{eff}(\omega)$, provided, for example, in H. O. Frota, Phys. Rev. B 45, 1096 (1992).

135 ZITKO, R. ; cA, J. Bon. Multiple-impurity anderson model for quantum dots coupled in parallel. **Phys. Rev. B**, v. 74, p. 045312, 2006. Disponível em: <https://doi.org/10.1103/PhysRevB.74.045312>.

136 ZARÁND, G. et al. Quantum criticality in a double-quantum-dot system. **Phys. Rev. Lett.**, v. 97, p. 166802, 2006. Disponível em: <https://doi.org/10.1103/PhysRevLett.97.166802>.

137 ZITKO, R. ; MRAVLJE, J.; HAULE, K. Ground state of the parallel double quantum dot system. **Phys. Rev. Lett.**, v. 108, p. 066602, 2012. Disponível em: <https://doi.org/10.1103/PhysRevLett.108.066602>.

138 In Ref. (125), our Γ_0, Γ_1, and t_{01} notation becomes Γ_1, Γ_2, and t, respectively.

139 N. Andrei, K. Furuya, and J. H. Lowestein, Rev. Mod. Phys. 55, 331 (1983). More specifically, the universal susceptibility curve is listed in Table 3 in A. M. Tsvelick and P. B. Wiegmann, Adv. Phys. 32, 453 (1983).